geologicaacta

Citation: Marín, M., Carola, E., Beamud, E., Bover-Arnal, T., López-Blanco, M., Garcés, M., Roca, E., Costa, E., Ferrer, O., Cabrera, L., 2025. Paleogene kinematics of the central Catalan Coastal Ranges: temporal constraints from magneto-chronology and provenance analysis in synorogenic deposits in the SE margin of the Ebro Basin (NE Spain). Geologica Acta, 23.2, 1-25, I-XVI.

Online ISSN: 1696-5728 DOI: 10.1344/GeologicaActa2025.23.2

Paleogene kinematics of the central Catalan Coastal Ranges: temporal constraints from magneto-chronology and provenance analysis in synorogenic deposits in the SE margin of the Ebro Basin (NE Spain)

Miquel Marín[1,2] Eloi Carola[2,3] Elisabet Beamud[2,4] Telm Bover-Arnal[2,5] Miguel López-Blanco[2,3] Miguel Garcés[2,3] Eduard Roca[2,3] Elisenda Costa[3,6] Oriol Ferrer[2,3] Lluís Cabrera[2,3]

[1]SLB
Abingdon Technology Centre, OX14 4RU Abingdon, United Kingdom

[2]UB-Geomodels Research Institute
Facultat de Ciències de la Terra, University of Barcelona (UB), Martí i Franquès s/n, 08028 Barcelona, Spain

[3]Departament de Dinàmica de la Terra i de l'Oceà
Facultat de Ciències de la Terra, University of Barcelona (UB), Martí i Franquès s/n, 08028 Barcelona, Spain

[4] Paleomagnetic Laboratory CCiTUB - GEO3BCN CSIC
Carrer Lluís Solé i Sabarís s/n, 08028 Barcelona, Spain

[5]Departament de Mineralogia, Petrologia i Geologia Aplicada
Facultat de Ciències de la Terra, University of Barcelona (UB), Martí i Franquès s/n, 08028 Barcelona, Spain

[6]INS Torrent de les Bruixes (Departament d'Educació Generalitat Catalunya)
c/ Sta. Eulàlia s/n, 08921 Santa Coloma de Gramenet, Spain

ABSTRACT

The precise determination of the tectonic deformation timing such as thrust emplacement has always been a challenge for understanding the evolution of fold-and-thrust belts. In the Catalan Coastal Ranges, this issue has traditionally been addressed through the mapping and the analysis of the syn-tectonic successions preserved in the SE margin of the Ebro Basin. However, the age of the Paleogene contractional structures located towards the hinterland and responsible of the inversion and uplift of the inherited Mesozoic structure remained uncertain due to the lack of preserved syn-kinematic strata in these areas. With the aim of better understand the contractional evolution of the area during the Paleogene, this work presents a tectono-stratigraphic analysis approach that combines structural reconstructions, provenance analysis and magnetostratigraphic dating in well-exposed synorogenic sediments in the central SE margin of the Ebro Basin. The results of the study allow to establish the precise age of the main contractional structures present in the central Catalan Coastal Ranges. The combined analysis has revealed that: i) the inversion of the Montmell-Vallès Faults System started in the Bartonian and continued up to the late Priabonian, and ii) the emplacement of the Gaià-El Camp Thrust and the formation of the Cabra-Carme Anticline took place from early to late Priabonian and was the responsible of the sudden increased of the sedimentation rates. A later decrease of the sedimentation rates during late Priabonian (chron C15n) has been interpreted as the prelude of the end of the Paleogene compressional phase in the area.

KEYWORDS | **Catalan Coastal Ranges. Ebro Foreland Basin. Synorogenic. Magnetostratigraphy. Provenance Analysis. Paleogene.**

INTRODUCTION

Thrust systems in orogenic belts have traditionally been interpreted as usually propagating toward the foreland in a forward-breaking thrusting sequence (Boyer and Elliott, 1982; Butler, 1982, 1987). In this sequence, foreland basin sediments are progressively incorporated in the deformation wedge (Fig. 1). Thrusting can also develop towards the hinterland, a process known as break-back sequence (Boyer and Elliott, 1982; Butler, 1982, 1987). Moreover, out-of-sequence thrusts might develop in the hinterland of the fold-and-thrust belt, thus conditioning the advance of deformation as well as the configuration of the orogen (McClay, 1992). On the other hand, the configuration of fold-and-thrust belts can also be influenced by the presence of pre-existing extensional faults. The reactivation of these faults can lead to the development of inversion-related structures such as footwall shortcuts, hanging-wall folding and backthrusting as the effect of the buttressing (*e.g.* Amilibia *et al.*, 2008; Butler, 1989; Coward *et al.*, 1991; Coward, 1994; Ferrer *et al.*, 2023; Hayward and Graham, 1989; Scisciani *et al.*, 2001) or by changes in the mechanical stratigraphy (Couzens and Wiltschko, 1996; Ferril *et al.*, 2008; Gross *et al.*, 1997). Understanding the sequence of emplacement of thrusts is important in order to better interpret the changes in the sedimentation pattern over time due to the fact that tectonics and sedimentation are closely interconnected in orogenic belts. Thus, changes in depositional systems are often interpreted as responses to regional or local tectonic activity, such as the uplift and growth of nearby thrusts or folds. Moreover, the geometrical and genetic analysis of syn-tectonic strata can be used to understand the kinematics of individual structures (*e.g.* Burbank *et al.*, 1992; Fernández *et al.*, 2004; Ford *et al.*, 1997; Hardy *et al.*, 1996; Salvini and Storti, 2002; Suppe *et al.*, 1992; Vergés and Muñoz, 1990; Vergés *et al.*, 2002).

A thorough understanding of key geological elements and their critical moments is essential for accurately assessing natural resources like hydrocarbons, CO_2 storage, minerals, and geothermal energy. Determining the absolute and relative ages of structures is vital to assess uncertainties and exploration risks, like the timing between hydrocarbon generation and trap formation (Al-Hajeri *et al.*, 2009; Magoon, 1987; Makeen *et al.*, 2016) or cross-cutting relationships in non-accessible areas. Analyzing syn-kinematic sedimentation and growth geometries is crucial to determine the age and movement of structures in orogenic belts.

The Ebro Basin is the southern foreland of the Pyrenean orogen (northeastern Iberia) that developed from Late Cretaceous to middle Miocene times (Mouthereau *et al.*, 2014; Muñoz, 1992; Vergés and García-Senz, 2001). To the southwest and southeast, the Ebro Basin is limited by two intraplate chains that resulted from the inversion of pre-existent Mesozoic basins: the Iberian Range, and the Catalan Coastal Ranges (CCR) respectively (Fig. 2). The Ebro Basin infill is made up by both marine and continental sediments that thickens northwards and northwestwards up to over 5,000m (Rioja-3 borehole; Lanaja, 1987). At the basin margins, these sediments record the growth of the three mountain ranges. World-class examples of growth strata have been documented along the three margins (*e.g.*

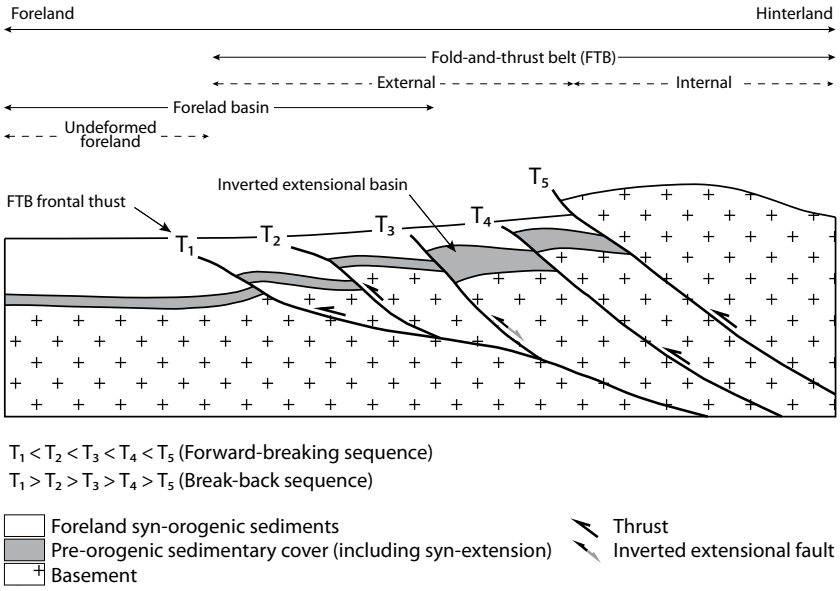

FIGURE 1. Schematic diagram of a thick-skinned fold-and-thrust belt, which includes an inverted extensional basin and its related foreland basin. Ti to Tv stand for relative timing of deformation. End-member thrusting sequences (forward-breaking and break-back) are also specified. Other combinations of relative timing imply out-of-sequence thrusting.

Anadón, 1978a, b; Anadón *et al.*, 1985, 1986; Colombo, 1994; Ford *et al.*, 1997; Gómez-Paccard *et al.*, 2011; Lawton *et al.*, 1999; López-Blanco, 2002; Riba, 1973, 1976; Suppe *et al.*, 1992, 1997; Vergés and Muñoz, 1990). Such growth strata geometries in the southeastern margin, together with clast composition and paleocurrents analysis performed in the alluvial and fan-delta sediments deposited at the toe of the CCR have been used to decipher the age and kinematics of some frontal fold-and-thrust structures both, regionally (Anadón, 1978a, b; Anadón *et al.*, 1985, 1989; Colombo, 1994; Gómez-Paccard *et al.*, 2011; López-Blanco, 2002; López-Blanco *et al.*, 2000a, b) and of the study area (Anadón, 1978a, b; Anadón *et al.*, 1986).

The study area is located along the central southeastern margin of the Ebro Basin, between Cabra del Camp and Vallespinosa towns (Fig. 2B). Previous studies have suggested the presence of a progressive unconformity at this location, indicating that the growth and uplift of the frontal structure of the central Catalan Coastal Ranges (Carme-Cabra Anticline) were contemporaneous with the deposition of conglomeratic units during the middle Eocene (Anadón *et al.*, 1985, 1986; Benzaquen *et al.*, 1973) (Fig. 2). Nevertheless, the age of the contractional structures located towards the hinterland and responsible for the inversion and contractional uplift of the pre-existent Mesozoic basins (Montmell Domain in Fig. 2B, C) remain uncertain due to the lack of preserved syn-kinematic strata in the footwall of the Montmell Fault.

To address this problem, the current study presents a detailed tectonostratigraphic analysis of the whole Paleogene

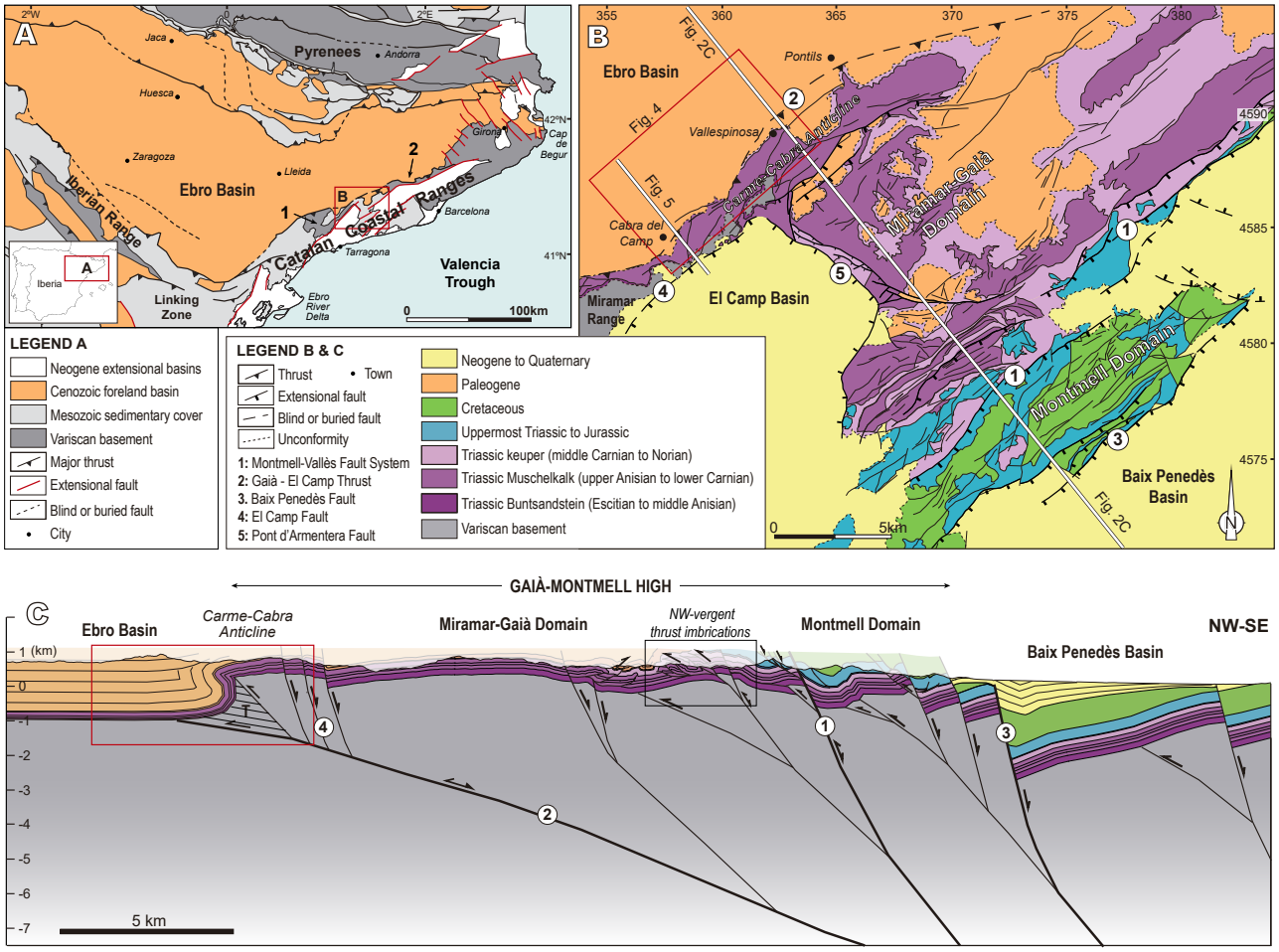

FIGURE 2. A) Geologic map of NE Iberia showing the major Cenozoic structural units including its three bounding orogenic belts: the Pyrenees and the intraplate Iberian and Catalan ranges. Cenozoic foreland basin-fill is highlighted in orange. Coordinates in geographical system. Labels 1 and 2 respectively correspond to the Prades Block and the Montserrat-Sant Llorenç del Munt areas referred in the text. B) Geological map of the Gaià-Montmell High in the central Catalan Coastal Ranges and adjoining areas. The area corresponds to the linkage zone between the Neogene Montmell-Vallès Fault System and El Camp Fault. Coordinates in UTM kms. C) Cross-section across the Gaià-Montmell High and its neighbouring areas. The hatched area labelled with "T" indicates the zone of distributed shear at the tip of the Gaià-El Camp Thrust (modified from Marín *et al.*, 2021). Legend for B and C is the same.

succession preserved in the central southeastern margin of the Ebro Basin along the northwestern limb of the Carme-Cabra Anticline which in the study are resembles more of a monocline (Fig. 2). It integrates results from a detailed geological map, clast composition and paleotransport direction analysis, and a magnetostratigraphic section performed across the 1,450m of the well-exposed Ebro Basin infill succession in the area. This approach enables the precise determination of the age and kinematics not only of the Carme-Cabra Anticline but also of the structures responsible for uplift and denudation of the inner parts of the central CCR during the Paleogene compressional phase.

GEOLOGICAL SETTING

Tectonostratigraphic framework

The CCR is a NE-SW-oriented structural unit that extends for up to 250km parallel to the NE coastline of Iberia (Fig. 2A). It is around 30km wide, and its basin-and-range configuration constitutes the onshore expression of the mainly extensional, divergent continental margin that separates the thicker crust of the Iberian Plate from the thinned crust of the Valencia Trough (Dañobeitia *et al.*, 1992; Roca and Guimerà, 1992; Vidal *et al.*, 1995). The current structure of the CCR is the result of three main tectonic phases: i) a multiepisodic extensional phase from late Paleozoic to Mesozoic, ii) a compressional phase during the Paleogene and iii) an extensional phase from latest Oligocene to middle Miocene (Anadón *et al.*, 1979; Bartrina *et al.* 1992; Baqués *et al.*, 2012; Cantarero *et al.*, 2014a, b; Llopis, 1947; López-Blanco *et al.*, 2000a, b; Marín *et al.*, 2021; Roca and Guimerà, 1992).

The Late Jurassic to Early Cretaceous extensional episode, well recorded in the neighbour Iberian Range (Guimerà, 2018; Salas and Casas, 1993), is represented by two right-stepped extensional basins, the Montmell-Garraf and Barcelona-Maresme basins bounded towards the northwest by two main extensional faults: the Montmell-Vallès Fault System and the Barcelona Fault (Fig. 3). These faults limit towards the NW the upper crust extensively deformed during the opening of the Tethys, in such a way that in their footwall blocks there are no Upper Jurassic or Lower Cretaceous sediments (Gaspar-Escribano *et al.*, 2004; Marín *et al.*, 2021; Roca and Guimerà, 1992; Salas, 2001).

Convergence and later collision between the Iberian and Eurasian plates took place from Late Cretaceous (Santonian) to middle-late Oligocene (Andeweg, 2002; Angrand and Mouthereau, 2021; Angrand *et al.*, 2020; Rosenbaum *et al.*, 2002; Srivastava *et al.*, 1990). In the NE of Iberia, this period led to the formation of the Pyrenees (García-Senz *et al.*, 2019; Muñoz, 1992; Muñoz, 2017; Vergés *et al.*, 2002), the Iberian Chain (Guimerà, 1984; Guimerà, 2018; Guimerà *et al.*, 1995; Nebot and Guimerà, 2016), and the Catalan Intraplate Chain (CIC) in the current location of the CCR (Anadón *et al.*, 1985; Guimerà and Álvaro, 1990; López-Blanco, 2002; Salas *et al.*, 2001) (Fig. 2A). In the study area, this entailed to the formation of the CIC from early Eocene to early Oligocene (Anadón *et al.*, 1985; Guimerà, 1984; Guimerà and Santanach, 1978; López-Blanco, 2002) by the tectonic inversion of the inherited Mesozoic extensional basins, and, towards the northwest, of the Ebro Foreland Basin (Anadón *et al.*, 1985; Baqués *et al.*, 2012; Juez-Larré and Andriessen, 2006; Marín *et al.*, 2021; Roca and Guimerà, 1992; Salas *et al.*, 2001). The CIC fold-and-thrust belt growth was controlled by the emplacement of major NW-directed NE-trending basement involving thrust sheets that incorporated the marginal parts of the developing Ebro Basin (Anadón *et al.*, 1986; Colombo, 1994; Gómez-Paccard *et al.*, 2011; López-Blanco, 2002; López-Blanco *et al.*, 2000a, b; Marín *et al.*, 2021).

The Paleogene contractive structure in the study area includes two domains with a differentiated stratigraphy in the Gaià-Montmell High (Marín *et al.*, 2021) (Fig. 2B, C). The Miramar-Gaià Domain in the NW comprises a very thin Mesozoic succession made up of only a Triassic succession uplifted over the Ebro Basin by a NW-directed low-angle basement thrust (the Gaià-El Camp Thrust). On the other hand, the Montmell Domain includes a well-developed Jurassic-Cretaceous succession (Fig. 3). The boundary between both domains corresponds to the Montmell-Vallès Fault System, a high-angle SE-dipping Mesozoic fault that was inverted during the Paleogene compressional phase as it is attested by the presence of NW-directed thrust imbrications developed along its footwall (Fig. 2C) (Baqués *et al.*, 2012; Marín *et al.*, 2021).

Throughout the Neogene, an extensional period associated to the rollback of the Tethyan Ocean plate during its subduction beneath the Iberian Plate took place (Carminati *et al.*, 1998; Roca, 1994; Roca *et al.*, 2004; Romagny *et al.*, 2020; Sabat *et al.*, 1995; van Hinsbergen *et al.*, 2014, 2020). This period resulted in the present-day horst-and-graben configuration of the CCR and the display of series of NNW-tilted blocks limited by major SE-dipping extensional faults (Fig. 2C). These faults resulted from the negative tectonic inversion (*i.e.* extensional reactivation) of the Paleogene faults (Baqués *et al.*, 2012; Bartrina *et al.*, 1992; Gaspar-Escribano *et al.*, 2004; Marín *et al.*, 2021; Roca, 2001). In this scenario, the study area comprises the footwall block of the northeastern end of one of these major Neogene extensional faults (El Camp Fault) and the northeastern edge of the extensional relay zone developed between this fault and the Montmell-Vallès Fault System (Fig. 2B).

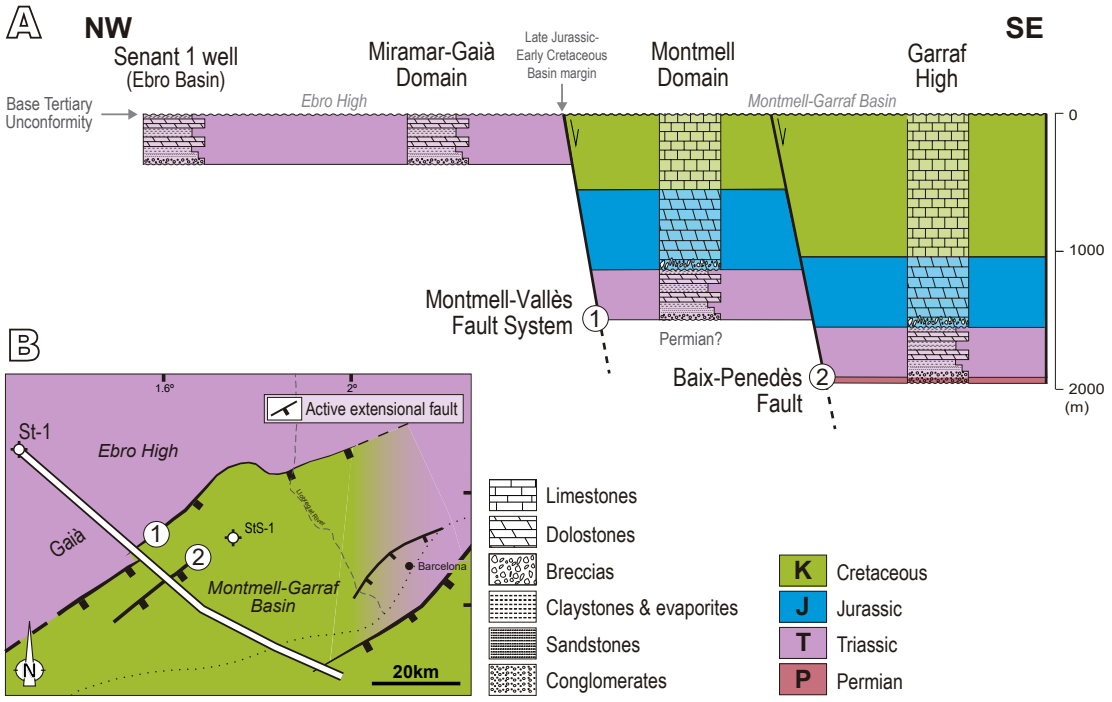

FIGURE 3. A) Mesozoic thicknesses across the central Catalan Coastal Ranges and the present-day offshore Barcelona-Maresme Basin. Upper reference datum corresponds to the base of the Tertiary. Mesozoic thicknesses based on Salas (1987), Lanaja (1987) and ICGC (2005). B) Tectonostratigraphic map of the central Catalan Coastal Ranges and offshore areas at the end of the Late Jurassic - Early Cretaceous extensional phase. Bcn E-1: Barcelona Marina E-1 well; StS-1: Sant Sadurní-1 well.

Alpine stratigraphic record of the central CCR and the SE Ebro Basin margin

The Alpine stratigraphy of the study area includes an upper Permian-Cretaceous cover unconformably overlain by the Paleogene sedimentary infill of the Ebro Basin. In the footwall of the Montmell-Vallès Fault System, this sedimentary cover is formed by an up to 200 to 350m succession of upper Permian-Triassic rocks (Galán-Abellán *et al.*, 2013; Mercedes-Martín *et al.*, 2014; Virgili *et al.*, 2006) (Miramar-Gaià Domain, Figs. 2; 3) encompassing siliciclastic, limestone, dolostone, and evaporitic rocks ascribed to Buntsandstein, Muschelkalk and Keuper facies (Arnal *et al.*, 2002; Calvet and Marzo, 1994; Escudero-Mozo *et al.*, 2017; Galán-Abellán *et al.*, 2013; Marin *et al.*, 2021, 2023; Mercedes-Martín and Buatois, 2020; Ortí *et al.*, 2017; Virgili, 1958). In contrast, Jurassic and Cretaceous rocks are present in the hangingwall of the Montmell-Vallès Fault System (Montmell Domain, Figs. 2; 3). This succession exceeds 2km in thickness (Salas, 1987) and includes Lower-Middle Jurassic dolomitic breccias, a relatively thick succession of Late Jurassic-Early Cretaceous (Barremian-Aptian) shallow marine limestones, dolomites, and shales (Albrich *et al.*, 2006; Salas, 1987; Salas *et al.*, 2001), and an upper Albian to Cenomanian sequence of fluvial and shallow marine carbonates that represents the youngest Mesozoic rocks preserved in the Montmell Domain (ICGC, 2005, 2018; Salas, 1987; Salas *et al.*, 2001). The Upper Jurassic to lower Albian succession is part of the extensional Montmell-Garraf Basin (Fig. 3) that developed during this period (Anadón *et al.*, 1979; Salas, 1987; Salas and Casas, 1993).

The Cenozoic stratigraphic record in the Ebro Basin infill consists of marine and continental sediments ranging from the Paleocene to the upper Eocene (Figs. 4; 5). As reported by the well Senant-1 (Lanaja, 1987) and from the geological maps (Figs. 2; 4) the Cenozoic succession, in some areas, rests directly on top of the Triassic succession. From the Paleocene to middle Eocene (middle Bartonian), the basin was connected to open Atlantic waters to the northwest (Garcés *et al.*, 2020 and references therein; Serra Kiel *et al.*, 2003). Yet, by the late Bartonian, the marine connections became restricted, leading to a change in sedimentation patterns over time (Costa *et al.*, 2010; Garcés *et al.*, 2020). This was recorded by the shift from marine marls to alternations of shales and anhydrite, halite, carnallite and sylvinite, recorded in the central parts of the basin and corresponding to the final stages of marine Priabonian sedimentation (Busquets *et al.*, 1985; Costa *et al.*, 2010; Pueyo, 1975; Reguant, 1967; Travé *et al.*, 1996). From the late Eocene (Priabonian) (Arasa-Tuliesa and Cabrera, 2018; Arche *et al.*, 2010) the Ebro Foreland Basin became an endorheic sedimentary trough filled exclusively with continental deposits including siliciclastic

sediments in the margins grading to lacustrine evaporites and carbonates towards the inner basin parts (Anadón *et al.*, 1989; Valero-Montesa *et al.*, 2014).

The Paleocene to Oligocene deposits present in the study area belong to the first marine basin-fill hemicycle and a part of the second endorheic hemicycle (Serra Kiel *et al.*, 2003).

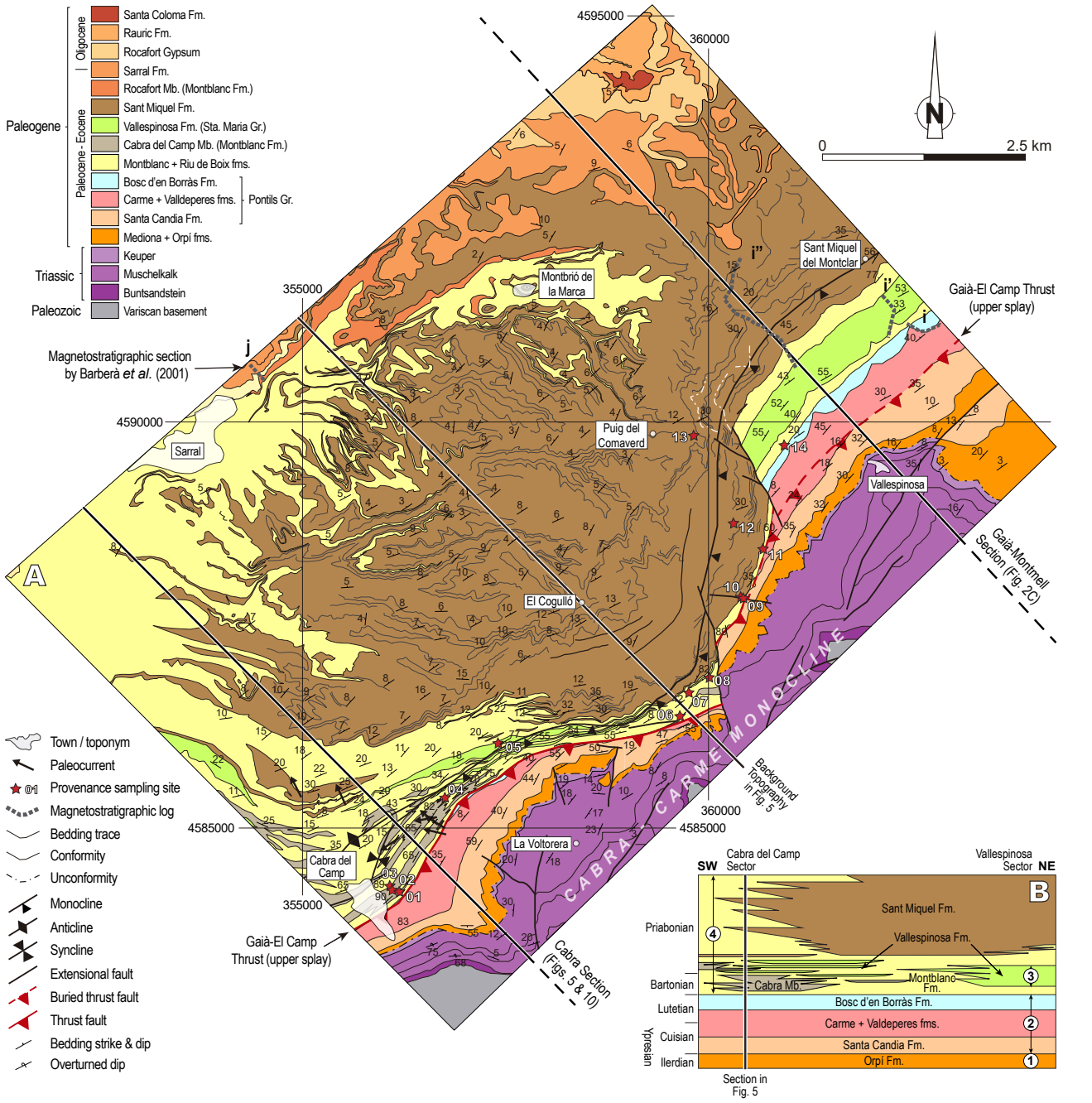

FIGURE 4. A) Geological map of the SE margin of the Ebro Basin between Cabra del Camp and Vallespinosa locations based on Carrera *et al.* (2020) and extended towards the northeast using the map from Colldeforns (unpublished). Labels i, i', i" stand for the Pontils magnetostratigraphic logs from Beamud *et al.* (2012). The basal portion of the magnetostratigraphic log corresponding to the Carme Fm. present in Figure 8, is located in the map shown in Figure I, Appendix II. Label j indicates the location of the Rocafort de Queralt magnetostratigraphic log from Barberà (1999) and Barberà *et al.* (2001). The location of the cross-section in Figure 5 is shown. The map uses UTM projection for zone 31N (ETR96 datum) and the coordinates are in meters. B) Not-to-scale schematic lithostratigraphic panel for the Eocene units. Numbers in the panel indicate the four major lithostratigraphic units defined in the area by Colldeforns *et al.* (1994a, b): 1) basal continental unit (Mediona Fm.) and a lower marine unit (Orpí Fm.); 2) Pontils-Cornudella Group; 3) Santa Maria Group; and 4) Barberà-Anoia Group.

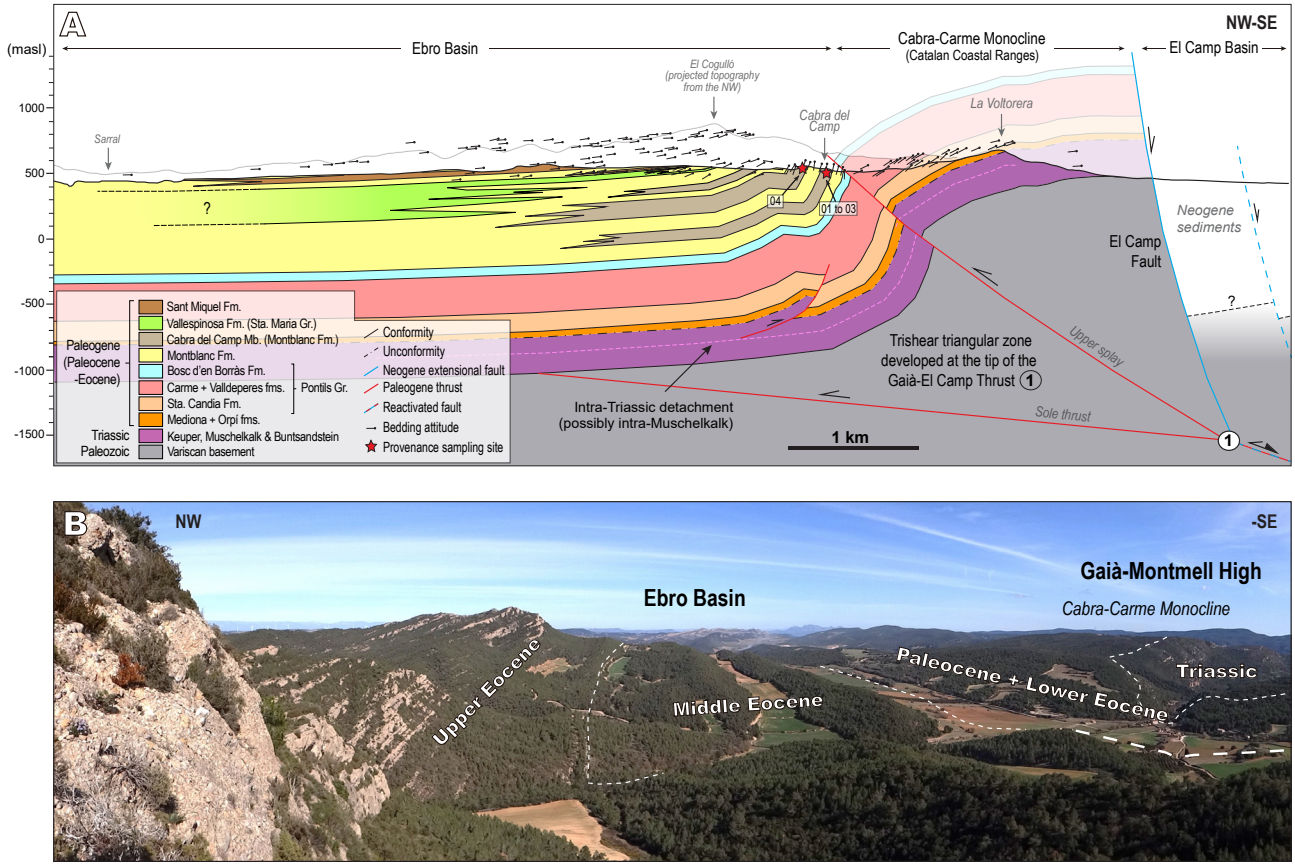

FIGURE 5. A) Geological cross-section of the SE margin of the Ebro Basin across the locality of Cabra del Camp. The section includes the NW frontal structure of the Catalan Coastal Ranges (Cabra-Carme Monocline). B) Field image of the limit between the Triassic and the succession of the foreland. See map in Figure 2 for location at regional scale and map in Figure 4 for a detail section location in the study area.

Colldeforns *et al.* (1994a, b) subdivided these Paleogene series into four lithostratigraphic assemblages: i) a basal assemblage formed by the Mediona and the Orpí formations; ii) the Pontils-Cornudella Group; iii) the Santa Maria Group from which only the Riu de Boix and the Vallespinosa formations are present in the studied area and iv) the Barberà-Anoia Group, the basal part of which is a lateral equivalent of the Santa Maria Group towards the northeast.

The basal assemblage is present in the Miramar-Gaià Domain and the northwestern limb of the Carme-Cabra Monocline. It begins with the Thanethian Mediona Fm. (Anadón, 1978a, b), a discontinuous continental unit formed by alluvial shales affected by intense pedogenic processes that unconformably overlies the Triassic cover. This basal unit is overlaid by the well dated marine Ypresian (Ilerdian) Orpí Fm. (Anadón, 1978a, b; Anadón *et al.*, 1979; Ferrer, 1971), a frequently dolomitized Alveolina limestone unit deposited in a shallow carbonate platform environment.

The Pontils-Cornudella Group (Anadón, 1978a, b; Anadón *et al.*, 1979, 1983, 1992; Colldeforns *et al.*, 1994b; Colombo, 1980, 1986) mainly encompasses non-marine detrital and lacustrine units Ypresian to Lutecian in age. The lower part of this unit is also present in the Miramar-Gaià Domain (Fig. 2). From bottom to top, in the study area, five formations have been distinguished in this group (Anadón, 1978a): a 80 to 110m thick succession of lacustrine limestones alternating with varicoloured mudstones of the Santa Càndia Fm.; a 170m thick mud flat plain facies (red mudstones with minor sandstone and calcareous intercalations) of the Carme Fm.; a variable thickness (up to a maximum of 100m) of evaporites and lacustrine carbonates of the Valldeperes Fm.; the lacustrine and palustrine limestones with interbedded marl and chert of the Bosc d'en Borràs Fm., which reaches its maximum thickness (about 100m) at the NE end of the study area and grades towards the southwest to distal alluvial mudstones.

Above, the Bartonian and Priabonian deposits of the Santa Maria and Barberà-Anoia groups are preserved in the northwest limb of the Carme-Cabra Monocline (Fig. 4). In the study area, the Santa Maria Group embraces up of nearly 300m thick succession of shallow marine and

transitional facies (*i.e.* deltaic, fan-deltaic conglomerates, sandstones, coral-bearing limestones, and marlstones with bioclastic sandstones intercalations) (Anadón and Marzo, 1986; Ferrer, 1971; Serra Kiel *et al.*, 2003) integrated in the Vallespinosa Fm. (Colldeforns *et al.*, 1994a).

On the other hand, the Barberà-Anoia Group (Colldeforns, 1994a; Colombo, 1980, 1986) comprises the Bartonian to Oligocene continental and lacustrine deposits. It includes up to six different formations: Montblanc, Sant Miquel, Sarral, Rocafort, Rauric and Santa Coloma (Colldeforns *et al.*, 1994a, b; Colombo, 1980, 1986). The Montblanc Fm. is made up of distal alluvial red beds that are interbedded with the marine sandstone of the Vallespinosa Fm. in its lower part, which becomes thicker and predominant towards the northeast. To the southwest, discontinuous alluvial conglomerate intercalations of the Cabra del Camp Mb. (Colldeforns, 1994a) are present showing a maximum thickness of around 200m in the Cabra del Camp area instead (Fig. 4). The Sant Miquel Fm. (Colombo, 1980, 1986) corresponds to a 600m thick succession of proximal alluvial fan conglomerates that unconformably overlay the marine sediments of the Santa Maria Group (Priabonian Riu de Boix Fm.) (Anadón *et al.*, 1986; Colldeforns *et al.*, 1994a). Towards the north and northeast, these conglomerates laterally change to late Priabonian to early Oligocene successions. These ones include the lacustrine carbonates and marls of the Sarral and Rocafort formations, the fluvial and lacustrine shales, marls, and lenticular conglomerates of the Rauric Fm. and the lacustrine marls and gypsums of the Santa Coloma Fm. (Benzaquen *et al.*, 1973; Colldeforns *et al.*, 1994a, b; Colombo, 1980, 1986).

The dating of these marine and non-marine lithostratigraphic units was formerly established and lately refined through the definition of biostratigraphic assemblages and biozones (Agustí *et al.*, 1987; Anadón, 1978a, b; Anadón and Feist, 1981; Anadón *et al.*, 1983, 1987, 1992; Feist *et al.*, 1994; Ferrer, 1971; Minwer-Barakat *et al.*, 2023; Sanjuan *et al.*, 2014; Serra-Kiel *et al.*, 2003; Tosal *et al.*, 2019). Further on, magnetostratigraphic studies done in neighbouring areas allowed the refinement of the biostratigraphic ages (Barberà, 1999; Barberà *et al.*, 2001; Beamud *et al.*, 2012; Costa *et al.*, 2010, 2013; Garcés *et al.*, 2020; Gomez-Paccard *et al.*, 2011).

METHODOLOGY

The present study uses an integrated approach that combines geological mapping, the construction of a geological section, provenance analysis and magnetostratigraphic dating. A NW-SE-oriented structural section was constructed combining up to 140 bedding dips in Triassic to Eocene rocks. This section uses a new geological map of the SE margin of the Ebro Basin between Cabra del Camp and Vallespinosa towns (Carrera *et al.*, 2020), which partially covers the area of study and was extended towards the northeast using a geological map done by Colldeforns (unpublished). All the data provided with the map (Fig. 4) are obtained from the field and the location was acquired with a device equipped with a GPS. The use of both maps allows constraining the contacts between stratigraphic units, stratigraphic thicknesses as well as structural relationships and attitudes (Fig. 5). Additionally, the use of 3D digital outcrop models was used to better refine the contact of some of the stratigraphic units (Appendix I).

The provenance analysis includes two main parts: the analysis of the palaeontological content in clasts from foreland conglomerates in order to define the tectonically uplifted areas exposed to erosion in the hinterland of the orogenic system, and the integration of paleocurrent indicators (*i.e.* base marks, channels) to determine the relative location of the alluvial deposits source. Up to 14 samples gathered through the Paleogene succession along the Ebro Basin margin between Cabra del Camp and Vallespinosa towns were analysed using thin sections (see map in Fig. 4 for their location).

The magnetostratigraphic analysis aims for an accurate reconstruction of the Paleogene compressional deformation in the central CCR by refining the age of the Paleogene succession to constrain the timing of the synorogenic sedimentation. The Pontils magnetostratigraphic section was carried out north and northwest of Vallespinosa where a relatively continuous northwest-dipping Paleogene succession occurs (Fig. 4). The sampled section consists of 238 measurement sites along ~1,430m of sedimentary record, which yields an average sampling resolution of 6 m/sample (Fig. I, Appendix II). The succession shows a relatively steep dip of 64º at the base of the section which progressively decreases to a gentle dip of 15º at the top. The first 410m of the Pontils section include the Carme, Valldeperes, Bosc d'en Borràs and Montblanc formations of the Pontils-Cornudella Group, followed by 300m of the Vallespinosa Fm. of the Santa Maria Group, extending up to the meter 716. The Montblanc-Riu de Boix formations along the Pontils section were not suitable for magnetostratigraphic purposes and no samples were obtained until the meter 800, where the first Sant Miquel conglomerates of the Barberà-Anoia Group crop out (Fig. 4). Details about the sampling and laboratory procedures of the magnetostratigraphic analysis are provided in the Appendix II.

RESULTS

Structure of the central SE margin of the Ebro Basin

The structure of the SE margin of the Ebro Basin across Cabra del Camp is illustrated in the section of the Figure 5A. Overall, the margin in the study area depicts an anticline-syncline geometry developed at the tip of a low-angle thrust that uplifts the basement and the sedimentary cover over a gently northwest-dipping regional level of the Ebro Basin (Fig. 5B). The most prominent structure in the section is the Cabra-Carme Monocline, which is cored by a trishear triangular zone (understood as the model proposed by Erslev, 1991) developed at the tip of the Gaià-El Camp Thrust. This monocline represents the northwest deformation front of the CCR and involves the Variscan Basement and the unconformably overlying sedimentary cover made up by a Germanic Triassic succession (Buntsandstein, Muschelkalk and Keuper) and the Paleogene strata of the Ebro Basin fill. A splay of the Gaià-El Camp Thrust propagates up to the surface showing a relatively low displacement. The trace of this thrust can be followed at surface for around 6km towards the northeast up to a zone characterized by the presence of NW-SE-oriented faults and the relatively thick conglomerates of the Sant Miquel Fm. (Fig. 4). From this point on, towards the northeast, the thrust appears progressively buried by the lower to middle Eocene Santa Càndia and Carme formations.

As shown by dip data and the cartographic traces, the geometry of the thrust footwall displays a pair of anticline-syncline structures that extend westward, parallel to the deformation front (Figs. 4; 5). Towards the northeast, the folds plunge and merge into a monocline structure (Fig. 4). The southern limb of the footwall syncline is characterized by the presence of nearly vertical beds of the Cabra del Camp Mb., which rapidly reduce their dip towards the northwest. This trend continues further northwest where dips between 5º and 8º are present around the location of Sarral town (Fig. 4). At depth, the aforementioned anticline-syncline pair has been interpreted as the result of the propagation of a southeast-directed out-of-syncline thrust, probably detached within the ductile levels of the middle Muschelkalk in the Triassic succession (Fig. 5). This structure transfers slip along the anticline forelimb to accommodate the tectonic shortening (Mitra, 2002).

In terms of lithostratigraphy, the conglomerates of the Cabra del Camp Mb. laterally and vertically grade towards the northwest into the finer-grained sediments of the Montblanc Fm. and, towards the northwest, into the marine succession of the Vallespinosa Fm. (Figs. 4B; 5). These three formations are overlaid by the massive conglomerates of the Sant Miquel Fm.

Additionally, the Cabra-Carme Monocline is affected near its hinge by the El Camp Fault, a high-angle, SE-dipping Neogene extensional fault that is interpreted as rooted in the Gaià-El Camp Thrust. This Neogene structure bounds towards the northwest the El Camp Basin and controls the development of a semi-graben depocenter on its hangingwall (Figs. 2; 5).

Paleocurrents and Provenance analysis

Paleocurrent indicators such as base marks, imbrications, channel base axis (Fig. 6A, B) were collected in the field in conglomeratic beds around Cabra del Camp (Figs. 4; 6C). Dips at these locations range from the nearly verticalized beds in the Cabra del Camp town area in the southern limb of the syncline at this location to the 25º of the Sant Miquel Fm. north of Cabra del Camp (Figs. 4; 5). Once restored to the horizontal, paleocurrent lineaments reveal a main flow direction towards the west and northwest (Fig. 6D), therefore implying a source area located east to southeast of the study area.

On the other hand, the analysis of the fossil content of carbonate clasts, which were sampled from coarse grained beds at 14 different sites distributed through the Paleogene succession along the margin (see locations in Fig. 4), has been performed aiming to provide information about their provenance and, therefore, the determination of the tectonically active areas. Samples 01 to 08 and 12 to 14 were collected at different levels of the Montblanc and Vallespinosa formations and Cabra del Camp Mb. Samples 09 to 11 were collected in undetermined alluvial deposits. To help in the tectonostratigraphic analysis, which is the objective of this study, only the sites close to the Cabra section (sites 01 to 04 sampled in the Cabra del Camp Mb.) are detailed while descriptions for each investigated sample can be found in the Table I, Appendix I.

Site 1 clasts are mainly grainstones dominated by *Alveolina*, *Opertorbitolites*, miliolids, other foraminifera and recrystallized green algae (Fig. 7A), as well as packstones containing peloids, orbitolinids, and fragments of rudist bivalves, other molluscs, and echinoids. Clasts exhibiting wackestone to packstone textures with ostracods occur (Fig. 7B) and sometimes the ostracod-bearing clasts include gastropods and can show bioturbation traces. Mudstones, dolostones, and wackestone to packstone textures with small miliolids and other foraminifera (Fig. 7C), bivalves and serpulids, are also common. Other clast facies identified include sandy limestone, a mudstone-wackestone with characean remains, a grainstone with recrystallized ooids and calcareous algae, a grainstone with ooids exhibiting radial and concentric coatings (Fig. 7D), and grainstone textures with ooids, peloids, intraclasts, orbitolinids, and fragments of oysters and other molluscs.

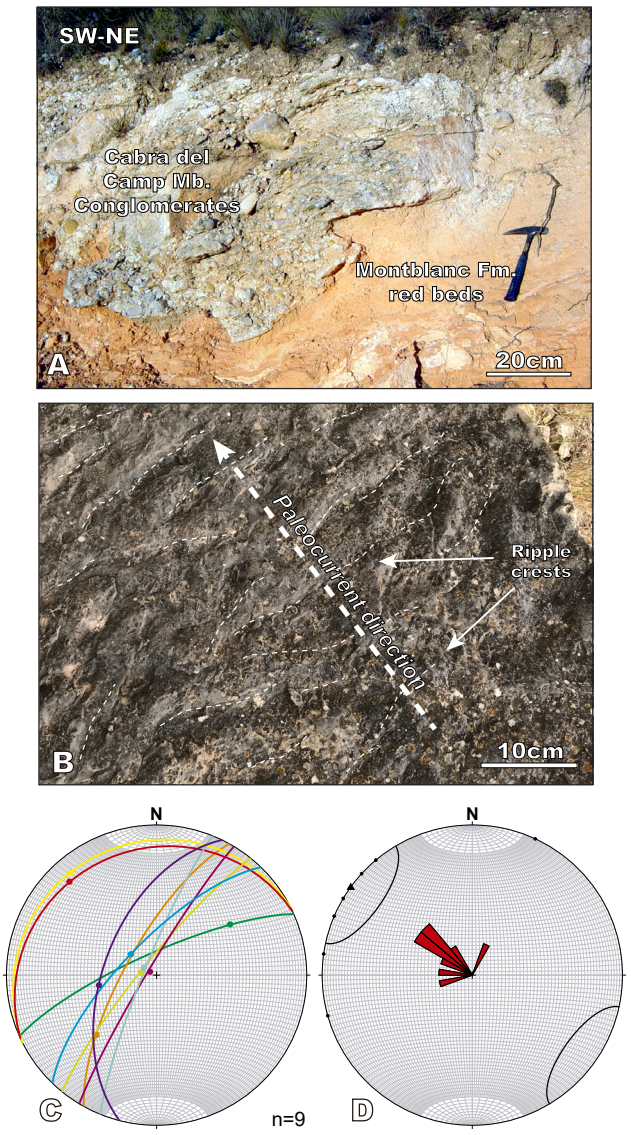

FIGURE 6. A) Paleochannel bottom outcrop in conglomerates of the Cabra del Camp Mb. used for paleocurrent measurements. B) Ripples at the bed top of marine-continental transitional facies. Dashed white arrow indicates the paleocurrent direction. C) Stereographic plot of paleocurrent measurements in the Cabra Fm. around the Cabra del Camp (n= number of measurements). See map in Figure 4 for location. D) Restored paleocurrent directions showing the predominant direction of the sediment supply.

Alveolina and fragments of orbitolinids were also recognized within the conglomerate matrix.

Site 2 clasts are made up of dolomitic limestone with a grainstone texture containing peloids (Fig. 7E), miliolids, other foraminifera, fragments of molluscs, echinoids, and calcareous algae, as well as a highly recrystallized limestone clast with abundant calcareous green algae (Fig. 7F). Fragments of oysters, gastropods, echinoids, and bryozoans occur. Non-skeletal components found in this latter highly recrystallized grainstone include peloids, silt-sized quartz grains and intraclasts. Non-skeletal components found in the highly recrystallized grainstone also include peloids, silt-sized quartz grains and intraclasts. Intraclasts are made up of packstone to grainstone textures with scarce ooids, other coated grains, peloids and silt-sized quartz. Furthermore, conglomerate clasts with packstone to grainstone textures including miliolids, Alveolina, Opertorbitolites, small rotaliids, other foraminifera, and fragments of echinoids and molluscs, were also recognized.

Site 3 sample contains clasts with orbitolinids (Fig. 7G), encrusting and agglutinating foraminifera, other foraminifera, fragments of oysters, other molluscs, calcareous algae and serpulids, as well as non-skeletal components such as peloids, intraclasts and silt-sized quartz. An additional investigated clast was made up of a recrystallized packstone texture with peloids, silt-sized quartz, miliolids, other foraminifers, and fragments of oysters, other molluscs, bryozoans, echinoids, and calcareous algae. Further analysed conglomerate clasts exhibit wackestone textures with small foraminifera, mudstone to wackestone textures, occasionally bioturbated, with ostracods and gastropods, packstone to grainstone textures with orbitolinids, peloids, and fragments of oysters, other molluscs, echinoids, corals, and calcareous algae, and grainstone textures with miliolids, Alveolina and other foraminifera. Finally, a clast made up of a "bacinellid" fabric was also identified (Fig. 7H).

Site 4 clasts exhibit grainstone textures with abundant orbitolinids. Miliolids, other foraminifera, and fragments of Marinella lugeoni, Permocalculus, other calcareous algae, bryozoans, echinoids, oysters, other bivalves, corals, and sections of belemnite rostra also occur (Fig. 7I). Non-skeletal components include well-rounded intraclasts, peloids and silt-sized quartz grains. A calclithite sample with silt to sand-sized quartz grains, peloids, ooids, miliolids, other undetermined benthic foraminifera and fragments of orbitolinids was also collected. The calclithite also includes small dolostone, mudstone and grainstone clasts. The latter is mainly made up of peloids and fragments of molluscs.

The Pontils magnetostratigraphic section

Thermal demagnetization of the studied samples reveals, in general, two stable paleomagnetic components after removal of a low temperature component that parallels either the present-day magnetic field or the drilling direction. This low temperature component is usually removed below 200-230ºC and will not be further considered. Above this, characteristic components pointing north with positive inclinations or south with negative inclinations are found along section. The temperature intervals selected to calculate each characteristic

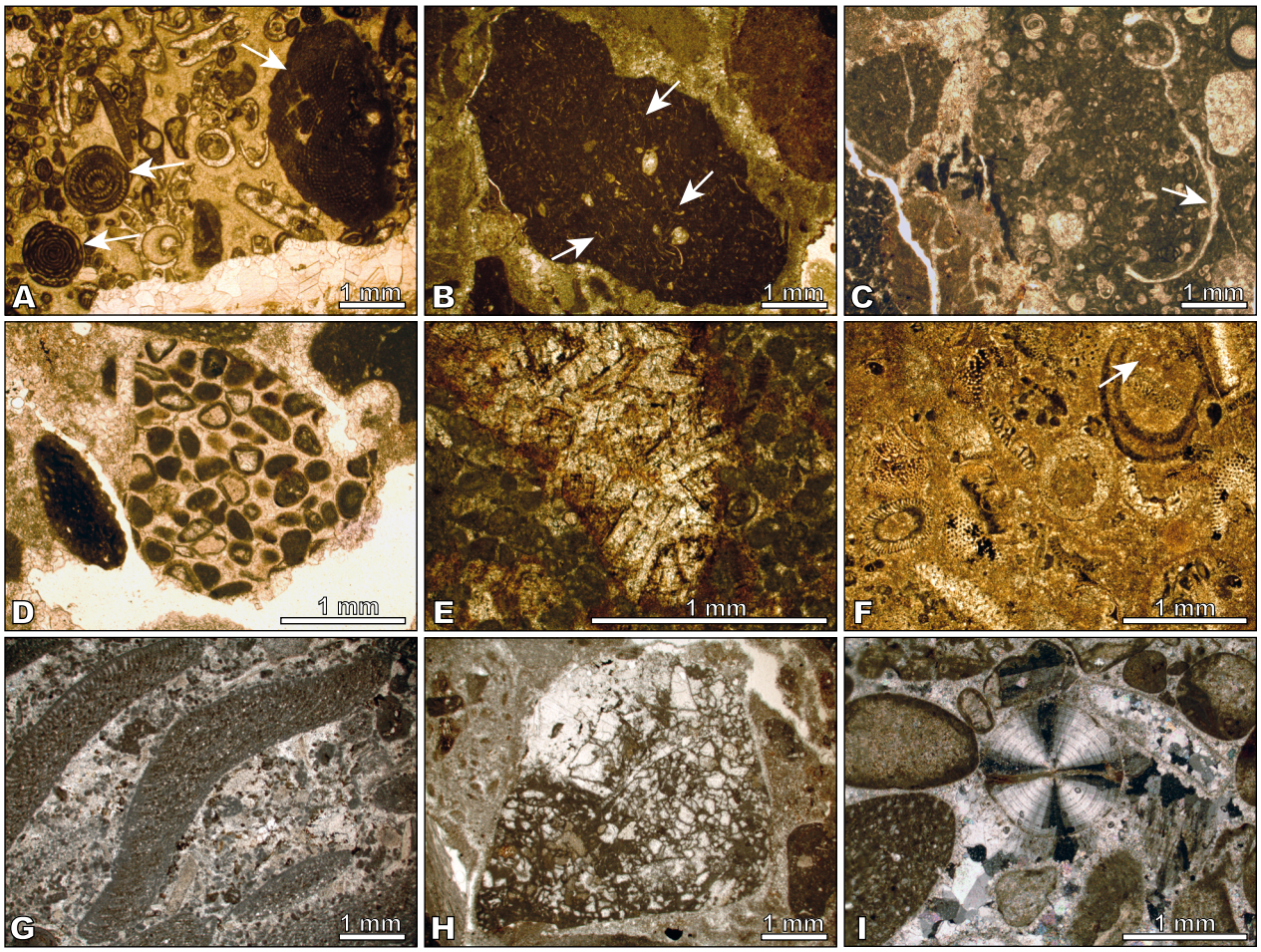

FIGURE 7. Clast microfacies. A) Photomicrograph of a grainstone texture from the Ypresian Orpí Fm. showing two Alveolina tests (left) and one of *Opertorbitolites* (upper right). Sampling site 1. B) Detail of a pebble-sized clast with ostracods giving rise to a wackestone texture. Santa Càndia Fm. (late Ypresian-Bartonian?). Sampling site 1. C) Close-up view of a packstone clast (centre to right) with small foraminifera and a section of a bivalve. Basal part of the Orpí Fm. (Ypresian). Sampling site 1. D) Sand-sized clast exhibiting a grainstone texture with ooids perhaps eroded from the Cenomanian Can Xuech Fm. Note the presence of an orbitolinid within the conglomerate matrix (right). Sampling site 1. E) Close-up view of a dolomitized miliolid and peloidal grainstone of Barremian-Aptian age. Sampling site 2. F) Photomicrograph of a recrystallized limestone exhibiting abundant sections of calcareous green algae. Cretaceous? Sampling site 2. G) Detail of an orbitolinid grainstone of Barremian-Aptian age. Sampling site 3. H) Pebble-sized clast of Aptian age showing a "bacinellid" fabric. Sampling site 3. I) Barremian-Aptian grainstone texture exhibiting a section of a belemnite rostrum (centre) under cross polarized light. Note the presence of an orbitolinid in the lower left part of the image. Sampling site 4.

component are compiled in the Table II, Appendix II. In general, characteristic components of grey mudstones and limestones are defined between 300-500ºC pointing to (titano)magnetite as the main remanence carrier. Characteristic components in red mudstones and fine-grained sandstones are defined at higher temperatures, up to 650-690ºC, pointing to hematites as the main remanence carrier. Despite this, some components are defined at temperatures around 400ºC thus suggesting a mixture of (titano)magnetite and hematite in the red beds. No substantial changes in magnetic susceptibility are observed upon progressive thermal demagnetization (Table III, Appendix II), indicating that not significant mineral neoformation occurred inside the thermal demagnetizer. The calculated characteristic components have been assigned to three qualities. Type 1 quality is assigned when the paleomagnetic direction can be calculated with more than 3 demagnetization steps and demagnetization diagrams yield linear trends to the origin of coordinates with maximum angular deviations (MAD) around 5º. Directions are defined as type 2, when MAD >5º, yet they can still be calculated by at least three demagnetization steps. Samples with erratic trends in which directions can be hardly calculated, often with only two demagnetization steps, yield type 3 directions, which are not considered for building the sequence of polarity zones in the magnetostratigraphic section. Nevertheless, this is not a significant issue since 205 directions out of 238 sites have been assigned to either type 1 or 2, which represents that 86% of the demagnetized samples yield

reliable paleomagnetic directions. Magnetic polarities are deduced after computing the Virtual Geomagnetic Pole latitude (VGP) from the characteristic component of each site. Positive values of VGP are interpreted as normal polarities and are represented in black when building the local magnetostratigraphic column (Fig. 8). Accordingly, negative VGP values are interpreted as reversed polarities and represented in white in the local magnetostratigraphic column. To define the magnetozones that constitute the local magnetostratigraphy at least two consecutive sites of the same polarity are needed. By doing so, 9 reversed and 9 normal magnetozones have been identified in the Pontils magnetostratigraphic section which can be correlated to the Geomagnetic Polarity Timescale (GPTS).

The magnetostratigraphic section is located a few km southwest of the Pontils village (Fig. 2B), where the fossil locality of Pontils was reported (Anadón, 1978a, b; Anadón and Feist, 1981; Minwer-Barakat *et al.*, 2023). The Pontils fossil site was assigned to the MP15 Mammal Paleogene Reference Level by Schmidt-Kittler (1987). Lithostratigraphic correlation of the fossil site to the Pontils magnetostratigraphic section places the first levels containing significant fossil mammal remains (sample PO22 from Minwer-Barakat *et al.*, 2023) around the meter 330 and the last levels containing significant mammal fossil remains (PO39 from Minwer-Barakat *et al.*, 2023) around the meter 400. Therefore, both levels are contained respectively between the base and the top of the Montblanc Fm. (Fig. 8). Additionally, the fossil site Rocafort de Queralt (RO), assigned to MP19-20 (Anadón *et al.*, 1987), can be lithostratigraphically correlated from the neighbouring Rocafort magnetostratigraphic section (Barberà *et al.*, 2001) to the meter 1,350 of the Pontils section, within the Sant Miquel conglomerates of the Barberà-Anoia Group (Fig. 8).

DISCUSSION

This discussion is divided into three parts: first, the attribution of age of the clasts sampled in the Cabra del Camp conglomerates; second, the age of the sampled Eocene units from the paleomagnetic study; and third, the tectono-stratigraphic interpretations and their implications in the tectonic evolution of the central CCR.

Source area age attribution of the upper Eocene clasts in the central SE margin of the Ebro Basin

The northwest-directed paleocurrents measured within the sampled upper Eocene strata (Figs. 4; 6) suggest the presence of higher reliefs toward the southeast of the study area, indicating a possible source of sediment input from elevated terrains. This pattern implies that the southeast region may have acted as a topographic high or a tectonically active area during the deposition of these strata, influencing sediment transport and depositional processes across the basin.

The detailed fossil content description carried out on clasts from the upper Eocene alluvial units (Cabra Mb., Montblanc Fm. and Sant Miquel Fm.) and the shallow marine units (Vallespinosa Fm.) provides key information about the formations that were exhumed and eroded in the source area at the time of sedimentation. A detailed summary with the attributed ages for each studied sample can be found in Table I, Appendix I.

A series of clast-types have been used to determine the original stratigraphic units where these clasts are derived from. These types are described below from younger to older and are summarized in Figure 9.

Type A clasts: Ypresian

The wackestone and packstone textures with undetermined small foraminifera (Fig. 7C) recognized in sites 01 and 03 are characteristic of the basal part of the Orpí Fm. (see figure 28 in Anadón, 1978a, b) and, therefore, are Ypresian (Ilerdian) in age.

Type B clasts: Ypresian

Grainstone clasts rich in *Alveolina*, *Opertorbitolites* (Fig. 7A), miliolids, gypsinids, and algae are prevalent throughout the studied clastic deposits and consistently present across nearly all sampling sites. These clasts, as well as the *Alveolina*, *Opertorbitolites* and gypsinid tests found in the conglomerate matrix in sites 07, 08, 09, 11 and 12, were also eroded from the Ypresian (Ilerdian) Orpí Fm. (see Anadón, 1978a, b).

Type C clasts: Cenomanian

The grainstone with well-formed ooids (Fig. 7D) exhibiting radial and concentric coatings sampled in site 01 is probably Cenomanian in age. Esteban (1973) reported similar facies from the Cenomanian Can Xuech Fm. in the Montmell area (Fig. 2).

Type D clasts: Barremian-Aptian, Upper Cretaceous, Ypresian

The age of the freshwater limestone facies with ostracods (Fig. 7B) and characeans recognized in clasts from sites 01 and 03 could have been sourced from the Barremian-Aptian and/or Upper Cretaceous as have been reported in the CCR (*e.g.* Esteban, 1973; Martín-Closas

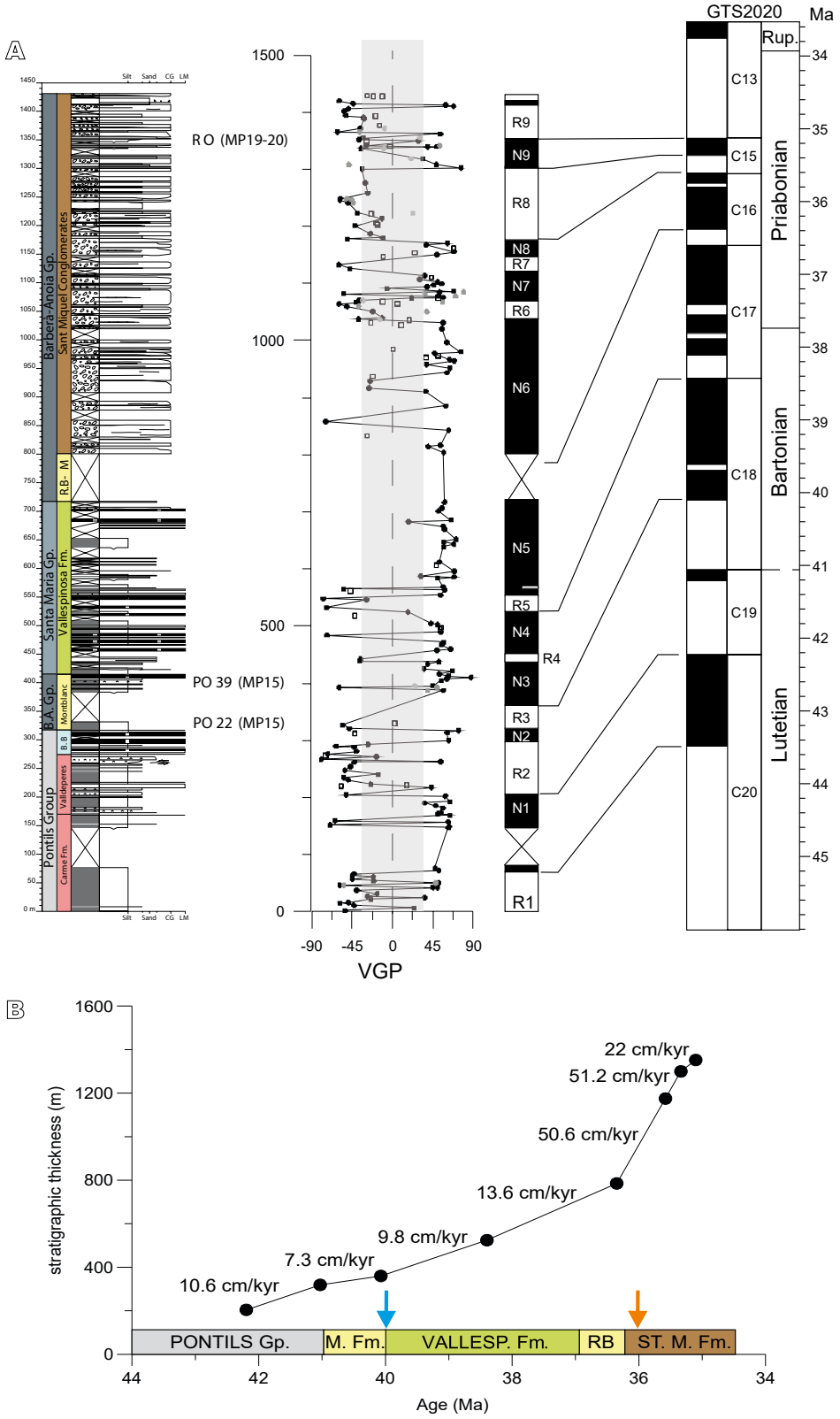

FIGURE 8. Magnetostratigraphy of the Pontils section. A) Magnetostratigraphic section and correlation to the GPTS (Gradstein *et al.*, 2020). PO and RO correspond to Pontils and Rocafort de Queralt fossil sites, respectively, with their attribution to Mammal Paleogene Reference Levels in brackets. White squares in the Virtual Geomagnetic Pole (VGP) graph represent type 3 directions, discarded to build the local magnetostratigraphy. B.A.Gp.: Barberà-Anoia Group; B.B.: Bosc d'en Borràs and R.B-M: Riu de Boix-Montblanc formations in the stratigraphic column. B) Sedimentation rates values and evolution for the Pontils section. Blue arrow: Bartonian transgressive event at the base of Santa Maria Group. Orange arrow: time of disconnection from the ocean of the Ebro Basin.

Sampled unit	Source area age attribution					
	Cretaceous				Paleogene	
	Lower Cretaceous		Upper Cretaceous		Eocene	
	Barremian-Aptian			Cenomanian	Ypresian	
Sant Miquel Fm.		E			B	
Vallespinosa Fm.		E			B	
Cabra del Camp Mb.	G	D E F H	D	C H	A D H	

FIGURE 9. Source area age attribution of the upper Eocene clasts in the central SE margin of the Ebro Basin. Clast type classification: A: Ypresian wackestones-packstones. B: Alveolina limestone. C: Cenomanian ooidal grainstones. D: Lacustrine limestones (Barremian-Aptian, Upper Cretaceous, Ypresian. E: Barremian-Aptian: orbitolinid limestone. F: Barremian-Aptian grainstones. G: Undifferentiated Cretaceous limestone. H: Undifferentiated Cretaceous or Early Eocene dolostones.

et al., 2018, this volume; Salas, 1987), but also from the Ypresian (Cuisian) Santa Càndia Fm., which belongs to the Pontils-Cornudella Group and overlies the Ypresian (Ilerdian) Orpí Fm. (Anadón, 1978a, b).

Type E clasts: Barremian-Aptian

Clasts and matrix samples containing orbitolinids also occur in almost all sampled sites (Figs. 7D, G; I). The presence of orbitolinids, and occasionally of *Nummuloculina*, *Marinella lugeoni*, *Permocalculus*, as well as fragments of rudist bivalves and belemnites (Fig. 7I), indicate a Barremian-Aptian age (Esteban, 1973; Robles, 1982; Salas, 1987).

Type F clasts: Barremian-Aptian

The grainstones dominated by the presence of peloids, scarce ooids, miliolids (Fig. 7E) and fragments of molluscs and echinoids found in sites 01 to 04 also show facies like those observed in Barremian-Aptian platform carbonates from the CCR (Esteban, 1973; Robles, 1982; Salas, 1987) and are therefore ascribed to this age interval. The "bacinellid" fabric-bearing clast (Fig. 7H) recognized in sampling site 03 is also representative of the Aptian Stage (see Schlagintweit and Bover-Arnal, 2013).

Type G clasts: undifferentiated Cretaceous

In sampling site 02, a clast made up of highly recrystallized limestone with abundant calcareous green algae was collected (Fig. 7F). The age of this sample is unknown. Similar deposits dominated by calcareous green algae, which are common in Cretaceous platform carbonates (*e.g.* Esteban, 1973; Salas, 1987), have not been reported in the Paleogene record of the CCR (Anadón, 1978a, b). Therefore, the age of this sample has been ascribed to the Cretaceous.

Type H clasts: undifferentiated Cretaceous or early Eocene

In the CCR, dolostone stratigraphic intervals that could have sourced the dolostone clasts found in the investigated conglomerate deposits of the Cabra del Camp Mb. (Sites 01 to 04) include the Barremian-Aptian succession (Robles, 1982; Salas, 1987), the Cenomanian Can Xuech Fm. (Esteban, 1973) and the Orpí Fm. of Ypresian age (Anadón, 1978a, b). The Jurassic and Triassic record also includes dolostone intervals (*e.g.* Salas, 1987). However, non-dolomitized clasts older than Lower Cretaceous have not been recognized in the sampling sites. Therefore, the dolostone clasts identified are more likely to be of Cretaceous or early Eocene in age.

Age of the Pontils magnetostratigraphic section

The proposed correlation of the Pontils local magnetostratigraphic section to the GPTS (Gradstein *et al.*, 2020) suggests that the deposition of the Pontils section occurred between C20r to C13r chrons (Lutetian to Priabonian) (Fig. 8A). This correlation is based on both the reversal pattern, the location of fossil sites PO and RO along the section and cartographic relationship with neighbouring sections (López-Blanco *et al.*, 2024). Fossil site RO (MP19-20) is located around the meter 1350 in the Pontils section coinciding with the upper part of the normal magnetozone N9 (Fig. 8A). Correlation of RO to C15n by Barberà *et al.* (2001) also favours the correlation of N9 to C15n in the Pontils section, which pins the upper part of the section. The base of the Sant Miquel conglomerates is also characterized by a long normal magnetozone N6, which we propose to correlate to C16n based on the geological mapping-deduced vertical and lateral relationships with the Tossa Fm. (López-Blanco *et al.*, 2024) that is correlated to C16n by Costa *et al.* (2013). Therefore, deposition of the Sant Miquel conglomerates occurred from C16n up to C13r (36.2Ma up to 34.5Ma according to GPTS version of Gradstein *et al.* (2020)). The Riu de Boix-Montblanc Fm. does not provide a characteristic reversal pattern since no data are available due to bad outcrop conditions. However, it has been assigned to C16r.2r-C17n.1n (Fig. 8A). Below, the Vallespinosa Fm. within the Santa Maria Gp. yields N5, N4 and part of N3 normal magnetozones and R4 and R5 reversed magnetozones. N5 is correlated to C17n.2n and 3n (Priabonian-Bartonian), whereas R5, N4, R4 and top of N3 are correlated to Bartonian chrons C17r.3r, C18n.1n, C18r.1r and top of 18n.2n, respectively. The Montblanc Fm., in a stratigraphic position equivalent to the Pontils fossil site (MP15, Fig. 8), also records the magnetozone N3 and the reversed magnetozone R3, which are correlated to C18n.2n and the base of C18r.2r respectively. Therefore, the Pontils fossil site correlation to the GPTS confirms the Bartonian age assigned by Minwer-Barakat *et al.* (2023)

and not the uppermost Lutetian age as previously suggested by Beamud *et al.* (2003) and Beamud (2013) due to an imprecise location of the fossil site on top of the Bosc d'en Borràs Fm. Limestones and the heterochronous character of its top due to the transition to SW to detrital Montblanc Fm. strata. From this correlation the fossil site spans from approximately 41Ma (PO22, reversed polarity) to 39.8Ma (PO39, normal polarity). Following down-section, the Bosc d'en Borràs, Valldeperes and Carme formations reversal pattern formed by magnetozones N2, R2, N1 and R1 are proposed to correlate to C19n, C19r, C20n and C20r respectively (Fig. 8A).

Although bio- and chronostratigraphic implications of the European Paleogene reference levels are beyond the scope of this study, it is worth pointing out that the Bartonian age of the Pontils fossil site derived from this work only refers to the Pontils fossil site and not to the calibration of the MP15 reference level. As an example, the Sant Jaume de Frontanyà (SJF) fossil site (Busquets *et al.*, 1992; Moyà-Solà and Kohler, 1993), which is also assigned to MP15 reference level, has been traditionally dated as early Bartonian (Bonilla-Salomón *et al.*, 2016). However, a new 6.5km thick composite magnetostratigraphic section within the Ripoll syncline, in the south Pyrenean foreland, correlates the SJF fossil site to C20n (late Lutetian) (Juvany *et al.*, 2024). This implies a time span of more than 3Myr between SJF and Pontils fossil sites, both belonging to the MP15 reference level. Therefore, further studies are needed in order to understand the chronostratigraphic significance of the Paleogene mammal reference levels.

Using the absolute ages obtained from the correlation of the magnetostratigraphic log with the GPTS 2020 and the stratigraphic thickness corresponding to the different magnetozones, values of sedimentation rates have also been calculated (Fig. 8B). The Pontils-Cornudella Group (C20n to C19n) correlates to low sedimentation rates with an average value of 10.6cm/kyr. The Montblanc, Vallespinosa and Riu de Boix formations (C18n to C16r) also represent low sedimentation rates, although slightly increasing the values between 7.3 at the base and 13.6cm/kyr towards the top (Fig. 8B). Conversely, the base of the Sant Miquel Fm. at C16n shows an abrupt change in the sedimentation rates to much higher values sustained for 1Myr (from 50.6cm/kyr at C16n to 51.2cm/kyr at C15r), finally decreasing to 22cm/kyr at C15n.

Tectonostratigraphic evolution of the central Catalan Coastal Ranges during the Paleogene compression: relative and absolute timing of thrust emplacement

The compressional phase related to the convergent motion between the Iberian and Eurasian plates started in the late Santonian (Late Cretaceous) (Roest and Srivastava, 1991; Rosenbaum *et al.*, 2002). However, the first evidence of the transmission of the compressional stresses into the CCR area occurs at the end of the Cretaceous (possibly Maastrichtian), as recorded in the Miramar-Gaià Domain by the presence of a paraconformity that brings in contact basal Paleogene and Triassic (Keuper) strata (Figs. 4; 5). This unconformity denotes a period of regional uplift linked to either, a Late Cretaceous contractional deformation, or an isostatic adjustment after the Late Jurassic to Early Cretaceous rifting phase (Marín *et al.*, 2021). A subsequent period of tectonic quiescence from Paleocene to middle Eocene (late Lutetian) is illustrated by the sedimentation of conformable fine-grained terrigenous and carbonate beds deposited in the distal areas of the South-Pyrenean foreland (Anadón, 1978 a, b; Anadón *et al.*, 1985). The presence of *Alveolina* and *Opertorbitolites*, as well as freshwater limestone facies in clasts from the first conglomeratic beds present in the basin margin suggests that, at least, Paleocene-Ypresian (Ilerdian to lower Cuisian) strata from the Mediona, Orpí and Santa Càndia formations and, probably, upper Cuisian to Lutetian from the Carme, Valldeperes and Bosc d'en Borràs formations, were unconformably overlying Cretaceous rocks of the Montmell-Garraf Basin area (Fig. 10A). This stratigraphic succession indicates the absence of significant deformation or creation of relief in the adjacent areas and its extension towards the southeast remains uncertain.

The first significant compressional period in the study area corresponds to the beginning of the tectonic inversion of the Montmell Fault, which drives the uplift of Montmell-Garraf Basin and the overlying strata over the undeformed Ebro Basin (Fig. 10B). This inversion is characterized by the development of footwall shortcuts in the upper part of the reactivated faults as well as the presence of minor buttressing (*e.g.* SE-directed backthrusts and pop-up structures) in the Montmell Fault hangingwall (Marín *et al.*, 2021). The uplift of the Montmell-Garraf Basin controlled the denudation of the positive reliefs and the deposition of the first syn-compression succession recorded in the studied sector of the Ebro Basin margin (Fig. 11). The base of this succession corresponds to the first conglomerates of the Cabra del Camp Mb. (Montblanc Fm.). The observed parallelism with the strata underneath denotes that their deposition was before the emplacement of the Gaià-El Camp Thrust (pre-Gaià-El Camp Thrust kinematic, Fig. 11) therefore contradicting previous interpretations that included these conglomerates as part of a growth sequence (*i.e.* Anadón *et al.*, 1986).

The analysis of the fossil content in clasts from the Cabra del Camp Mb. conglomerates and coeval units (Montblanc and Vallespinosa formations) reveals that the source area contained rocks from the Lower Cretaceous (Barremian-Aptian), Upper Cretaceous (Cenomanian, Turonian and,

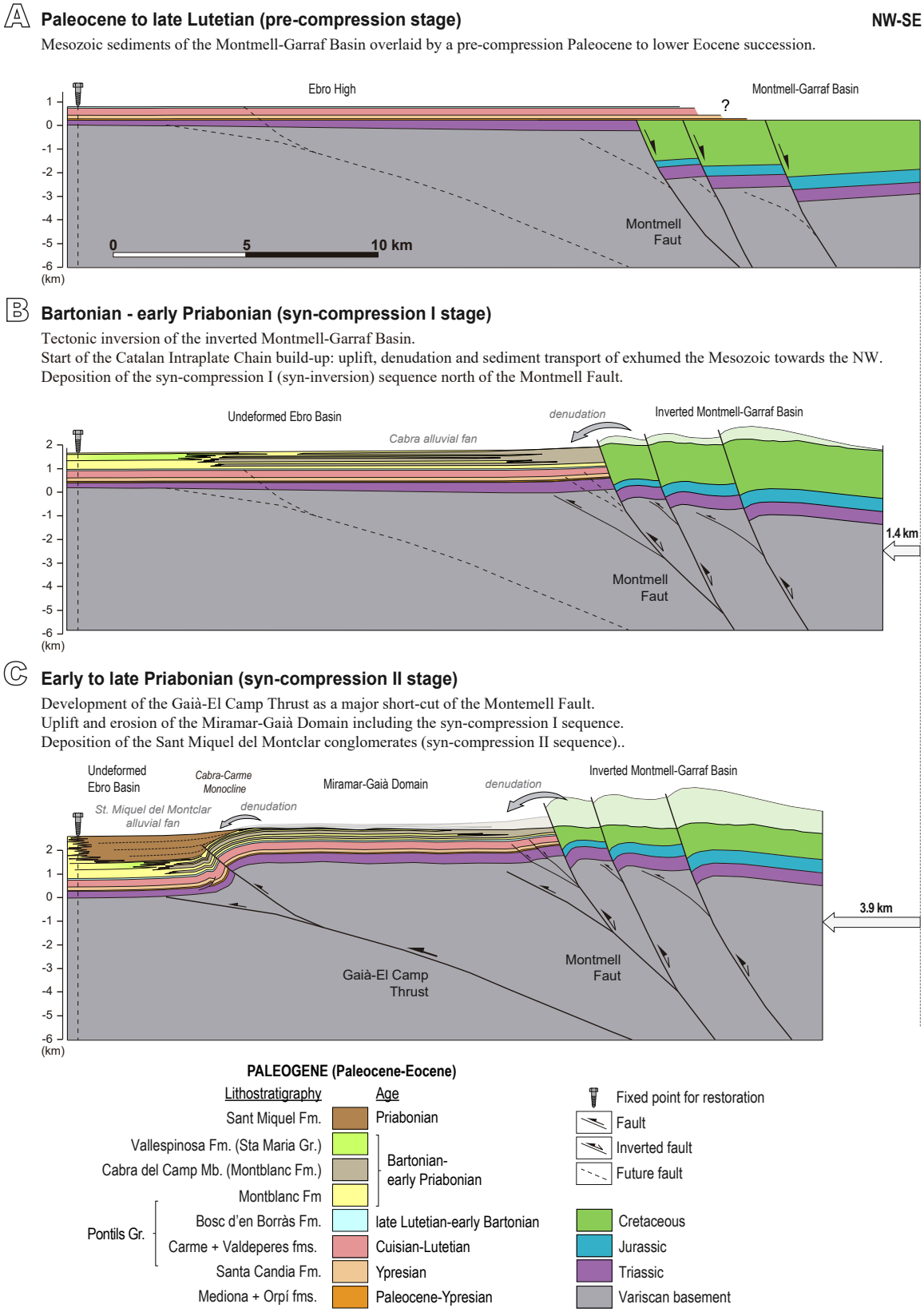

FIGURE 10. Schematic sequential structural restoration of the Gaià-Montmell section applying flexural slip and bed length preservation. A) late Lutetian pre-compressional stage. B) late Lutetian – middle Bartonian syn-compressional stage. C) middle Bartonian to late Priabonian latest stages of the compressional stage. No vertical exaggeration.

possibly, Senonian) and lower to middle Eocene (Ypresian-Lutetian). Despite the current levels of erosion south of the Montmell Fault in the Miramar-Gaià Domain does not allow the recognition of rocks younger than Paleocene (Figs. 2B, C), an alluvial system at the footwall of the Montmell Fault and extending up to the present-day location of Cabra del Camp is proposed for this period (Cabra alluvial fan, Fig. 10B). This reconstruction contemplates the presence of (unpreserved) proximal alluvial facies at the foothills of the inverted Montmell-Garraf Basin laterally changing to distal facies towards the northwest above the still inactive Gaià-El Camp Thrust. This reconstruction is supported by the measured NW-directed paleocurrents and the fact that one of the main sources of the sediments consisted of Cretaceous rocks comparable to the formations described in the Mesozoic basins located southeast of the study area (*e.g.* Montmell-Garraf) (Esteban, 1973; Esteban and Robles, 1976; Martín-Closas *et al.*, this volume; Moreno-Bedmar *et al.*, 2017; Salas *et al.*, 2001). Consequently, the conglomerate beds currently outcropping in the surroundings of Cabra del Camp in the Ebro Basin margin (Cabra del Camp Mb., Fig. 4) can be described as the distal remains of an alluvial system that expanded over the Miramar-Gaià Domain (Fig. 10B). To the northwest, the Cabra alluvial system would laterally transition into the finer-grained facies of the Montblanc Fm. and the marine sediments of the Vallespinosa Fm. (Fig. 4B)

The beginning of the inversion and the uplift of the Montmell-Garraf Basin can be stablished from the paleomagnetic analysis performed in sediments of the Santa Maria and Barberà-Anoia groups (Fig. 8), which constrains the age of the base of the Montblanc Fm. and its lateral equivalent the Cabra del Camp Mb. (Figs. 4; 5) as early Bartonian (41Ma). This age of initial contractional movements and inversion agrees with the fact that the compressional deformation in the CCR progressed from northeast to southwest up to the middle Oligocene (Anadón *et al.*, 1985; Guimerà, 1984; Guimerà and Santanach, 1978). The earliest syn-tectonic sediments recorded along the SE Ebro Basin margin are the early Eocene Cairat Fm. (Ypresian-early Cuisian in age), which were deposited northeast of the study area in the Montserrat-Sant Llorenç del Munt area (López-Blanco, 2002) (Fig. 2A).

The compressional deformation continued and the whole ensemble of the Miramar-Gaià Domain became uniformly uplifted by the Gaià-El Camp Thrust (Fig. 10C), a low-angle thrust previously interpreted as a major footwall shortcut that provided a smoother fault trajectory during the inversion of the Montmell Fault (Marín *et al.*, 2021). The emplacement of the Gaià-El Camp Thrust is the responsible of the Cabra-Carme Monocline formation, which represents the deformation front of the CCR. The deformation was first accommodated within a trishear triangular zone developed at the tip of the Gaià-El Camp Thrust. As deformation progressed, an out-of-syncline back-thrust developed to accommodate the shortening, folding the previously deposited syn-compression I succession (Figs. 5; 10C; 11) and resulting in the characteristic anticline-syncline pair observed north of Cabra del Camp (Fig. 4). Similar out-of-syncline structures have been previously recognized in the Miramar Range southwest of the study area by Gómez and Guimerà (1999) (see map in Fig. 2B for location).

The Sant Miquel conglomerates were deposited during this period as the result of the uplift, denudation, and transport of coarse-grained sediments from the adjoining reliefs towards the southeast (Fig. 10C). The projection of topographically higher dip data from the Sant Miquel Fm.

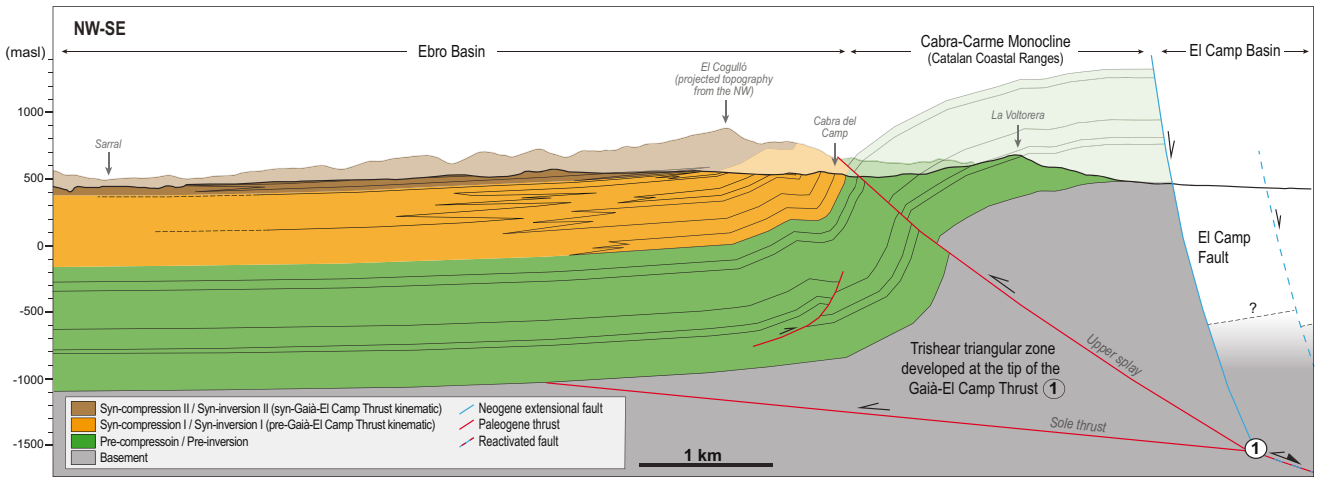

FIGURE 11. Geological cross-section of the SE margin of the Ebro Basin across the locality of Cabra del Camp showing the tectono-sequences differentiated by the tectono-stratigraphic analysis. See Figure 4 for section location.

located to the northeast (Fig. 5), shows that this formation probably onlaps and/or truncates the strata underneath. The internal structure of these conglomerates seen northeast of the Vallespinosa town (Fig. 4), which includes at least two intraformational angular unconformities (López-Blanco *et al.*, 2025), is coherent with its deposition during the coeval development of the Cabra-Carme Monocline. The observed geometries would suggest that this monocline developed following a limb rotation model that generated a fan of beds with intraformational unconformities (Fig. 10C). This fact agrees with the interpretation of the frontal structure as a fault-propagation fold developed by a triangular shear zone at the tip of the Gaià-El Camp Thrust (Marín *et al.*, 2021).

If we consider the results of the magnetostratigraphic analysis (Fig. 8) and the above-mentioned geometrical relationships of the Sant Miquel conglomerates, it is possible to refine the age of the deformation as Priabonian and not late Bartonian as previously suggested by Marín *et al.* (2021). The end of the compressional deformation is difficult to establish in the study area considering that the stratigraphic record is limited. However, it probably ended in the uppermost Priabonian, as suggested by the end of the conglomeratic sedimentation and the presence of lacustrine facies that would denote tectonic quiescence (Anadón *et al.*, 1985, 1989).

Combining thickness and precise age control provided by magnetostratigraphic analysis sedimentation rates have been calculated for the Pontils magnetostratigraphic section. The evolution of these sedimentation rates shows a tight correlation with the deduced tectonic evolution of the Ebro Basin margin (Fig. 8B). The calculated values for the Pontils Group and Montblanc Formation (10.6cm/kyr and 7.3cm/kyr, respectively) show, in average, the lowest sedimentation rates of the section. These low values correspond to areas of low subsidence attributed to a relative quiescence episode during the Late Lutetian pre-compression stage (Fig. 10A). The Bartonian-early Priabonian units (Vallespinosa and Riu de Boix Formations) show higher sedimentation rates (9.8cm/kyr and 13.6cm/kyr, respectively). These values still represent relatively low subsidence rates. However, they correspond to syn-compression I stage (Fig. 10B) and thus, associated to the first significant compressional period in the study area. In this case, it can be interpreted that the inversion of high-angle faults bounding the Montmell-Garraf Basin did not induce a major change in subsidence rates. However, the increasing trend in sedimentation rates would record a progressive rise in subsidence rates due to a change in the tectonic activity. The calculated values for Sant Miquel Formation imply an abrupt increase in the sedimentation rates of up to 51.2cm/kyr. This shift corresponds to the beginning of the early Priabonian late Priabonian syn-compression II stage (Fig. 10C) and can be interpreted as related to the continuation of the Montmell-Garraf Basin inversion and mostly to the onset of the Gaia-El Camp emplacement. This resulted in a major load of basement units causing an increase in subsidence rates in the basin. However, this period (C16n and C15r) also shows relatively high sedimentation rates in other sections and sub-basins from the South-Pyrenean foreland (Garcés *et al.*, 2020). In these other areas, the increase in values has been interpreted as being related to the disconnection of the South-Pyrenean foreland from the Atlantic Ocean (Garcés *et al.*, 2020). Thus, the abrupt increase in sedimentation rates observed in the Pontils section could be interpreted as a combination of the basin margin tectonics and the evolution of the Ebro Basin from exoreic to endorheic conditions during C16n (Costa *et al.*, 2010). The final decrease in the sedimentation rates from 51.2cm/kyr to 22cm/kyr (in C15r and C15n respectively) at the top of Sant Miquel Fm. can be interpreted as related either to the end of the whole syn-compression stage or to a gradual return to trends of the previous externally drained stage (Garcés *et al.*, 2020). This decreasing trend is also recorded by the very low sedimentation rates (6 cm/kyr) in C13r at the neighbouring Sarral section (Barberà *et al.*, 2001) corresponding to the strata just overlying the Sant Miquel conglomerates.

Additionally, the results of the provenance analysis in clasts from the Sant Miquel conglomerates indicate that Barremian-Aptian orbitolinids and Ypresian (Ilerdian) *Alveolina* are prevalent throughout the studied samples. This denotes the continuation of tectonic inversion of the Montmell Fault, the uplift and denudation of the Montmell-Garraf Basin and, the potential cannibalization of the proximal zones of the previously deposited Cabra alluvial system (Fig. 10C). In terms of Paleogene compression, uplift and its related denudation, significant erosion estimates of up to 2-3km are reported from fission-track thermal modelling southwest of the study area in an equivalent structural position in the Prades Block (Fig. 2A) (Juez-Larré and Andriessen, 2002).

CONCLUSIONS

The integration of a new geological map, structural analysis as well as magnetostratigraphic and provenance analyses has allowed the refinement of the tectono-stratigraphic evolution of the central Catalan Coastal Ranges (CCR) and the SE margin of the Ebro Basin during the Paleogene compression.

The correlation of the new Pontils magnetostratigraphic section with the Geomagnetic Polarity Time Scale allows constraining the absolute ages of the Paleogene stratigraphic units along more than 1,400m of succession from Lutetian to Priabonian. The sedimentation of the uppermost Carme

Fm. occurred during the late Cuisian, while the Valldeperes and the Bosc d'en Borràs formations occurred during the Lutetian. The age of the deposition of the Vallespinosa and Montblanc formations (including the Cabra del Camp Mb.) has been established as Bartonian to early Priabonian. The paleomagnetic study also dates the Pontils fossil site (MP15 reference level) as Bartonian, ranging from 41 to 39.8Ma.

The conglomerates of the Cabra del Camp Mb. correspond to distal facies of an alluvial system (Cabra alluvial system). This system expanded to the northwest of the Montmell Fault over the Miramar-Gaià Domain due to the onset of compression and the tectonic inversion of the fault during the Bartonian to early Priabonian. This proposed age refines previous estimates for the timing of the Montmell Fault inversion that placed the reactivation in the late Ypresian (Cuisian). Additionally, it aligns with the diachronous record of the compression observed along the SE margin of the Ebro Basin, where the timing varies from Ypresian in the northern sector to Bartonian in the central area, and middle to late Eocene in the south.

The provenance analysis of the Cabra del Camp conglomerates indicates that the source area of this alluvial system was located southeast of the studied area and corresponded to the Montmell-Garraf Basin. The proximal facies of Cabra alluvial system would have been located in the footwall of the Montmell Fault although these have not been preserved due to later uplift and denudation. The composition of clasts suggests that the Mesozoic Basin included Upper Cretaceous (Cenomanian, Turonian and minor Senonian), and Lower Cretaceous (Barremian-Aptian) strata. The Mesozoic Basin was overlaid by Paleocene to Lutetian sediments (Mediona and Orpí formations and Pontils-Cornudella Group), which confirms this as a period of tectonic quiescence. However, the extent of these Paleogene successions towards the southeast remains uncertain.

A second pulse of compression is recorded by intraformational angular unconformities in the conglomerates of the Sant Miquel Formation (syn-compression II stage) during the Priabonian. The deformation of these conglomerates is associated with the growth of a fault-propagation fold known as the Cabra-Carme Monocline, which resulted from the emplacement of the Gaià-El Camp Thrust. This thrust uplifted the Miramar-Gaià Domain over the Ebro Basin. The Cabra-Carme Monocline constitutes the deformation front of the CCR at this location. Additionally, out-of-syncline backthrusting deformed the previously deposited syn-compression I sequence, which includes the conglomerates of the Cabra del Camp Mb. The beginning of this stage is marked by the abrupt increase in the sedimentation rates, which is related to the increase in the tectonic subsidence caused by the onset of the Gaià-El Camp low angle thrust.

ACKNOWLEDGMENTS

The authors thank the Paleomagnetic Laboratory CCiTUB - Geo3BCN (CSIC) for the support on paleomagnetic analyses. We would like to thank the kind and useful review performed by Drs. Antonio Casas and Mar Moragas as well as the Editor, Dr. Joan Guimerà, and finally, all the staff members of Geologica Acta for handling the paper. This research has been carried out within the framework of the following projects: the IBERINSULA (PID2020-113912GB-I00), funded by MCIN/AEI/10.13039/501100011033; the MCIN Project IMPACSIS (PID2019-106440GB-C21) European Regional Development Fund (ERDF); the SABREM-PID2020-117598GB-I00 funded by MCIN/AEI/10.13039/501100011033; the DGICYT PID2021-122467NB-C22 Ministerio de Ciencia, Innovación y Universidades/Agencia Estatal de Investigación/Fondo Europeo de Desarrollo Regional; GEODIGIT (TED2021-130602B-I00) research projects funded by MCIN/AEI/10.13039/501100011033 for the European Union "NextGenerationEU"/PRTR. The Grups Consolidats de Recerca "Geologia Sedimentària" (2021-SGR-Cat 00349) and "Geodinàmica i Anàlisi de Conques" (2021-SGR 00076) of the Generalitat de Catalunya, and the UB Geomodels Research Institute are also acknowledged. The research has also been benefited by the project "Caracterització litoestratigràfica i estructural i cartografia geològica del Paleogen dels fulls de Sarral (67-31) i Montblanc (67-32) del Mapa Geològic de Catalunya 1:25000" funded by the Institut Cartogràfic i Geològic de Catalunya.

REFERENCES

Agustí, J., Anadón, P., Arbiol, S., Cabrera, L., Colombo, F., Sáez, A., 1987. Biostratigraphical characteristics of the Oligocene sequences of north-eastern Spain (Ebro and Campins basins). Münchner Geowissenshaften Abhandlungen (A), 10, 35-42.

Albrich, S., Bernaus, J.M., Boix, C., Caus, E., Martín-Closas, C., Salas, R., Vicedo, V., Villalonga, R., 2006. Caracterización bioestratigráfica y paleoambiental del Cretácico Inferior (Berriasiense-Barremiense) del Macizo de Garraf (Cadena Costera Catalana). Revista Española de Micropaleontología, 38(2-3), 429-451.

Al-Hajeri, M.M., Al-Saeed, M., Derks, J., Fuchs, T., Hantschel, T., Kauerauf, A., Neumaier, M., Schenk, O., Swientek, O., Tessen, N., Welte, D., Wygrala, B., Kornpihl, D., Peters, K., 2009. Basin and petroleum system modeling. Oilfield Review, 21(2), 14-29

Amilibia, A., Sàbat, F., McClay, K.R., Muñoz, J.A., Roca, E., Chong, G., 2008. The role of inherited tectono-sedimentary architecture in the development of the central Andean Mountain belt: Insights from the Cordillera de Domeyko. Journal of Structural Geology, 30(12), 1520-1539.

Anadón, P., 1978a. El Paleógeno continental anterior a la transgresión biarrtziense (Eoceno medio) entre los ríos Gaia y Ripoll. PhD Thesis. Barcelona, University of Barcelona, 267pp.

Anadón, P., 1978b. El Paleógeno continental anterior a la transgresión biarrtziense (Eoceno medio) entre los ríos Gaiá y Ripoll. Estudios Geológicos, 157pp.

Anadón, P., Feist, M., 1981. Charophytes et biostratigraphie du Paléogène inférieur du bassin de l'Ebre oriental. Palaeontographica Abteilung B, 178, 143-168.

Anadón, P., Marzo, M., 1986. Sistemas deposicionales eocenos del margen oriental de la cuenca del Ebro: Sector Igualada-Montserrat. In: Anadón, P., Cabrera, Ll. (eds.). XI Congreso Español de Sedimentología: guía de las excursiones. Barcelona, 4.1-4.59.

Anadón, P., Colombo Piñol, F., Esteban Cerdà, M., Marzo Carpio, M., Robles Orozco, S., Santanach, P., Solé Sugrañes, L., 1979. Evolución tectonoestratigráfica de los Catalánides. Acta Geologica Hispánica, 14 (1, Hommage to Lluís Solé i Sabaris), 242-270.

Anadón, P., Feist, M., Hartenberger, J.L., Muller, C., Villalta-Comella, J., 1983. Un exemple de correlation biostratigraphique entre échelles marines et continentales dans l'Éocène: la coupe de Pontils (Bassin de l' Ebre, Espagne). Bulletin de la Société Géologique de la France, XXV(5), 747-755.

Anadón, P., Cabrera, L., Guimerà, J., Santanach, P., 1985. Paleogene strike-slip deformation and sedimentation along the southeastern margin of the Ebro Basin, In: Biddle, K.T., Christie-Blick, N. (eds.). Strike-Slip Deformation, Basin Formation, and Sedimentation. The Society of Economic Paleontologists and Mineralogists, 303-318. DOI: https://doi.org/10.2110/pec.85.37.0303

Anadón, P., Cabrera, L., Colombo, F., Marzo, M., Riba, O., 1986. Syntectonic intraformational unconformities in alluvial fan deposits, eastern Ebro Basin margins (NE Spain). In: Allen, P.A., Homewood, P. (eds.). Foreland basins. nternational Association of Sedimentologists, 8 (Special Publication), 259-271.

Anadón, P., Vianey-Liaud, M., Cabrera, L., Hartenberger, J.L., 1987. Gisements à vertébrés du paléogène de la zone orientale du bassin de l'Ebre et leur apport à la stratigraphie. Paleontologia i Evolució, 21, 117-131.

Anadón, P., Cabrera, L., Colldeforns, B., Sáez, A., 1989. Los sistemas lacustres del Eoceno superior y Oligoceno del sector oriental de la Cuenca del Ebro. Acta Geologica Hispánica, 24(3-4), 205-230.

Anadón, P., Cabrera, L., Choi, S.J., Colombo, F., Feist, M., Sáez, A., 1992. Biozonación del Paleógeno continental de la zona oriental de la Cuenca del Ebro mediante carófitas: implicaciones en la biozonación general de carófitas de Europa occidental. Acta Geologica Hispánica, 27(1-2), 69-94.

Andeweg, B., 2002. Cenozoic tectonic evolution of the Iberian Peninsula: effects and causes of changing stress fields. PhD Thesis. Amsterdam, Vrije Universiteit, 178pp.

Angrand, P., Mouthereau, F., 2021. Evolution of the Alpine orogenic belts in the Western Mediterranean region as resolved by the kinematics of the Europe-Africa diffuse plate boundary. BSGF-Earth Sciences Bulletin, 192(1), 44pp. DOI: https://doi.org/10.1051/bsgf/2021016

Angrand, P., Mouthereau, F., Masini, E., Asti, R., 2020. A reconstruction of Iberia accounting for Western Tethys–North Atlantic kinematics since the late-Permian–Triassic. Solid Earth, 11(4), 1313-1332. DOI: https://doi.org/10.5194/se-11-1313-2020

Arasa-Tuliesa, A., Cabrera, L., 2018. Neogene-Quaternary onshore record in the lower Ebro River incised palaeovalley (Ebro margin, Catalan Coastal Range, NE Iberia). Geologica Acta, 16(3), 265-292.

Arche, A., Evans, G., Clavell, E., 2010. Some considerations on the initiation of the present SE Ebro River drainage system: Post- or pre-Messinian? Journal of Iberian Geology, 36(1), 73-85.

Arnal, I., Calvet, F., Márquez, L., Márquez-Aliaga, A., Solé de Porta, N., 2002. La plataforma carbonatada epeírica (Formaciones Imón e Isábena) del Triásico superior del Noreste de la Península Ibérica. Acta Geológica Hispánica, 37(4), 299-328.

Baqués, V., Travé, A., Roca, E., Marín, M., Cantarero, I., 2012. Geofluid behavior in successive extensional and compressional events: a case study from the southwestern end of the Vallès-Penedès Fault (Catalan Coastal Ranges, NE Spain). Petroleum Geosciences, 18, 17-31.

Barberà, X., 1999. Magnetostratigrafia de l'Oligocè del sector sudoriental de la Conca de l'Ebre: implicacions magnetobiocronològiques i seqüencials. PhD Thesis. Barcelona, University of Barcelona, 247pp.

Barberà, X., Cabrera, L., Marzo, M., Parés, J.M., Agustí, J., 2001. A complete terrestrial Oligocene magnetobiostratigraphy from the Ebro Basin, Spain. Earth and Planetary Science Letters, 187, 1-16.

Bartrina, M.T., Cabrera, L., Jurado, M.J., Guimerà, J., Roca, E., 1992. Evolution of the central Catalan margin of the Valencia trough (western Mediterranean). Tectonophysics, 203(1-4), 219-247.

Beamud, E., 2013. Paleomagnetism and thermochronology in Tertiary syntectonic sediments of the South-Central Pyrenees: Chronostratigraphy, kinematic and exhumation constraints. PhD Thesis. Barcelona, University of Barcelona, 251pp.

Beamud, E., Garcés, M., Cabrera, L., Muñoz, J.A., Almar, Y., 2003. A new late Eocene continental chronostratigraphy from NE Spain. Earth and Planetary Science Letters, 216, 501-514.

Beamud, E., Costa, E., Garcés, M., Cabrera, L., Roca, E., Gómez-Paccard, M., 2012. An integrated Eocene chronostratigraphy for the central sector of the SE margin of the Ebro Basin. Geotemas, 13, 1116-1119.

Benzaquen, M., Nuñez, A., Martínez, W., 1973. Hoja nº 418 (Montblanc), Mapa Geológico de España E. 1: 50.000. Segunda Serie (MAGNA). Madrid, Instituto Geológico y Minero de España.

Bonilla-Salomón, I., Minwer-Barakat, R., Vianey-Liaud, M., Moyà-Solà, S., 2016. Middle Eocene rodents from Sant Jaume de Frontanyà (eastern Pyrenees, northern Spain) and biochronological implications. Journal of Vertebrate Paleontology, 36(4), e1121149. DOI: https://doi.org/10.1080/02724634.2016.1121149

Boyer, S.E., Elliott, D., 1982. Thrust systems. American Association of Petroleum Geologists (AAPG) Bulletin, 66(9), 1196-1230.

Burbank, D.W., Verges, J., Munoz, J.A., Bentham, P., 1992. Coeval hindward-and forward-imbricating thrusting in the south-central Pyrenees, Spain: Timing and rates of shortening and deposition. Geological Society of America Bulletin, 104(1), 3-17.

Busquets, P., Ortí, F., Pueyo, J.J., Riba, O., Sáez, A., Salas, R., Taberner, C., 1985. Evaporite deposition and diagenesis in the saline (potash) Catalan basin, Upper Eocene. Lleida (Spain), Excursion Guidebook 6th European Meeting, 13-59.

Busquets, P., Ramos Guerrero, E., Moya, S., Agusti, J., Colombo, F., Checa, L., Kohler, M., 1992. La Formación de Bellmunt (Unidad del Cadi, Pirineo Oriental); aportaciones bioestratigráficas de los sistemas lacustres y palustres asociados. Acta Geologica Hispánica, 27, 109-116.

Butler, R.W.H., 1982. The terminology of structures in thrust belts. Journal of structural Geology, 4(3), 239-245.

Butler, R.W.H., 1987. Thrust sequences. Journal of the Geological Society, 144(4), 619-634.

Butler, R.W.H., 1989. The influence of preexisting basin structure on thrust system evolution in the Western Alps. In: Cooper, M.A., Williams, G.D. (eds.). Inversion Tectonics. London, The Geological Society, 44 (Special Publications), 105-122.

Calvet, F., Marzo, M., 1994. El Triásico de las Cordilleras Costero Catalanas: estratigrafía, sedimentología y análisis secuencia. In: Arche, A. (ed.). Field guide III. Cuenca, Coloquio de Estratigrafía y Sedimentología del Triásico y Pérmico de España, 1-53.

Cantarero, I., Travé, A., Alías, G., Baqués, V., 2014a. Polyphasic hydrothermal and meteoric fluid regimes during the growth of a segmented fault involving crystalline and carbonate rocks (Barcelona Plain, NE Spain). Geofluids, 14, 20-44.

Cantarero, I., Lanari, P., Vidal, O., Alías, G., Travé, A., Baqués, V., 2014b. Long-term fluid circulation in extensional faults in the central Catalan Coastal Ranges: P-T constraints from neoformed chlorite and K-white mica. International Journal of Earth Sciences, 103, 165-188.

Carminati, E., Wortel, M.J.R., Meijer, P.T., Sabadini, R., 1998. The two-stage opening of the western–central Mediterranean basins: a forward modeling test to a new evolutionary model. Earth and Planetary Science Letters, 160(3-4), 667-679.

Carrera, N., López-Blanco, M., Arbués, P., Beamud, E., Garcés, M., Marín, M., Cabrera, L., 2020. Caracterització litostratigràfica i estructural i cartografia geològica del Paleogen dels fulls de Sarral (67-31) i Montblanc (67-32) del Mapa Geològic de Catalunya 1:25000. Institut Cartogràfic i Geològic de Catalunya, Technical Report CG-0006/20, unpublished, 70pp.

Colldeforns, B., unpublished. Mapa Geològic de Catalunya. 1:25.000, Sheet nº 418-2-1 (68-31) (Querol). Geological map advised by P. Anadón. Barcelona (Spain), Servei Geològic de Catalunya.

Colldeforns, B., Anadón, P., Cabrera, L., 1994a. Litoestratigrafía del Eoceno superior-Oligoceno inferior de la zona oriental de la Cuenca del Ebro. Sector Igualada-Santa Coloma de Queralt. Geogaceta, 15, 55-58.

Colldeforns, B., Anadón, P., Cabrera, L., 1994b. Nuevos datos sobre la litoestratigrafía del Eoceno-Oligoceno inferior de la zona suroriental de la Cuenca del Ebro (Sector Pontils-Montblanc, provincias de Tarragona y Barcelona). Geogaceta, 16, 98-101.

Colombo, F., 1980. Estratigrafía y sedimentología del Terciario inferior continental de los Catalánides. PhD Thesis. Barcelona, University of Barcelona, 608pp.

Colombo, F., 1986. Continental Paleogene stratigraphy and sedimentology of the western southern border of the Catalanides, Tarragona Province, Spain. Cuadernos de Geología Ibérica, 10, 55-115.

Colombo, F., 1994. Normal and reverse unroofing sequences in syntectonic conglomerates as evidence of progressive basinward deformation. Geology, 22(3), 235-238.

Costa, E., Garcés, M., López-Blanco, M., Beamud, E., Gómez-Paccard, M., Larrasoaña, J.C., 2010. Closing and continentalization of the South Pyrenean foreland basin (NE Spain): magnetochronological constraints. Basin Research, 22(6), 904-917.

Costa, E., Garcés, M., López-Blanco, M., Serra-Kiel, J., Bernaola, G., Cabrera, L., Beamud, E., 2013. The Bartonian-Priabonian marine record of the eastern South Pyrenean foreland basin (NE Spain): a new calibration of the larger foraminifers and calcareous nannofossil biozonation. Geologica Acta, 11(2), 177-193.

Couzens, B.A., Wiltschko, D.V., 1996. The control of mechanical stratigraphy on the formation of triangle zones. Bulletin of Canadian Petroleum Geologists, 44, 165-179.

Coward, M.P., 1994. Inversion tectonics. In: Hancock, P.L. (ed.). Continental Deformation. Pergamon Press, 280-304.

Coward, M.P., Gillcrist, R., Trudgill, B., 1991. Extensional structures and their tectonic inversion in the Western Alps. In: Roberts, A.M., Yielding, G., Freeman, B. (eds.). The Geometry of Normal Faults. Geological Society, 56 (Special Publication), 93-113.

Dañobeitia, J.J., Arguedas, M., Gallart, J., Banda, E., Makris, J., 1992. Deep crustal configuration of the Valencia trough and its Iberian and Balearic borders from extensive refraction and wide-angle reflection seismic profiling. Tectonophysics, 203(1-4), 37-55.

Escudero-Mozo, M.J., Márquez-Aliaga, A., Goy, A., Martín-Chivelet, J., López-Gómez, J., Márquez, L., Arche, A., Plasencia, P., Pla, C., Marzo, M., Sánchez-Fernández, D., 2017. Middle Triassic carbonate platforms in eastern Iberia: evolution of their fauna and palaeogeographic significance in the western Tethys. Palaeogeography, Palaeoclimatology, Palaeoecology, 417, 236-260.

Erslev, E.A., 1991. Trishear fault-propagation folding. Geology, 19(6), 617-620.

Esteban, M., 1973. Petrología de las calizas Cretácicas del Sector Central de los Catalánides (Prov. de Tarragona y Barcelona). PhD Thesis. Barcelona, University of Barcelona, 425pp.

Esteban, M., Robles, S., 1976. Sobre la paleogeografía del Cretácico Inferior de los Catalánides entre Barcelona y Tortosa. Acta Geológica Hispánica, 11(3), 73-78.

Feist, M., Anadón, P., Cabrera, L., Choi, S.J., Colombo, F., Sáez, A., 1994. Upper Eocene-Lowermost Miocene charophyte succession in the Ebro basin (Spain). Contribution to the charophyte biozonation in Western Europe. Newsletters on Stratigraphy, 30(1), 1-32.

Fernández, O., Muñoz, J.A., Arbués, P., Falivene, O., Marzo, M., 2004. Three-dimensional reconstruction of geological surfaces: An example of growth strata and turbidite systems from the Ainsa basin (Pyrenees, Spain). American Association of Petroleum Geologists (AAPG) Bulletin, 88(8), 1049-1068.

Ferrer, J., 1971. El Paleoceno y Eoceno del borde suroriental de la Depresión del Ebro (Cataluña). Mémoires suisses de Paléontologie, 90, 1-70.

Ferrer, O., Carola, E., McClay, K., 2023. Structural control of inherited salt structures during inversion of a domino basement-fault system from an analogue modelling approach. Solid Earth, 14(5), 571-589.

Ferrill, D.A., Morris, A.P., 2008. Fault zone deformation controlled by carbonate mechanical stratigraphy, Balcones fault system, Texas. American Association of Petroleum Geologists (AAPG) Bulletin, 92(3), 359-380.

Fontboté, J.M., Guimerà, J., Roca, E., Sàbat, F., Santanach, P., Fernández-Ortigosa, F., 1990. The Cenozoic geodynamic evolution of the Valencia trough (western Mediterranean). Revista Sociedad Geológica de España, 3(3-4), 249-259.

Ford, M., Williams, E.A., Artoni, A., Vergés, J., Hardy, S., 1997. Progressive evolution of a fault-related fold pair from growth strata geometries, Sant Llorenç de Morunys, SE Pyrenees. Journal of structural Geology, 19(3-4), 413-441.

Galán-Abellán, B., López-Gómez, J., Berrenechea, J.F., Marzo, M., De la Horra, R., Arche, A., 2013. The beginning of the Buntsandstein cycle (Early–Middle Triassic) in the Catalan Ranges, NE Spain: Sedimentary and palaeogeographic implications. Sedimentary Geology, 296, 86-102.

Garcés, M., López-Blanco, M., Valero, L., Beamud, E., Muñoz, J.A., Oliva-Urcia, B., Vinyoles, A., Arbués, P., Cabello, P., Cabrera, L., 2020. Paleogeographic and sedimentary evolution of the South Pyrenean foreland basin. Marine and Petroleum Geology, 113, 104105.

García-Senz, J., Pedrera, A., Ayala, C., Ruiz-Constán, A., Robador, A., Rodríguez- Fernàndez, L.R., 2019. Inversion of the north Iberian hyperextended margin: the role of exhumed mantle indentation during continental collision. London, The Geological Society, 490 (Special Publications), 177-198.

Gaspar-Escribano, J.M., García-Castellanos, D., Roca, E., Cloetingh, S.A.P.L., 2004. Cenozoic vertical motions of the Catalan Coastal Ranges (NE Spain): The role of tectonics, isostasy, and surface transport. Tectonics, 23(1), TC1004.

Gómez, M., Guimerà, J., 1999. Estructura Alpina de la Serra de Miramar y del NE de las Muntanyes de Prades (Cadena Costera Catalana). Revista Sociedad Geológica de España 12(3-4), 405-418.

Gómez-Paccard, M., López-Blanco, M., Costa, E., Garcés, M., Beamud, E., Larrasoaña, J.C., 2011. Tectonic and climatic controls on the sequential arrangement of an alluvial fan/fan-delta complex (Montserrat, Eocene, Ebro basin, NE Spain). Basin Research, 23, 1-19.

Gradstein, F.M., Ogg, J.G., Schmitz, M.D., Ogg, G.M. (eds.)., 2020. Geologic time scale. Elsevier, 159-192.

Gross, M.R., Gutierrez-Alonso, G., Bai, T., Wacker, M.A., Collingsworth, K.B., Behl, R.J., 1997. Influence of mechanical stratigraphy and kinematics on fault scaling relations. Journal of Structural Geology, 19, 171-183.

Guimerà, J., 1984. Paleogene evolution of deformation in the northeastern Iberian Peninsula. Geological Magazine, 121, 413-420.

Guimerà, J., 2018. Structure of an intraplate fold-and-thrust belt: the Iberian Chain. A synthesis. Geologica Acta, 16(4), 427-438.

Guimerà, J., Santanach, P., 1978. Sobre la compresión alpina en el sector central de las Cadenas Costeras Catalanas. Acta Geológica Hispánica, 2(13), 33-42.

Guimerà, J., Álvaro, M., 1990. Structure et évolution de la compression alpine dans la Chaîne ibérique et la Chaîne côtière catalane (Espagne). Bulletin de la Société géologique de France, 6(2), 339-348.

Guimerà, J., Alonso, A., Mas, J.R., 1995. Inversion of an extensional-ramp basin by a newly formed thrust: The Cameros basin (N. Spain). In: Buchanan, J.G., Buchanan, P.G. (eds.). Basin Inversion. Geological Society, 88 (Special Publication), 433-453.

Hardy, S., Poblet, J., McClay, K.R., Waltham, D., 1996. Mathematical modelling of growth strata associated with fault-related fold structures. London, The Geological Society, 99 (1, Special Publications), 265-282.

Hayward, A.B., Graham, R.H., 1989. Some geometrical characteristics of inversion. In: Cooper, M.A., Williams, G.D. (eds.). Inversion Tectonics. London, The Geological Society, 44 (Special Publications), 17-39.

ICGC., 2005. Mapa geològic comarcal de Catalunya 12, Baix Penedès, 1:50.000. Barcelona, Institut Cartogràfic i Geològic de Catalunya.

ICGC., 2018. Mapa geològic de Catalunya, Sant Martí Sarroca 419-1-2 (69-32), 1:25.000. Barcelona, Institut Cartogràfic i Geològic de Catalunya.

Juez-Larré, J., Andriessen, P.A.M., 2002. Post Late Paleozoic tectonism in the southern Catalan Coastal Ranges (NE Spain), assessed by apatite fission track analysis. Tectonophysics, 349, 113-129.

Juez-Larré, J., Andriessen, P.A.M., 2006. Tectonothermal evolution of the northeastern margin of Iberia since the break-up of Pangea to present, revealed by low-temperature fission-track and (U–Th)/He thermochronology. A case history of the Catalan Coastal Ranges. Earth and Planetary Science Letters, 243, 159-180.

Juvany, P., Garcés, M., López-Blanco, M., Martín-Closas, C., Beamud, E., Tosquella, J., Bekkevold, S.E., 2024.

Chronostratigraphy and tectono-sedimentary history of the Eastern South Pyrenean foreland basin (Ripoll Syncline, North-East Spain). The Depositional Record, 10, 338-363. DOI: https://doi.org/10.1002/dep2.287.

Kirschvink, J.L., 1980. The least-squares line and plane and the analysis of paleomagnetic data. Geophysical Journal of the Royal Astronomical Society, 62, 699-718.

Lanaja, J.M., 1987. Contribución de la exploración petrolífera al conocimiento de la Geología de España. Madrid, Instituto Geologico y Minero de España (IGME), Ministerio de Industria y Energía, 465pp.

Lawton, T.F., Roca, E., Guimerà, J., 1999. Kinematic-stratigraphic evolution of a growth syncline and its implications for tectonic development of the proximal foreland basin, southeastern Ebro basin, Catalunya, Spain. Geological Society of America (GSA) Bulletin, 111(3), 412-431.

Llopis, N., 1947. Contribución al conocimiento de la morfoestructura de los Catalánides. PhD Thesis. Barcelona, Instituto Lucas Mallada (CSIC), 373pp.

López-Blanco, M., 2002. Sedimentary response to thrusting and fold growing on the SE margin of the Ebro basin (Paleogene, NE Spain). Sedimentary Geology, 146, 133-154.

López-Blanco, M., Marzo, M., Burbank, D.W., Vergés, J., Roca, E., Anadón, P., Piña, J., 2000a. Tectonic and climatic controls on the development of foreland fan deltas: Montserrat and Sant Llorenç del Munt systems (Middle Eocene, Ebro Basin, NE Spain). Sedimentary Geology, 138(1-4), 17-39.

López-Blanco, M., Marzo, M., Piña, J., 2000b. Transgressive–regressive sequence hierarchy of foreland, fan-delta clastic wedges (Montserrat and Sant Llorenç del Munt, Middle Eocene, Ebro Basin, NE Spain). Sedimentary Geology, 138(1-4), 41-69.

López-Blanco, M., Carrera, N., Arbués, P., Beamud, E., Garcés, M., Marín, M., Cabrera, Ll., Roca, E. Ferrer, O., Gratacos, O., 2024. Relación entre los Conglomerados de Sant Miquel de Montclar (Eoceno, margen SE de la cuenca del Ebro) y las unidades estratigráficas adyacentes. Geo-Temas, 20, 138.

López-Blanco, M., Ma, M., Beamud, E., Marín, M., Costa, E., 2025. New evidence of synsedimentary folding of the Sant Miquel de Montclar conglomerates (Eocene, Ebro basin, NE Spain). Geogaceta, 77, 35-38.

Magoon, L., 1987. The Petroleum System-A Classification Scheme for Research, Exploration, and Resource Assessment. In: Magoon, L. (ed.). Petroleum Systems of the United States. U.S. Geological Survey Bulletin, 1870, 67pp.

Makeen, Y.M., Abdullah, W.H., Pearson, M.J., Hakimi, M.H., Ayinla, H.A., Elhassan, O.M., Abas, A.M., 2016. History of hydrocarbon generation, migration and accumulation in the Fula sub-basin, Muglad Basin, Sudan: Implications of a 2D basin modeling study. Marine and Petroleum Geology, 77, 931-941.

Marín, M., Roca, E., Marcuello, A., Cabrera, L., Ferrer, O., 2021. Mesozoic structural inheritance in the Cenozoic evolution of the central Catalan Coastal Ranges (western Mediterranean): Structural and magnetotelluric analysis in the Gaià-Montmell High. Tectonophysics, 814, 228970.

Marín, M., Roca, E., Baqués, V., Cantarero, I., Cabrera, L., Ferrer, O., Travé, A., 2023. Fluid-rock interaction control on fault reactivation: A review of the Montmell-Vallès Fault System, central Catalan Coastal Ranges (NE Iberia). Global and Planetary Change, 220, 104011.

Martín-Closas, C., Vicente, A., Pérez-Cano, J., Sanjuan, J., Bover-Arnal, T., 2018. On the earliest occurrence of Tolypella section Tolypella in the fossil record and the age of major clades in extant Characeae. Botany Letters, 165, 23-33.

Martín-Closas, C., Albalat, D., Colombo, F., Vilà, M., Vicente, A., Ossó, A., 2025. A new Iberian refugium for charophytes during the maximum post-Palaeozoic sea-level high stand in Europe: the Cenomanian-Turonian of Tarragona (Catalonia, Spain). Geologica Acta, 23.7.

McClay, K.R., 1992. Glossary of thrust tectonics terms. In: McClay K.R. (ed.). Thrust tectonics. Springer Science & Business Media, 419-433.

Mercedes-Martín, R., Arenas, C., Salas, R., 2014. Diversity and factors controlling widespread occurrence of syn-rift Ladinian microbialites in the western Tethys (Triassic Catalan Basin, NE Spain).Sedimentary Geology, 313, 68-90.

Mercedes-Martín, R., Buatois, L.A., 2020. Microbialites and trace fossils from a Middle Triassic restricted carbonate ramp in the Catalan Basin, Spain: evaluating environmental and evolutionary controls in an epicontinental setting. Lethaia, 54(1), 4-25.

Minwer-Barakat, R., Bolet, A., Anadón, P., Alegret, L., Badiola, A., Blanco, A., Cotton, L., Femenias-Gual, J., Furió, M., Godinot, M., Moyà-Solà, S., Peláez-Campomanes, P., Sanjuan, J., Marigó, J., 2023. The fossil assemblage from Pontils, a middle Eocene primate-bearing locality from Northeastern Spain. Journal of Vertebrate Paleontology, 43, e2259970. DOI: https://doi.org/10.1080/02724634.2023.2259970

Mitra, S., 2002. Fold-accommodation faults. American Association of Petroleum Geologists (AAPG) Bulletin, 86(4), 671-693.

Moreno-Bedmar, J.A., Robert, E., Matamales-Andreu, R., Bover-Arnal, T., 2017. Review of the early Albian ammonites of the Montmell Formation near Marmellar (Salou-Garraf Basin, Tarragona, Catalonia, Spain). Carnets de Géologie, 17(1), 1-10. DOI: 10.4267/2042/62038

Mouthereau, F., Filleaudeau, P.-Y., Vacherat, A., Pik, R., Lacombe, O., Fellin, M.G., Castelltort, S., Christophoul, F., Masini, E., 2014. Placing limits to shortening evolution in the Pyrenees: Role of margin architecture and implications for the Iberia/Europe convergence. Tectonics, 33, 2283-2314.

Moyà-Solà, S., Kohler, M., 1993. Middle Bartonian locality with Anchomomys (Adapidae, Primates) in the Spanish Pyrenees: preliminary report. Folia Primatologica, 60, 158-163. DOI: https://doi.org/10.1159/000156684.

Muñoz, J.A., 1992. Evolution of a continental collision belt: ECORS-Pyrenees crustal balanced cross-section. In: McClay, K. (ed.). Thrust Tectonics. London, Chapman & Hall, 235-246.

Muñoz, J.A., 2017. Fault-related folds in the southern Pyrenees. American Association of Petroleum Geologists (AAPG) Bulletin, 101(4), 579-587.

Nebot, M., Guimera, J., 2016. Structure of an inverted basin from subsurface and field data: the Late Jurassic-Early Cretaceous Maestrat Basin (Iberian Chain). Geologica Acta, 14(2), 155-177.

Ortí, F., Pérez-López, A., Salvany, J.M., 2017. Triassic evaporites of Iberia: sedimentological and palaeogeographical implications for the western Neotethys evolution during the Middle Triassic–Earliest Jurassic. Palaeogeography, Palaeoclimatology, Palaeoecology, 471, 157-180.

Pueyo, J.J., 1975. Estudio petrológico y geoquímico de los yacimientos potásicos de Cardona, Súria, Sallent (Barcelona, España). PhD Thesis. Barcelona, University of Barcelona, 351pp.

Reguant, S., 1967. El Eoceno marino de Vic (Barcelona). Memorias Instituto Geológico y Minero de España, 68, 1-350.

Riba, O., 1973. Las discordancias sintectónicas del Alto Cardener (Prepirineo catalán), ensayo de interpretación evolutiva». Acta Geológica Hispánica, VIII(3), 90-99.

Riba, O., 1976. Syntectonic unconformities of the Alto Cardener, Spanish Pyrenees: A genetic interpretation. Sedimentary Geology, 15(3), 213-233.

Robles, S., 1982. Catalánides. In: García, A. (ed.). El Cretácico de España. Madrid, Universidad Complutense de Madrid, 199-272.

Roca, E., 1994. La evolución geodinámica de la Cuenca Catalano-Balear y áreas adyacentes desde el Mesozoico hasta la actualidad. Acta Geológica Hispánica, 29, 3-26.

Roca, E., 2001. The Northwest-Mediterranean basin (Valencia Trough, Gulf of Lions and Liguro-Provencal basins): structure and geodynamic evolution. In: Ziegler, P.A., Cavazza, W., Robertson, A.H.F., Crasquin-Soleau, S. (eds.). Peri-Tethys Memoir 6: Peri-Tethyan Rift/Wrench Basins and Passive Margins. French National Museum of Natural History, 186, 671-706.

Roca, E., Guimerà, J., 1992. The Neogene structure of the eastern Iberian margin: structural constraints on the crustal evolution of the Valencia trough (western Mediterranean). Tectonophysics, 203(1-4), 203-218.

Roca, E., Frizon de Lamotte, D., Mauffret, A., Bracène, R., Vergés, J., Benaouali, N., Fernàndez, M., Muñoz, J.A., Zeyen, H., 2004. Transect II: Aquitaine Basin - Pyrenees - Ebro Basin - Catalan Range - Valencia Trough - Balearic Block - Algerian Basin - Kabylies - Atlas - Saharan Platform. In: Cavazza, W., Roure, F.M., Spakman, W., Stampfli, G.M., Ziegler, P.A. (eds.). 2004. The Transmed Atlas – The Mediterranean Region from Crust to Mantle. Berlin, Heidelberg, Springer, CD.

Roest, W.R., Srivastava, S.P., 1991. Kinematics of the plate boundaries between Eurasia, Iberia and Africa in the North Atlantic from the Late Cretaceous to the present. Geology, 19, 613-616.

Romagny, A., Jolivet, L., Menant, A., Bessière, E., Maillard, A., Canva, A., Gorini, Ch., Augier, R., 2020. Detailed tectonic reconstructions of the Western Mediterranean region for the last 35 Ma, insights on driving mechanisms. Bulletin de la Société géologique de France, 191, 1-45.

Rosenbaum, G., Lister, G.S., Duboz, C., 2002. Relative motions of Africa, Iberia and Europe during Alpine orogeny. Tectonophysics, 359, 117-129.

Sàbat, F., Roca, E., Muñoz, J.A., Vergés, J., Sans, M., Masana, E., Estévez, A., Santisteban Bove, C.D., 1995. Role of extension and compression in the evolution of the eastern margin of Iberia: The ESCI-Valencia Trough seismic profile. Revista Sociedad Geológica de España, 8(4), 431-448.

Salas, R., 1987. El Malm i el Cretaci inferior entre el Massís de Garraf i la Serra d'Espadà. Anàlisi de Conca. PhD Thesis. Barcelona, University of Barcelona, 541pp.

Salas, R., Casas, A., 1993. Mesozoic extensional tectonics, stratigraphy and crustal evolution during the Alpine cycle of the eastern Iberian basin. Tectonophysics, 228(1-2), 33-55.

Salas, R., Guimerà, J., Mas, R., Martin-Closas, C., Melendez, A., Alonso, A., 2001. Evolution of the Mesozoic central Iberian Rift System and its Cainozoic inversion (Iberian chain). Mémoires du Muséum National d'Histoire Naturelle, 186, 145-186.

Salvini, F., Storti, F., 2002. Three-dimensional architecture of growth strata associated to fault-bend, fault-propagation, and décollement anticlines in non-erosional environments. Sedimentary Geology, 146(1-2), 57-73.

Sanjuan, J., Martín-Closas, C., Costa, E., Barberà, X., Garcés, M., 2014. Calibration of Eocene-Oligocene charophyte biozones in the Eastern Ebro Basin (Catalonia, Spain). Stratigraphy, 11(1), 61-81.

Schlagintweit, F., Bover-Arnal, T., 2013. Remarks on *Bačinella* Radoičić, 1959 (type species *B. irregularis*) and its representatives. Facies, 59, 59-73.

Schmidt-Kittler, N., 1987. International Symposium on Mammalian biostratigraphy and paleoecology of the European Paleogene - Mainz, february 18th-21st. Müncher Geowissenschaftliche Abhandlungen, 10, 312pp.

Scisciani, V., Tavarnelli, E., Calamita, F., 2001. Styles of tectonic inversion within synorogenic basins: examples from the Central Apennines, Italy. Terra Nova, 13, 321-326.

Serra-Kiel, J., Travé, A., Mató, E., Saula, E., Ferràndez, C., Tosquella, J., Vergés, J., 2003. Marine and transitional Middle/Upper Eocenen units of the Southeastern Pyrenean Foreland Basin (NE Spain). Geologica Acta, 1(2), 177-200.

Srivastava, S.P., Roest, W.R., Kovacs, L.C., Oakey, G., Lévesque, S., Verhoef, J., Macnab, R., 1990. Motion of Iberia since the Late Jurassic: results from detailed aeromagnetic measurements in the Newfoundland Basin. Tectonophysics, 184, 229-260.

Suppe, J., Chou, G.T., Hook, S.C., 1992. Rates of folding and faulting determined from growth strata. In: McClay (ed.). Thrust tectonics. Springer Science & Business Media, 105-121.

Suppe, J., Sàbat, F., Munoz, J.A., Poblet, J., Roca, E., Vergés, J., 1997. Bed-by-bed fold growth by kink-band migration: Sant Llorenç de Morunys, eastern Pyrenees. Journal of Structural Geology, 19(3-4), 443-461. DOI: https://doi.org/10.1016/S0191-8141(96)00103-4

Travé, A., Serra-Kiel, J. Zamarreno, I., 1996. Paleoecological interpretation of transitional environments in Eocene carbonates (NE Spain). Palaios, 11, 141-160.

Tosal, A., Valero, L., Sanjuan, J., Martín-Closas, C., 2019. Influence of short-and long-term climatic cycles on floristic change across the Eocene–Oligocene boundary in the Ebro Basin (Catalonia, Spain). Comptes Rendus Palevol, 18(8), 925-947.

Valero-Montesa, L., Garcés, M., Cabrera, L., Costa Gisbert, E., Sáez, A., 2014. 20 Myr of eccentricity paced lacustrine cycles in the Cenozoic Ebro Basin. Earth and Planetary Science Letters, 408, 183-193.

van Hinsbergen, D.J., Vissers, R.L.M., Spakman, W., 2014. Origin and consequences of western Mediterranean subduction, rollback, and slab segmentation. Tectonics, 33(4), 393-419.

Van Hinsbergen, D.J., Torsvik, T.H., Schmid, S.M., Maţenco, L.C., Maffione, M., Vissers, R.L.M., Gürer, D., Spakman, W., 2020. Orogenic architecture of the Mediterranean region and kinematic reconstruction of its tectonic evolution since the Triassic. Gondwana Research, 81, 79-229.

Vergés, J., Muñoz, J.A., 1990. Thrust sequence in the southern central Pyrenees. Bulletin de la Société géologique de France, 6(2), 265-271.

Vergés, J., García-Senz, J., 2001. Mesozoic evolution and Cenozoic inversion of the Pyrenean Rift. In: Ziegler, P.A., Cavazza, W., Robertson, A.H.F. (eds.). Peri-Tethys memoir 6: Peri-Tethyan Rift/wrench Basins and Passive Margins. Mémoires du Muséum national d'histoire naturelle, 186, 187-212.

Vergés, J., Marzo, M., Muñoz, J.A., 2002. Growth strata in foreland settings. Sedimentary Geology, 146(1-2), 1-9.

Vidal, N., Gallart, J., Dañobeitia, J.J., Díaz, J., 1995. Mapping the Moho in the Iberian Mediterranean margin by multicoverage processing and merging of wide-angle and near-vertical reflection data. In: Banda, E., Torné, M., Talwani, M. (eds.). Rifted Ocean-Continent Boundaries. Proceedings of the NATO Advanced Research Workshop on Rifted Ocean-Continental Boundaries, 291-308.

Virgili, C., 1958. El Triásico de los Catalánides. Boletín del Instituto Geológico y Minero de España, 69, 856pp.

Virgili, C., Cassinis, G., Broutin, J., 2006. Permian to Triassic sequences from selected continental areas of Southwestern Europe. London, The Geological Society, 265 (Special Publications), 231-259.

Manuscript received October 2024;
revision accepted December 2024;
published Online January 2025.

APPENDIX I

3D Digital Outcrop Model of a selected site in the study area. The material needed files to load the model as well as a video of it can be accessed from the following path: https://doi.org/10.7910/DVN/KTJ8EN

TABLE I. Description and attributed ages of the collected samples. See map of Figure 4 for the location of the samples and colors used in the "Sampled formation" column

Sampling site	Sampled formation	Sample ID	Clast/matrix description	Clast/matrix components attributed age/s
01	Montblanc Fm. (Cabra del Camp Mb.)	01a	Conglomerate clasts correspond to dolostone, sandy limestone, mudstone textures, wackestone to packstone bioturbated textures with ostracods and gastropods. grainstone with recrystallized ooids and calcareous algae, grainstone with *Alveolina*, *Opertorbitolites* and miliolids, packstone with small foraminifera, bivalves and serpulids, mudstone-wackestone with characean remains, grainstone with ooids exhibiting radial and concentric coatings, and grainstone with orbitolinids, fragments of oysters, intraclasts and peloids. Conglomerate matrix includes fragments of orbitolinids and *Alveolina*.	Barremian-Aptian, Cenomanian? Senonian? Ypresian and late Ypresian-Lutetian?
		01b	Conglomerate clasts are mainly grainstones with *Alveolina*, *Opertorbitolites*, other foraminifera and recrystallized green algae. Clasts made up of a grainstone texture with ooids, peloids and fragments of molluscs, a packstone texture with peloids, orbitolinids, and fragments of rudist bivalves, other molluscs, and echinoids, a wackestone texture with small miliolids and other foraminifera, and a wackestone texture with ostracods, also occur. Fragments of orbitolinids were recognized within the conglomerate matrix.	Barremian-Aptian, Senonian? Ypresian and late Ypresian-Lutetian?
02	Montblanc Fm. (Cabra del Camp Mb.)	02a	Conglomerate clast made up of dolomitic limestone with a grainstone texture containing peloids, miliolids, other foraminifera, and fragments of molluscs, echinoids, and calcareous algae.	Barremian-Aptian
		02b	Conglomerate limestone clast exhibiting a highly recrystallized texture with abundant calcareous green algae. Skeletal components such as foraminifera, and fragments of oysters, gastropods, other molluscs, echinoids, and bryozoans occur. Non skeletal components include peloids, silt-sized quartz grains and intraclasts. Intraclasts are made up of packstone to grainstone textures with scarce ooids, other coated grains, peloids and silt-sized quartz.	Cretaceous?
		02c	Conglomerate clast with a packstone to grainstone texture including miliolids, *Alveolina*, *Opertorbitolites*, small rotaliids, other foraminifera, and fragments of echinoids and molluscs.	Ypresian

TABLE I. Continued

Sampling site	Sampled formation	Sample ID	Clast/matrix description	Clast/matrix components attributed age/s
03	Montblanc Fm. (Cabra del Camp Mb.)	03a	Conglomerate grainstone clast with orbitolinids, encrusting and agglutinating foraminifera, other foraminifera, fragments of oysters, other molluscs, calcareous algae and serpulids. Non-skeletal components identified include peloids, intraclasts and silt-sized quartz.	Barremian-Aptian
		03b	Recrystallized packstone clast with peloids, silt-sized quartz, miliolids, other foraminifers, and fragments of oysters, other molluscs, bryozoans, echinoids, and calcareous algae.	Barremian-Aptian?
		03c	Conglomerate clasts are made up of wackestone textures with small foraminifera, mudstone to wackestone textures, occasionally bioturbated, with ostracods and gastropods, packstone to grainstone textures with orbitolinids, peloids, and fragments of oysters, other molluscs, echinoids, corals, and calcareous algae, and grainstone textures with miliolids, *Alveolina* and other foraminifera. A clast made up of "bacinellid" fabrics was also identified.	Barremian-Aptian, Senonian? Ypresian and late Ypresian-Bartonian?
04	Montblanc Fm. (Cabra del Camp Mb.)	04a	Conglomerate clasts exhibit grainstone textures with abundant orbitolinids, miliolids, other foraminifera, and fragments of *Marinella lugeoni*, *Permocalculus*, other calcareous algae, bryozoans, echinoids, oysters, other bivalves, corals, and sections of belemnite rostra. Non-skeletal components include well-rounded intraclasts, peloids and silt-sized quartz grains.	Barremian-Aptian
		04b	Calclithite with silt to sand-sized quartz grains, peloids, ooids, miliolids, other undetermined benthic foraminifera and fragments of orbitolinids. Small dolostone and mudstone clasts. Small grainstone clasts with peloids and fragments of molluscs.	Barremian-Aptian
05	Vallespinosa Fm.	05	Breccia matrix with *Nummulites*, gypsinids, *Nummoloculina* and fragments of orbitolinids, serpulids and bivalves. Grainstone clast with *Alveolina*.	Barremian-Aptian, and Ypresian
06	Montblanc Fm. (Cabra del Camp Mb.?)	06	Breccia matrix with fragments of orbitolinids. Small packstone and grainstone clasts with orbitolinids.	Barremian-Aptian
07	Montblanc Fm. (Cabra del Camp Mb.?)	07	Conglomerate matrix with orbitolinids, *Alveolina*, *Solenomeris* and gypsinids.	Barremian-Aptian and Ypresian

TABLE I. Continued

Sampling site	Sampled formation	Sample ID	Clast/matrix description	Clast/matrix components attributed age/s
08	Vallespinosa Fm.	08	Conglomerate matrix with *Nummulites*, gypsinids, *Nummoloculina* and fragments of orbitolinids, serpulids and bivalves. Grainstone clasts with *Alveolina*.	Barremian-Aptian, and Ypresian
09	Montblanc Fm. (Cabra del Camp Mb.?)	09a	Conglomerate matrix with orbtiolinids, *Nummuloculina* and fragments of gypsinids.	Barremian-Aptian and Ypresian
		09b	Conglomerate matrix with orbitolinids and fragments of gypsinids. Grainstone clast with *Alveolina*.	Barremian-Aptian and Ypresian
10	Montblanc Fm. (Cabra del Camp Mb.?)	10	Sandstone with small orbitolinid fragments.	Barremian-Aptian
11	Montblanc Fm. (Cabra del Camp Mb.?)	11a	Conglomerate matrix with fragments of orbitolinids, miliolids, *Alveolina*, *Opertorbitolites* and geniculate Corallinales.	Barremian-Aptian and Ypresian
		11b	Conglomerate matrix with fragments of orbitolinids, miliolids and geniculate Corallinales.	Barremian-Aptian and Ypresian
12	Sant Miquel Fm.	12a	Conglomerate matrix with fragments of orbitolinids.	Barremian-Aptian
		12b	Conglomerate matrix with fragments of orbitolinids and *Alveolina*.	Barremian-Aptian and Ypresian
13	Sant Miquel Fm.	13	Conglomerate matrix contains orbitolinids. Packstone and grainstone clasts with orbitolinids. Grainstone clasts with *Alveolina*.	Barremian-Aptian and Ypresian
14	Montblanc Fm.	14	Grainstone clast with *Alveolina.*	Ypresian

APPENDIX II

Details about the sampling and laboratory procedures for the magnetostratigraphic analysis.

Sampling was focused on limestones, mudstones, and fine-grained sandstones, since coarser lithologies are less efficient recorders of the geomagnetic field. Electrical and gasoline power drills equipped with diamond core bits cooled with water were used to obtain 2 samples per site after cleaning the outcrop to get fresh unaltered rocks. Samples were in situ oriented with a magnetic compass coupled with an orienting device with clinometer in order to have a coordinate system to refer the paleomagnetic vector obtained in the laboratory. Laboratory treatment consisted in stepwise thermal demagnetization and subsequent measurement of the Natural Remanent Magnetization (NRM). Samples were heated in an MMTD-80 thermal demagnetizer (Magnetic Measurements Ltd.) with a residual field less than 10nT and the NRM was measured in a superconducting rock magnetometer (2G Enterprises) in the Paleomagnetic Laboratory of Barcelona (CCiTUB and GEO3BCN CSIC). The magnetic noise in the superconducting rock magnetometer is around $1x10^{-6}$A/m, well below the intensity of the samples (Figure II).

Stepwise thermal demagnetization was performed in 14 to 18 temperature steps, from 100ºC up to 520ºC in limestones and grey mudstones and up to 680-690ºC in red mudstones and fine-grained sandstones. Magnetic susceptibility was measured after each demagnetization step with a kappabridge KLY2 (Geofyzika Brno) to monitor the undesired formation of magnetic minerals upon heating, since it can be detected by a sharp increase in magnetic susceptibility (Table III). Stable Characteristic Remanent Magnetization (ChRM) directions were calculated by means of Principal Component Analysis (Kirschvink, 1980) after visual inspection of demagnetization diagrams using the Paldir software (University of Utrecht) (Figures II; III and Table II).

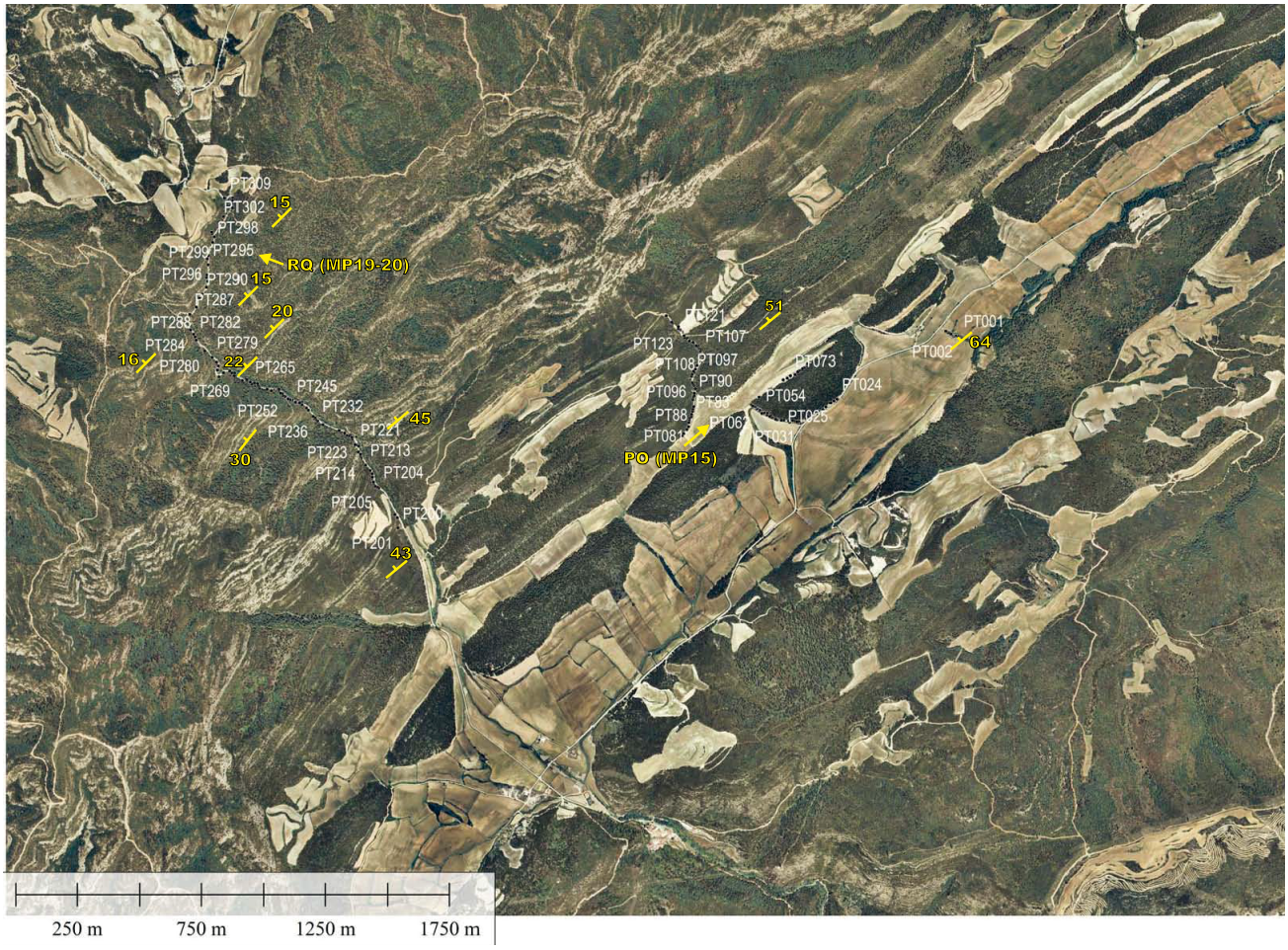

FIGURE I. Location of the magnetostratigraphic sites along the Pontils section. Bedding dips are indicated in yellow. PO and RQ represent the location by lithostratigraphic correlation of the Pontils and Rocafort de Queralt fossil sites, respectively.

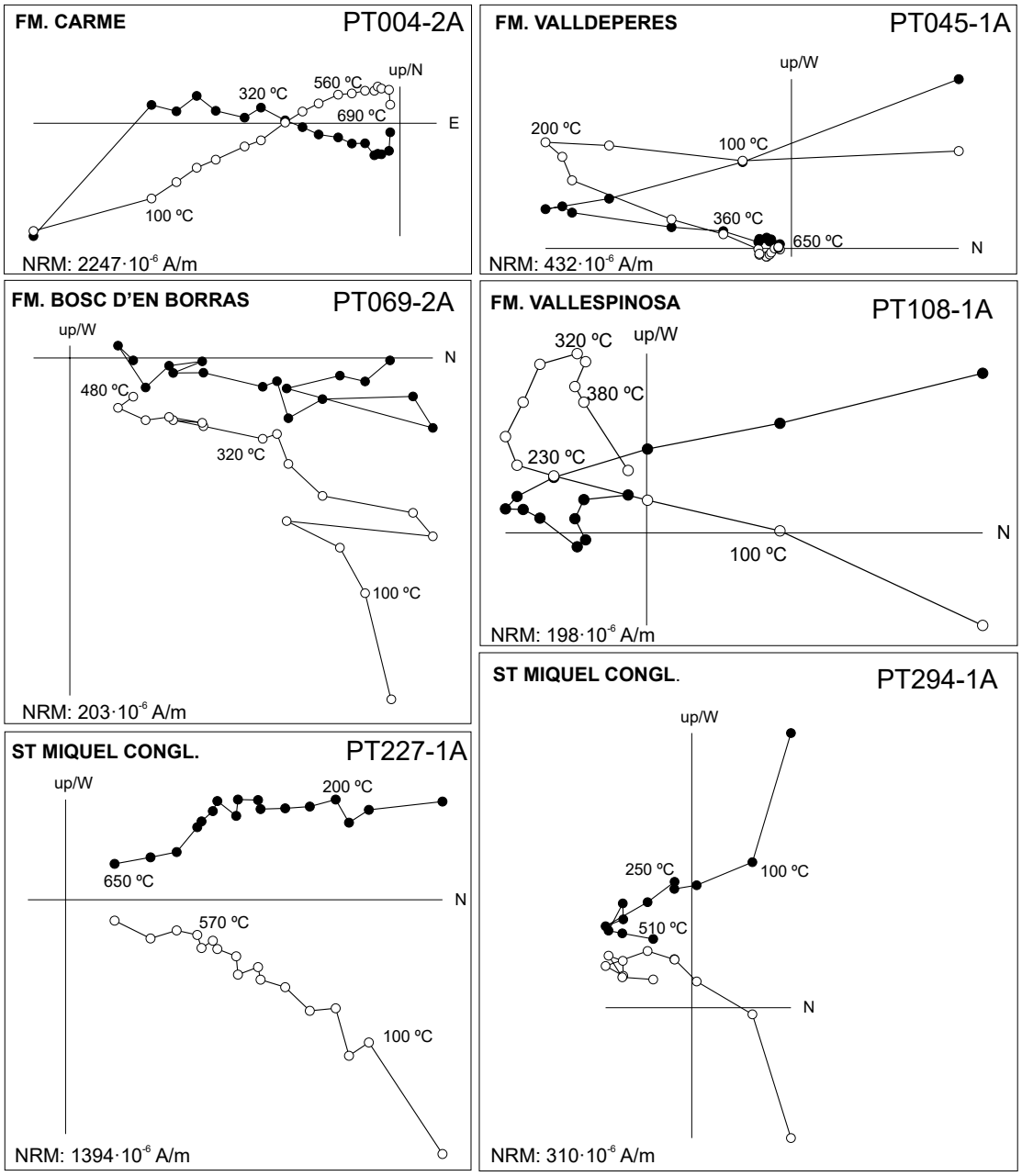

FIGURE II. Demagnetization diagrams of selected samples for the different formations. Black (white) dots represent projection of the demagnetization vector-end point into the horizontal (vertical) plane. Thermal demagnetization steps expressed in ºC. All diagrams represented after bedding correction. NRM: Natural Remanent Magnetization.

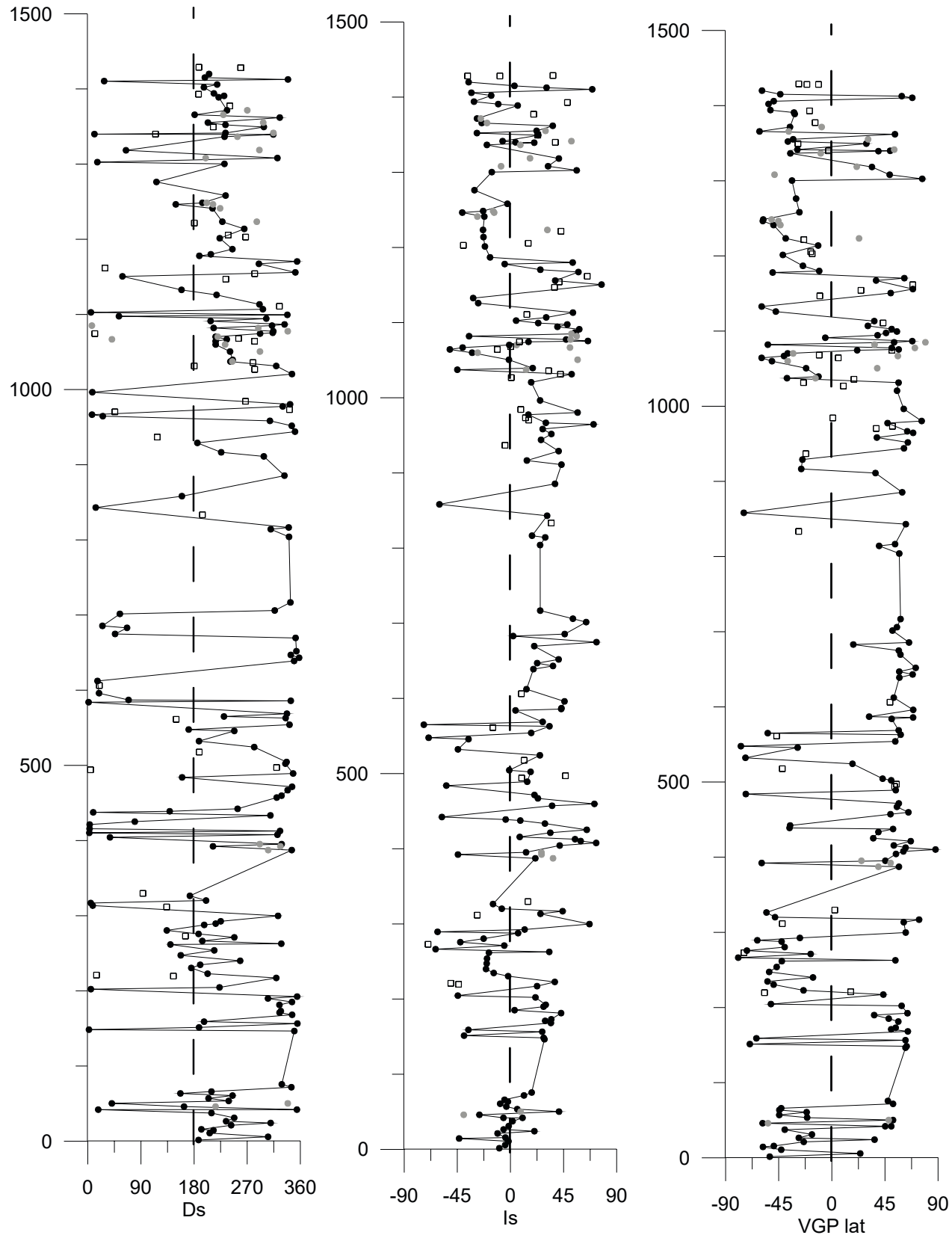

FIGURE III. Local magnetostratigraphy of the Pontils section. Ds: Declination in stratigraphic coordinates; Is: Inclination in stratigraphic coordinates; VGP lat: Virtual Geomagnetic Pole latitude.

TABLE II. Paleomagnetic information of the characteristic components calculated for each sample of the Pontils magnetostratigraphic section. Dec_g: magnetic declination in geographic coordinates; Inc_g: Inclination in geographic coordinates; Dec_s: Declination in stratigraphic coordinates; Inc_s: Inclination in stratigraphic coordinates; VGP lat: Virtual Geomagnetic Pole latitude; int: intensity expressed in 10^{-6}A/m; err: maximum angular deviation; Q: Quality; Trange: selected temperature intervals to calculate each characteristic component

sample	31T UTM x	31T UTM y	level (m)	Dec_g	Inc_g	Dec_s	Inc_s	VGP lat	int	err	Q	Trange
PT001-2A	363412.631	4591653.971	1.50	218.47	-41.51	187.58	-9.38	-52.6	386.57	19.14	2	* 150-520
PT002-1A	363408.42	4591652.2	5.75	293.16	56.66	305.29	-4.41	24	648.28	3.22	1	280-650
PT003-1A	363405.672	4591654.103	10.75	220.50	-21.30	206.45	-1.70	-42.9	66.90	23.24	2	680-690
PT004-2A	363400.139	4591656.059	14.50	266.59	-29.13	212.90	-43.47	-58.4	294.44	5.61	1	590-680
PT005-2A	363398.712	4591654.234	15.80	215.47	-34.99	192.28	-4.25	-49.1	258.67	3.27	1	590-650
PT006-1A	363391.717	4591652.516	21.25	245.16	7.00	242.81	-10.89	-23.8	77.24	5.01	2	650-680
PT007-1A	363391.452	4591623.106	24.25	260.18	79.37	309.68	20.24	36.2	381.39	3.99	1	360-620
PT008-2A	363389.527	4591652.874	26.50	236.83	1.83	234.33	-5.87	-28	35.44	21.05	2	650-680
PT010-1A	363384.828	4591656.348	31.00	239.12	15.84	247.86	-1.50	-16.9	38.28	18.94	2	480-590
PT013-1A	363379.365	4591662.005	37.50	218.65	-17.06	209.40	1.82	-39.9	105.08	7.72	2	590-680
PT014-1A	363378.987	4591664.608	42.00	44.74	33.03	17.52	10.23	50.4	1083.44	2.69	1	280-650
PT014-2A	363378.987	4591664.608	42.00	10.98	43.45	354.28	-5.97	45.2	772.07	4.59	1	350-680
PT015-1A	363372.511	4591667.688	46.00	235.40	-68.92	162.91	-26.28	-58.63	140.92	7.93	2	400-570
PT016-2A	363369.727	4591667.741	50.25	85.39	23.00	40.69	41.11	51.8	73.69	7.94	2	620-680
PT017-1A	363364.229	4591671.547	53.50	228.19	10.80	238.61	5.78	-20.9	247.88	7.54	2	650-680
PT018-1A	363361.48	4591673.45	57.00	221.20	-23.94	204.41	-3.48	-44.6	100.78	13.85	2	560-680
PT019-1A	---	---	60.75	244.41	10.12	245.24	-8.76	-21.3	56.88	9.20	2	480-520
PT020-1A	---	---	63.50	177.31	-60.87	156.82	-2.16	-44.5	70.47	7.10	2	520-620
PT021-1A	---	---	66.00	225.17	-20.09	209.50	-5.07	-42.9	31.40	25.61	2	680-690
PT022-1A	---	---	71.75	22.98	61.87	344.91	11.42	51.8	595.21	3.32	1	280-620
PT023-2A	---	---	75.75	8.05	78.27	328.64	17.97	47.5	850.76	3.80	1	320-620
PT024-1A	362920.435	4591398.595	146.55	4.96	54.06	349.77	28.79	62.4	767.59	3.33	1	320-620
PT025-2A	362907.767	4591391.43	148.45	20.06	48.79	1.99	28.07	63.4	145.24	4.89	1	320-520
PT026-1A	362895.098	4591384.267	151.35	217.34	-55.35	188.34	-39.33	-69.5	918.39	1.68	1	240-590
PT027-1A	362878.078	4591367.931	156.50	10.67	50.51	354.99	26.91	62.4	339.60	4.91	1	240-560
PT029-1A	362848.495	4591349.981	158.95	222.29	-48.29	196.83	-35.62	-63.9	3963.59	2.14	1	200-650
PT030-2A	362804.922	4591328.596	168.25	3.41	60.38	346.03	34.30	64.4	882.52	2.75	1	320-680
PT031-1A	362772.519	4591308.85	171.00	325.85	59.39	324.83	29.41	50.3	928.69	3.59	1	320-650
PT032-1A	362766.951	4591308.956	173.00	330.14	64.50	326.92	34.60	54	606.92	2.31	1	240-680
PT034-1A	362748.89	4591311.15	181.25	326.20	72.89	324.52	42.90	56.3	189.49	4.25	1	280-590
PT035-2A	362743.358	4591313.107	185.25	349.72	30.97	345.79	3.52	48.2	245.06	7.63	2	480-620
PT036-1A	362730.689	4591305.943	189.85	294.04	55.68	305.15	28.00	35.9	118.71	10.65	2	280-520
PT037-1A	362728.01	4591311.547	192.45	12.23	53.40	354.59	29.94	64.1	1117.09	3.65	1	* 320-680
PT038-1A	362707.166	4591313.795	202.25	19.03	41.39	5.01	21.15	59.1	323.98	3.52	1	320-680
PT039-1A	362697.422	4591313.98	204.50	252.27	-42.19	223.03	-44.54	-51.6	211.68	6.85	2	440-620
PT041-2A	362680.753	4591316.148	217.15	329.61	61.23	319.26	22.52	43.6	30.58	8.22	2	260-380
PT043-1A	362673.828	4591318.13	222.75	182.47	19.28	202.90	37.52	-24	82.97	1.51	2	200-300
PT044-1A	362661.406	4591323.92	230.50	183.93	-28.31	175.25	-2.00	-49.3	102.34	4.97	1	400-590
PT045-1A	362657.265	4591325.85	234.75	205.85	-29.37	190.30	-14.15	-54.5	391.16	7.58	2	280-590
PT046-1A	362654.622	4591333.305	240.00	262.10	5.98	258.01	-20.71	-16	46.63	13.04	2	* 320-480
PT048-1A	362650.376	4591329.683	247.25	176.18	-52.77	157.40	-20.09	-53.1	21.80	15.97	2	620-680
PT050-2A	362639.487	4591342.848	253.95	228.66	-18.42	214.14	-19.88	-46.7	54.49	8.54	2	520-650
PT052-1A	362626.959	4591343.087	261.75	148.20	-57.11	140.02	-18.23	-42.4	34.45	15.07	2	520-650
PT053-2A	362618.572	4591341.395	262.75	354.90	68.12	327.85	32.89	53.8	840.89	2.80	1	280-650
PT054-2A	362614.642	4591354.427	266.35	278.78	-62.50	193.98	-63.41	-79.3	47.86	4.88	2	520-540
PT055-1A	362610.466	4591354.507	271.25	248.60	3.60	248.06	-5.21	-18	30.19	4.81	2	260-300
PT057-1A	362609.074	4591354.533	275.75	233.75	-60.32	187.58	-42.52	-72	58.35	7.60	2	280-420
PT059-1A	362600.828	4591360.244	280.35	123.88	-59.35	133.71	-22.70	-40	47.51	2.39	1	300-380
PT061-1B	362592.581	4591365.954	287.75	199.95	-16.87	197.08	6.49	-42.6	6.82	18.56	2	340-380
PT062-2A	362591.189	4591365.98	289.50	278.59	-52.01	216.54	-61.69	-63.1	25.00	2.95	2	280-300
PT063-1A	362587.084	4591369.76	292.55	219.96	3.27	225.13	12.04	-27.1	10.82	3.73	2	300-340
PT065-2A	362576.054	4591375.523	299.75	150.36	74.99	322.13	66.92	62.6	18.53	6.23	2	280-320
PT069-2A	362773.639	4591514.3	313.45	32.76	48.15	8.37	25.39	60.9	165.46	4.76	1	260-440
PT071-1A	362763.79	4591508.934	316.95	54.50	62.92	4.82	44.20	73.9	38.12	8.04	2	230-380
PT072-2A	362752.443	4591498.043	320.20	210.73	-26.88	200.20	-7.30	-48.1	40.83	8.02	2	400-420
PT074-1A	362721.539	4591483.821	326.45	186.13	-46.76	172.93	-14.74	-55.4	384.20	2.07	1	400-480
PT077-1A	362303.716	4591260.391	387.25	359.93	50.78	345.52	21.03	56.8	220.91	7.08	2	200-480
PT078-1A	362316.562	4591276.806	392.25	247.79	-44.10	212.01	-44.43	-59.5	232.56	5.65	1	230-460
PT079-2A	362323.733	4591287.776	395.25	332.43	47.68	328.37	13.26	45.3	489.02	4.51	1	280-650
PT081-2A	362326.976	4591311.779	404.25	68.68	39.26	37.54	41.69	54.3	51.10	8.20	2	360-480
PT082-2A	362329.972	4591322.828	407.75	137.64	72.37	321.19	72.61	60.6	153.83	6.64	2	400-650
PT083-2A	362335.645	4591328.273	410.15	78.23	66.71	2.46	59.51	87.8	210.84	6.33	2	340-540
PT084-2A	362335.822	4591337.525	412.75	47.02	86.44	325.56	54.70	62.5	119.40	8.83	2	260-440
PT085-2A	362340.245	4591350.399	415.75	12.61	31.61	2.91	7.86	52.4	99.16	8.13	2	260-320
PT086-2A	362341.813	4591359.624	421.25	32.59	53.09	3.13	33.73	66.8	694.63	3.54	1	260-480
PT087-2A	362344.773	4591368.823	425.25	111.35	38.09	79.56	64.66	35.1	53.10	6.12	2	300-360
PT088-1B	362341.127	4591396.659	433.50	299.50	63.20	309.27	29.21	39.4	141.33	5.66	1	200-340
PT089-1B	362344.123	4591407.708	437.50	19.16	29.04	9.17	8.34	51.8	108.85	1.58	2	260-300

TABLE II. Continued

sample	31T UTM x	31T UTM y	level (m)	Dec_g	Inc_g	Dec_s	Inc_s	VGP lat	int	err	Q	Trange
PT090-1A	362347.012	4591413.206	439.00	138.42	-39.04	138.64	-4.04	-35.8	84.84	13.14	2	* 380-460
PT091-1A	362347.189	4591422.459	442.25	283.53	-34.76	253.79	-58.09	-35.3	78.06	8.82	2	* 340-380
PT092-1A	362351.717	4591440.883	457.25	320.98	70.27	320.05	35.28	49.7	42.97	1.91	2	320-360
PT093-1A	362346.396	4591453.942	459.75	129.54	73.41	328.11	71.15	64.9	81.63	4.20	1	280-340
PT094-1A	362342.326	4591459.573	467.00	355.53	59.42	338.46	23.29	55.1	110.86	5.47	1	260-420
PT095-1A	362339.648	4591465.178	471.50	4.49	53.62	346.01	20.34	56.7	133.39	6.57	2	280-320
PT096-1A	362335.966	4591491.163	484.00	282.53	-70.19	159.82	-54.34	-72.9	53.84	16.02	2	* 300-360
PT097-2A	362338.891	4591498.512	489.25	11.52	54.19	347.86	14.24	54.1	184.83	4.17	1	260-380
PT100-2A	362351.842	4591520.478	502.25	353.83	63.51	334.69	17.07	50.3	328.52	5.77	1	320-590
PT101-2B	362349.305	4591533.484	504.50	344.73	46.09	336.67	-0.98	43	396.82	5.66	1	280-620
PT105-1A	362381.035	4591568.417	524.35	243.63	55.35	281.97	24.94	17.5	65.03	16.12	2	320-360
PT106-1A	362382.131	4591575.433	532.25	254.30	-53.59	188.39	-44.48	-73.2	95.73	5.81	2	340-380
PT107-1B	362372.741	4591594.124	545.85	268.04	-9.36	248.13	-35.53	-29	49.53	3.67	2	300-340
PT108-1A	362372.882	4591601.525	547.75	300.44	-55.38	170.88	-69.30	-77	99.62	1.25	2	320-340
PT109-1B	362365.957	4591603.508	554.05	7.99	61.08	341.76	17.59	53.7	94.40	2.35	1	260-340
PT111-1A	362363.385	4591614.664	563.05	29.06	76.07	335.03	33.08	58.3	35.91	8.09	2	260-360
PT112-1A	362359.139	4591611.043	564.95	298.41	-36.71	230.68	-73.30	-54.3	24.73	12.74	2	340-360
PT113-2A	362355.034	4591614.823	568.75	16.71	71.12	337.26	27.37	56.6	20.25	8.67	2	200-280
PT114-1A	362345.466	4591624.26	584.00	13.07	43.80	1.29	4.33	50.7	419.93	2.60	1	230-340
PT115-1A	362344.145	4591627.989	586.00	59.68	83.06	343.89	43.03	68.8	74.31	4.01	1	300-360
PT116-1B	362342.753	4591628.015	586.95	100.70	25.62	69.10	43.19	31.6	246.40	2.66	1	280-340
PT117-1A	362327.548	4591633.858	596.05	83.56	58.78	18.97	45.76	68.9	50.85	8.40	2	230-320
PT119-2A	362308.307	4591647.182	612.25	37.38	43.05	16.45	13.62	52.4	25.27	7.84	2	230-280
PT121-1A	362289.421	4591679.012	639.05	6.39	62.38	349.50	19.43	57.2	86.45	7.00	2	200-300
PT122-2A	362285.28	4591680.941	643.25	48.47	70.44	357.86	36.05	68.4	185.91	1.84	2	200-260
PT123-1A	362282.567	4591684.696	646.95	357.55	67.28	343.87	22.66	57.1	245.96	3.48	1	260-340
PT124-1A	362282.709	4591692.097	651.95	58.14	75.67	353.37	40.82	71	192.52	4.19	1	260-400
PT125-2A	362257.901	4591705.528	669.50	11.60	62.09	351.95	20.22	58.1	302.70	5.09	1	260-320
PT126-1A	362255.187	4591709.282	674.85	130.32	46.90	46.14	72.93	56.7	584.49	1.82	1	340-480
PT200-1A	361150.376	4590880.788	683.00	65.84	-3.98	66.43	2.34	18.2	129.05	2.26	1	260-320
PT201-1A	361150.412	4590882.639	685.65	73.99	52.37	24.71	45.95	65.3	153.25	3.43	1	260-400
PT127-1A	362233.412	4591735.613	701.50	118.62	42.88	54.27	64.20	51.3	15.61	11.19	2	230-280
PT202-2A	361148.411	4590923.402	706.15	209.45	82.74	316.73	52.94	55.1	68.28	3.83	1	200-280
PT203-2A	361137.523	4590936.568	716.90	359.48	62.39	343.19	25.24	58.2	57.76	20.25	2	230-280
PT204-1A	361072.733	4591043.328	804.10	10.69	64.97	340.79	25.11	57.1	382.24	5.88	1	240-560
PT206-1C	361058.955	4591050.998	814.20	287.17	74.50	309.98	29.47	40	68.05	13.69	2	240-360
PT207-2B	361058.955	4591050.998	816.55	1.32	59.68	340.21	18.30	53.5	123.02	8.82	2	400-620
PT210-1A	361047.068	4591084.546	843.10	47.11	46.06	13.47	31.10	62.7	378.95	3.12	1	320-590
PT212-1A	361037.822	4591110.639	858.20	283.15	-73.26	159.39	-60.12	-74.5	63.03	22.01	2	* 340-420
PT213-1A	361018.761	4591133.219	885.50	11.98	76.27	333.19	37.74	59.6	102.33	11.16	2	590-650
PT215-1A	361001.27	4591165.026	911.1	235.80	74.56	298.12	43.21	36.96	136.37	7.15	2	300-480
PT216-1A	360998.593	4591170.631	916.6	217.32	7.74	225.87	13.88	-25.87	189.50	12.15	2	* 350-570
PT218-1A	360991.953	4591187.418	929.05	172.62	5.26	185.54	40.83	-24.9	54.34	9.44	2	360-480
PT220-1A	360990.989	4591209.65	944.1	23.03	58.31	350.95	25.89	61.05	259.05	5.13	1	200-420
PT221-1B	360979.959	4591215.416	951.9	4.87	59.58	345.44	34.70	64.4	199.45	7.10	2	200-450
PT222-2A	360969.251	4591237.835	958.4	301.81	56.51	308.58	27.34	38.17	370.84	4.68	1	200-480
PT223-2A	360969.393	4591245.236	964.65	98.46	62.15	25.38	70.42	68.78	216.74	3.34	1	250-600
PT224-2A	360966.609	4591245.29	966.65	27.69	46.42	7.08	29.99	63.87	272.14	4.20	1	200-540
PT227-1A	360945.872	4591253.094	977.65	334.09	44.56	330.19	15.25	47.17	562.19	3.69	1	480-630
PT228-1A	360937.627	4591258.806	980.4	45.41	77.51	342.68	56.93	76.09	170.98	7.29	2	420-570
PT230-1A	360915.604	4591272.188	996.50	24.88	41.93	7.77	25.11	60.9	32.53	8.38	2	300-380
PT231-2A	360849.215	4591295.681	1020.6	350.77	35.15	345.92	17.59	55.21	93.17	13.27	2	* 350-570
PT233-2A	360820.376	4591316.599	1031.40	329.70	65.46	319.20	51.80	56.5	122.00	7.15	2	250-490
PT235-2A	360817.735	4591324.054	1037.30	251.81	-35.85	241.58	-45.00	-37.97	70.42	11.81	2	450-530
PT236-2A	360809.49	4591329.767	1039.60	239.95	27.19	245.32	18.93	-11.32	85.33	19.29	2	350-530
PT237-1C	360790.465	4591354.197	1050.60	240.32	6.54	240.91	-1.26	-21.8	169.14	2.92	2	570-600
PT238-1A	360782.291	4591363.611	1059.90	226.72	-24.74	216.52	-32.40	-50.72	93.90	8.11	2	250-350
PT239-1A	360764.446	4591376.912	1064.4	235.73	-42.07	216.52	-51.26	-59.46	296.93	5.75	1	300-650
PT240-1B	360763.268	4591388.041	1066.90	245.71	-27.14	235.52	-40.45	-40.53	129.74	3.99	2	300-350
PT242-2A	360754.844	4591384.502	1070.3	215.90	4.82	216.54	-1.02	-37.42	306.01	1.90	1	510-600
PT243-1B	360739.533	4591384.797	1074.50	292.24	35.31	291.80	15.33	21.44	77.53	6.77	2	200-350
PT244-1A	360738.176	4591386.675	1075.65	4.94	80.10	313.21	65.64	56.66	304.56	6.65	2	250-570
PT245-2A	360724.363	4591392.495	1077.65	330.45	64.15	314.30	47.16	50.8	332.05	10.71	2	200-510
PT246-1A	360724.435	4591396.195	1081.9	224.87	-28.24	213.12	-35.04	-54.21	242.64	5.84	1	200-510
PT247-1A	360717.475	4591396.329	1085.10	335.53	72.26	312.14	55.37	52.7	151.25	8.66	2	240-480
PT248-2A	360716.083	4591396.356	1086.65	3.36	65.21	333.26	54.44	68.1	200.74	7.54	2	200-510
PT249-2A	360707.802	4591400.218	1091.15	176.78	55.76	208.09	58.31	-5.53	113.41	6.16	2	420-600

TABLE II. Continued

sample	31T UTM x	31T UTM y	level (m)	Dec_g	Inc_g	Dec_s	Inc_s	VGP lat	int	err	Q	Trange
PT250-1B	360698.237	4591409.659	1094.4	309.11	59.06	302.45	39.83	38.75	205.94	5.35	1	390-480
PT251-1A	360695.453	4591409.713	1097.65	66.56	35.04	52.85	48.15	45.9	71.62	6.13	2	520-560
PT252-1A	360687.172	4591413.574	1099.40	347.32	35.67	338.09	23.60	55.1	363.27	5.83	1	360-680
PT253-2A	360684.531	4591421.03	1102.65	8.80	10.45	5.34	4.80	50.61	468.34	2.90	1	300-510
PT254-1A	360677.608	4591423.014	1107.00	300.59	55.99	296.62	30.30	30.5	124.94	6.57	2	360-480
PT256-1A	360670.968	4591439.802	1113.40	294.01	78.90	290.87	52.92	36	253.01	7.16	1	400-680
PT257-1A	360640.203	4591432.992	1125.90	227.87	-16.69	218.07	-27.27	-47.4	131.62	5.72	2	280-360
PT258-1A	360622.214	4591438.893	1132.70	176.80	-45.51	158.79	-31.54	-59.5	95.91	21.70	2	620-680
PT260-1A	360589.021	4591450.64	1150.7	101.02	52.22	58.67	77.20	49.85	126.46	7.53	2	390-480
PT262-1A	360583.667	4591461.85	1155.90	11.01	53.78	351.69	37.98	68.6	349.66	6.53	2	240-520
PT264-2A	360559.968	4591460.456	1167.4	267.72	81.72	289.76	57.56	37.49	161.28	8.44	2	250-450
PT265-1A	360554.543	4591467.966	1170.4	8.32	36.48	354.61	25.32	61.42	210.02	13.18	2	* 200-600
PT266-1A	360540.802	4591477.487	1177.90	193.05	-17.17	188.96	-4.88	-50.1	869.28	2.92	1	320-520
PT267-1A	360536.698	4591481.268	1179.90	184.20	42.23	208.45	52.76	-10.7	148.03	6.66	2	320-400
PT268-1A	360522.635	4591474.136	1186.9	248.41	-4.45	244.92	-17.26	-24.55	87.71	8.36	2	420-570
PT269-2A	360496.545	4591493.15	1201.4	230.70	-15.64	223.45	-21.67	-41.48	28.38	19.96	2	* 480-540
PT273-1A	360474.632	4591512.085	1213.9	272.53	-10.18	264.94	-22.83	-11.6	93.69	6.51	2	420-480
PT275-1A	360431.015	4591488.863	1223.40	241.20	-27.14	227.87	-23.21	-39.06	68.27	9.47	2	490-600
PT276-1A	360424.592	4591516.754	1241.15	225.16	-33.84	211.29	-22.09	-49.38	57.33	2.48	1	450-530
PT277-1A	360429.09	4591533.327	1246.4	159.06	-59.08	149.03	-40.80	-58.45	220.74	8.79	2	390-540
PT278-1A	360421.025	4591548.293	1248.5	203.57	-30.22	194.06	-23.10	-58.08	139.02	11.74	2	350-540
PT279-1A	360403.287	4591567.146	1258.2	233.46	2.34	233.42	-2.56	-27.46	126.65	11.14	2	510-570
PT280-1A	360373.165	4591593.645	1276.20	111.69	-49.76	116.23	-30.46	-30.29	1913.71	2.30	1	250-530
PT281-2A	360337.798	4591636.904	1300.30	236.07	-10.74	231.46	-15.75	-33.69	79.04	6.73	2	530-570
PT282-2A	360333.872	4591649.939	1302.60	47.96	58.80	16.15	56.11	76.59	151.14	9.45	2	400-490
PT283-1A	360327.128	4591661.176	1308.1	325.53	51.35	321.19	31.91	48.96	251.56	11.70	2	200-420
PT284-1A	360314.923	4591678.072	1318.40	74.48	31.96	64.61	41.01	33.97	94.33	10.13	2	300-450
PT285-3A	360266.849	4591712.322	1336.5	236.40	-14.75	231.64	-19.89	-35.12	147.88	9.69	2	200-480
PT286-1A	360264.245	4591721.628	1339.4	315.80	35.92	314.36	20.14	39.39	106.87	6.11	2	350-450
PT287-1A	360311.964	4591741.066	1339.90	11.18	4.31	11.18	4.31	49.39	187.84	10.88	2	200-400
PT288-2A	360338.983	4591770.162	1341.4	234.27	-1.58	233.18	-6.64	-29.12	146.92	6.72	2	250-510
PT289-2A	360350.834	4591806.955	1349.4	294.78	37.38	298.23	23.54	29.16	127.61	9.22	2	200-350
PT290-1A	360362.292	4591823.393	1352.3	241.03	-26.36	233.28	-28.40	-37.25	61.54	14.50	2	480-570
PT291-1A	360379.531	4591850.826	1355.15	198.93	15.05	203.41	22.18	-32.76	110.09	10.46	2	480-630
PT293-1A	360380.283	4591889.685	1361.9	326.85	50.72	325.21	35.82	53.47	162.24	7.31	1	350-480
PT294-2A	360381.89	4591900.761	1365.65	187.15	-35.01	181.10	-24.31	-61.21	76.49	7.39	2	300-400
PT295-3A	360386.853	4591941.39	1371.65	243.30	-25.63	235.74	-28.29	-35.4	26.79	10.94	2	570-600
PT298-2A	360405.309	4592031.738	1388.9	220.40	3.98	221.73	6.17	-31.49	68.47	9.42	2	350-480
PT299-1A	360411.305	4592053.835	1390.7	233.57	-9.55	230.93	-10.30	-32.01	72.47	9.41	2	480-600
PT301-1A	360401.92	4592072.527	1394.1	222.86	-36.33	213.51	-30.86	-52	72.04	3.07	2	510-540
PT302-2A	360430.58	4592114.55	1402.1	201.18	-26.02	196.74	-16.25	-53.64	100.73	2.89	2	450-480
PT303-2A	360449.104	4592136.405	1405.9	229.36	-36.98	219.15	-33.02	-49.22	79.39	13.37	2	450-510
PT304-2A	360485.971	4592170.863	1410.4	71.22	72.06	27.83	69.27	68.13	123.65	8.86	2	250-390
PT305-1A	360486.042	4592174.564	1412.65	341.29	45.37	339.08	30.63	59.19	85.70	9.89	2	350-450
PT306-1A	360483.509	4592187.57	1415.15	198.65	-6.48	198.34	3.38	-43.71	122.01	7.62	2	390-510
PT307-2A	360486.543	4592200.47	1419.9	216.32	-42.68	205.54	-35.47	-59.2	29.01	11.67	2	390-420
PT015-2A	363372.511	4591667.688	46.00	262.87	-25.79	216.41	-39.57	-54.1	340.21	3.83	2b	280-560
PT016-1A	363369.727	4591667.741	50.25	9.33	64.63	338.76	8.52	48.21	804.11	4.52	2b	250-570
PT077-2A	362303.716	4591260.391	387.25	286.83	68.83	305.48	36.10	39.45	221.50	4.02	2b	200-350
PT078-2A	362316.562	4591276.806	392.25	331.98	60.90	326.19	26.32	49.75	65.65	6.72	2b	200-300
PT079-1A	362323.733	4591287.776	395.25	272.45	54.68	291.30	26.23	25.01	194.23	8.16	2b	250-590
PT235-1A	360817.735	4591324.054	1037.30	240.74	21.65	244.72	13.37	-13.9	127.94	9.86	2b	320-440
PT237-1B	360790.465	4591354.197	1050.60	285.79	71.63	291.60	56.87	38.4	162.07	8.09	2b	320-440
PT238-2A	360782.291	4591363.611	1059.90	239.15	-15.75	232.66	-27.74	-37.4	115.44	16.17	2b	* 280-440
PT240-1A	360763.268	4591388.041	1066.9	58.57	40.19	40.85	50.48	55.89	84.47	21.17	2b	350-450
PT242-1B	360754.844	4591384.502	1070.30	217.29	11.98	220.18	5.29	-32.75	243.42	5.41	2b	300-490
PT245-1A	360724.363	4591392.495	1077.65	5.20	60.48	338.68	50.93	70.31	158.50	7.01	2b	300-400
PT246-1B	360724.435	4591396.195	1081.90	288.02	76.15	288.81	56.16	36.13	259.77	5.74	2b	250-490
PT247-2A	360717.475	4591396.329	1085.10	32.63	51.51	6.95	51.65	79.25	79.92	3.65	2b	300-450
PT275-2A	360431.015	4591488.863	1223.4	266.69	47.38	286.18	31.26	23.09	125.45	10.20	2b	350-480
PT276-2A	360424.592	4591516.754	1241.15	240.72	-32.97	224.11	-27.96	-43.61	93.71	18.34	2b	480-570
PT277-2A	360429.09	4591533.327	1246.40	217.35	-15.44	212.10	-13.79	-45.27	96.86	10.15	2b	350-400
PT278-2A	360421.025	4591548.293	1248.50	207.58	-19.86	201.51	-14.67	-50.98	56.94	5.32	2b	400-450
PT283-2A	360327.128	4591661.176	1308.10	203.53	-14.11	199.78	-7.96	-48.53	87.82	4.65	2b	350-400
PT284-2A	360314.923	4591678.072	1318.7	288.69	31.99	290.66	16.58	21.03	126.02	9.76	2b	350-570
PT285-1A	360266.849	4591712.322	1336.50	250.56	17.91	253.56	8.31	-9.38	212.19	8.21	2b	200-490

TABLE II. Continued

sample	31T UTM x	31T UTM y	level (m)	Dec_g	Inc_g	Dec_s	Inc_s	VGP lat	int	err	Q	Trange
PT288-1A	360338.983	4591770.162	1341.40	320.06	67.37	314.43	51.69	52.88	114.98	6.79	2b	200-300
PT291-2A	360379.531	4591850.826	1355.15	292.55	43.42	297.20	29.75	30.74	181.31	6.26	2b	250-450
PT294-1A	360381.89	4591900.761	1365.65	235.01	-19.06	229.69	-19.84	-36.48	121.69	6.59	2b	350-510
PT295-1A	360386.853	4591941.39	1371.65	274.14	-14.90	270.10	-25.11	-8.62	327.76	7.00	2b	350-570
PT042-1A	362679.361	4591316.175	219.75	196.33	-77.23	144.92	-43.92	-57.1	32.24	17.47	3	* 150-280
PT056-1A	362609.109	4591356.384	272.95	305.26	-69.94	165.39	-69.79	-74.4	5.53	18.23	3	100-150
PT068-2A	362783.523	4591521.516	311.55	120.36	-64.61	133.52	-28.21	-42	13.12	4.92	3	200-230
PT075-2A	362704.695	4591476.738	329.75	94.73	-9.47	93.30	14.79	2.5	37.42	20.53	3	440-500
PT098-1A	362347.419	4591507.604	494.15	24.99	39.67	4.71	9.59	53.1	198.19	3.08	3	230-300
PT099-2A	362344.706	4591511.359	497.15	136.28	83.38	319.92	46.61	54.7	44.05	5.58	3	200-260
PT103-1A	362380.458	4591560.657	517.75	192.18	-21.05	188.75	11.63	-42	33.94	19.14	3	* 360-400
PT110-1A	362364.672	4591609.086	561.25	162.65	-64.25	149.62	-14.87	-46.7	21.02	29.01	3	* 320-420
PT118-1A	362316.624	4591645.173	606.25	36.68	37.82	19.52	9.30	49.3	52.89	3.31	3	230-260
PT209-2A	361050.923	4591067.812	833.40	179.85	4.05	194.08	34.56	-28.1	145.85	4.48	3	380-480
PT217-1A	360998.7	4591176.182	220.9	352.49	-16.84	14.67	-50.53	15.99	114.95	4.12	3	350-510
PT219-3A	360989.133	4591185.621	936.90	107.68	-45.43	117.67	-4.68	-22	69.34	7.36	3	240-280
PT225-1B	360958.435	4591254.704	970.40	54.26	15.19	45.82	15.53	37.5	563.65	2.27	3	520-540
PT226-2A	360954.188	4591251.082	973.4	348.27	39.93	341.71	12.71	51.34	97.73	8.10	3	300-420
PT229-2A	360937.698	4591262.507	984.5	259.17	25.75	267.12	8.78	0.77	202.54	5.92	3	250-420
PT232-2A	360827.228	4591310.913	1026.9	282.06	15.11	282.68	0.76	9.72	42.46	17.22	3	250-350
PT233-1A	360820.376	4591316.599	1031.4	170.45	33.94	180.29	42.40	-23.96	119.97	8.69	3	350-480
PT234-1B	360814.879	4591320.406	1036.00	274.97	46.32	279.62	32.40	18.65	82.15	7.33	3	350-450
PT239-1B	360764.446	4591376.912	1064.40	282.48	8.79	282.43	-11.07	5.51	118.78	2.46	3	300-350
PT241-2A	360757.664	4591386.299	1068.10	253.89	16.69	255.59	0.18	-10.68	42.54	9.36	3	* 200-350
PT243-1A	360739.533	4591384.797	1074.5	14.90	9.78	11.82	7.65	50.88	77.49	6.47	3	300-390
PT255-1A	360670.861	4591434.251	1110.9	332.09	34.28	324.65	13.89	43.44	64.90	12.69	3	200-300
PT259-1A	360591.662	4591443.184	1146.9	207.94	43.57	233.80	37.31	-10.22	246.62	2.77	3	450-540
PT261-2A	360584.916	4591454.421	1154.15	262.99	68.67	282.69	41.33	24.67	92.61	4.62	3	250-350
PT263-2A	360571.175	4591463.942	1161.65	76.31	59.86	29.18	65.08	68.5	59.01	6.38	3	360-400
PT270-1A	360492.369	4591493.231	1202.90	276.51	-21.18	267.37	-39.88	-16.7	42.23	8.68	3	* 440-520
PT271-2A	360493.976	4591504.306	1205.6	230.62	23.78	237.88	15.13	-17.81	91.80	12.02	3	* 420-570
PT274-2A	360449.433	4591505.167	1221.65	173.53	17.20	180.39	42.79	-23.66	43.23	16.30	3	510-600
PT287-2A	360311.964	4591741.066	1339.9	116.25	22.27	114.63	38.03	-2.83	83.49	5.10	3	390-540
PT289-1A	360350.834	4591806.955	1349.40	207.17	18.09	212.52	23.14	-28.63	38.71	9.38	3	300-350
PT296-2A	360383.142	4591965.526	1377.4	235.02	21.86	240.68	19.64	-14.17	44.32	4.94	3	350-390
PT300-2A	360403.204	4592066.949	1392.9	179.84	35.83	187.51	48.27898	-18.88	90.66	11.94	3	300-350
PT309-1B	360456.101	4592210.313	1428.15	260.40	-3.67	258.84	-8.88	-11.31	82.39	16.93	3	* 250-450
PT309-1B	360456.101	4592210.313	1428.15	270.10	-31.12	259.19	-36.22	-21.1	179.38	8.85	3	200-390
PT310-1A	360453.318	4592210.367	1428.9	183.01	23.96	188.16	36.10	-28	107.32	16.97	3	600-650
PT016-2A	363369.727	4591667.741	50.25	280.01	44.81	292.14	-10.59	12.7	130.91	6.28	4	* 320-590
PT075-2A	362704.695	4591476.738	329.75	95.93	-45.30	111.57	-16.18	-21.6	207.84	19.45	4	* 230-420
PT213-1A	361018.761	4591133.219	885.50	215.67	-32.69	197.22	-15.00	-52.8	152.99	26.93	4	* 440-590
PT225-1B	360958.435	4591254.704	970.40	98.88	-43.37	109.52	-18.57	-20.9	1805.33	5.35	4	* 420-500
PT011-2A	363383.471	4591658.226	34.50	177.83	75.83	308.46	36.69	41.9	515.23	2.54	5	240-360
PT012-1A	363380.757	4591661.979	36.00	238.25	53.45	281.73	15.65	14	457.21	4.72	5	150-280
PT282-1A	360333.872	4591649.939	1302.60	187.34	-6.20	183.72	-10.23	-53.5	43.75	29.03	5	300-390

TABLE III. Bulk magnetic susceptibility measured after each demagnetization step. Thermal demagnetization steps expressed in Celsius degrees, susceptibility values in 10^{-6}SI

Sample	ini	100	150	200	240	280	320	360	400	440	480	520	560	590	620	650	680	690	
PT01-2A	119	117	116	118	117	116	118	114	114	115	112	112	102	93	88	88	92		
PT02-1A	95	92	91	91	90	91	90	87	85	88	93	96	86	81	81	84	87		
PT03-1A	154	149	147	150	149	148	148	142	149	171	187	205	155	141	138	136	140	144	
PT04-2A	152	150	149	150	151	150	149	142	153	172	187	204	155	142	139	139	145	161	
PT05-2A	138	137	136	138	138	137	138	130	142	158	174	193	136	125	120	117	115	119	
PT06-1A	97	97	96	96	96	96	95	91	94	99	100	106	83	79	74	73	73	83	
PT07-1A	141	134	133	135	133	131	131	119	117	124	123	127	100	97	96	95	99	101	
PT08-2A	78	77	76	77	78	77	76	73	76	80	80	81	61	57	55	53	53	56	
PT10-2A	93	92	91	91	91	91	90	85	87	89	88	87	73	71	69	70	74		
PT11-2A	148	138	126	121	116	112	108	102											
PT12-1A	87	84	46	31	29	28	26												
PT13-1A	155	150	147	148	148	147	146	131	130	134	132	132	112	106	105	106	108		
PT14-1A	110	106	104	106	105	106	103	98	113	138	160	173	105	95	88	83	86		
PT15-2A	69	68	68	67	68	67	68	67	67	66	63	62	56	54	54	56	57		
PT16-2A	104	103	102	103	103	103	102	97	100	104	105	106	87	82	79	77	80	81	
PT17-1A	145	139	138	139	139	138	135	127	137	152	159	161	118	112	108	107	115	114	
PT18-1A	101	100	99	100	100	99	98	92	97	105	110	110	89	87	88	90	99	114	
PT19-1A	114	114	114	113	113	113	112	107	111	115	117	114	101	100	101	103			
PT20-1A	122	119	115	116	115	115	111	107	109	130	136	130	119	116	116	119	126		
PT21-1A	111	110	109	109	110	109	102	101	103	104	101	90	84	85	85	86	88	96	
PT22-1A	146	145	145	145	145	144	144	138	141	150	172	185	175	153	146	142	144	174	
PT23-2A	133	131	131	131	131	130	130	121	123	132	152	158	140	124	124	126	128	198	
PT24-1A	57	57	57	57	57	57	57	53	54	55	56	58	48	45	43	42	42	45	
PT25-2A	53	52	52	52	53	52	55	55	55	52	52	53	49	49	49				
PT26-1A	83	82	82	82	82	82	83	82	82	88	97	100	91	87	85				
PT27-1A	111	105	102	102	102	101	101	96	96	98	99	99	91	92	93	96	102		
PT29-1A	65	64	64	64	64	64	79	79	78	82	84	77	73	71	68				
PT30-2A	116	114	115	115	115	114	113	105	103	104	104	103	95	92	91	93	98		
PT31-1A	150	149	149	148	149	148	147	136	131	143	153	154	146	144	154	164	183		
PT32-1A	104	103	102	103	103	102	102	97	95	93	91	90	87	86	88	92	98		
PT34-1A	48	46	47	46	46	44	43	43	42	42	40	39	34	20	18	19	18		
PT35-2A	143	142	140	141	140	139	128	124	131	148	153	149	143	143	151	168			
PT36-1A	99	98	98	98	98	99	99	96	94	93	90	90	90	91	94	97			
PT37-1A	111	110	110	110	111	111	111	105	98	97	93	96	97	97	105	114	125		
PT38-1A	17	17	17	18	18	19	19	17	18	18	18	19	16	15	16	17	21	22	
PT39-1A	52	52	52	52	54	54	54	54	51	50	49	51	49	49	51	52			
PT44-1A	51	50	50	51	50	50	50	49	46	44	42	44	46	49	52				
PT45-1A	81	81	81	80	81	80	81	81	80	75	71	69	67	69	71	74			
PT46-1A	47	47	44	44	44	44	43	41	38	36	37	43	48						
PT47-2A	83	81	80	80	79	79	79	73											
PT48-1A	53	50	50	50	50	49	50	48	46	47	44	46	37	27	29	29	34		
PT49-2A	68	64	55	55	55	55	56	56											
PT50-2A	77	77	76	77	77	77	77	76	74	75	73	71	66	64	67	69	80		
PT51-2A	123	123	122	122	124	125	126	126	122	117	103	100	95	98	104	110	128		
PT52-1A	90	90	90	90	91	89	90	89	85	82	77	76	76	79	82	90	104		
PT53-2A	67	65	65	65	66	66	66	65	63	62	60	61	54	50	48	46	45		
PT76-1A	32	32	32	32	32	32	32	29											

TABLE III. Continued

Sample	ini	100	150	200	240	280	320	360	400	440	480	520	560	590	620	650	680	690	
PT77-1A	59	59	59	59	59	59	60	56	54	56	60	61	58	60	63				
PT79-2A	194	194	194	193	195	194	195	195	190	195	208	245	246	198	192	183	183		
PT80-2A	78	78	78	77	78	78	77	75											
PT81-2A	73	74	73	74	74	74	74	71	68	67	66	64	61	60	60	62	66		
PT82-2A	97	97	97	98	98	98	98	95	91	90	86	88	91	93	99	107	121		
PT100-2A	107	106	107	107	107	107	106	104	97	102	131	144	150	160	166	174	191		
PT101-2B	86	85	85	86	86	86	86	83	78	78	79	89	103	111	127	142	156		
PT204-1A	42	42	41	41	41	41	40	38	35	37	48	53	55	59	66	77			
PT206-1C	17	17	18	17	18	17	17	15	15	17	22	24	25	31	36				
PT207-2B	55	55	55	55	56	55	55	51	48	50	50	51	48	48	48	52	55		
PT208-2B	26	27	27	27	26	27	25	23	23	28	33	35	38	44	47				
PT210-1A	37	38	38	38	37	37	35	33	32	41	45	48	51	54	53	64			
PT211-2A	31	31	31	32	31	31	30	28											
PT213-1A	37	37	36	37	29	29	29	25	25	24	27	33	32	33	38	46			
PT218-1A	70	70	69	70	69	68	68	67	69	78	113	140	131						
PT219-3A	52	52	52	52	51	52	51	50											
PT235-1A	33	33	32	33	33	32	32	30	30	32	39	42	40						
PT236-1A	17	17	17	18	17	17	17	16	17	19	24	29	25	27	29				
PT237-1B	33	33	33	33	33	33	33	30	30	32	37	39	39						
PT238-2A	23	24	24	24	24	24	23	21	23	28	39	44	34						
PT247-1A	32	32	32	32	33	32	32	30	31	32	40	43	41						
PT251-1A	23	23	23	23	23	23	23	22	22	24	33	37	37	37	41	49			
PT252-1A	65	66	65	66	65	65	65	62	65	72	86	95	85	75	75	83	86	113	
PT254-1A	53	52	53	53	52	52	52	52	52	55	70	73	68	60	60	65	72		
PT256-1A	50	50	50	51	50	50	49	46	48	52	62	67	59	52	53	57	65	80	
PT257-1A	48	48	48	48	48	48	48	47	49	55	71	81	74	65	66	71			
PT258-1A	33	33	35	33	33	33	33	31	30	33	47	53	54	52	58	66	82		
PT262-1A	48	47	47	48	47	48	48	46	47	50	58	62	54	51	50	54			
PT263-2A	25	25	24	26	25	25	24	23	24	25	32	34	32						
PT266-1A	45	45	45	46	45	45	45	43	46	51	60	62	50	48	47	50	53	70	
PT267-1A	17	17	16	17	16	17	16	15	15	17	21	22	24	28	29	36			
PT270-1A	59	59	60	60	60	60	60	60	69	82	96	84	69	69	70				

TABLE III. Continued

Sample	ini	100	150	200	230	260	280	300	320	340	360	380	400	420	440	460	480	500	520
PT40-2A	6	6	5	6	5														
PT41-2A	19	19	19	19	19	19	18	18	17	17	16	16	16	16	14	16			
PT42-1A	27	27	27	28	27	27	28	28											
PT43-1A	12	12	12	12	12	11	12	12	12	12	12	11	11	11	9	11	10	11	
PT54-2A	37	37	36	38	39	39	39	38	38	38	38	37	38	37	38	41	40	36	36
PT55-1A	75	75	76	77	76	75	76	76	75	75	74	73							
PT56-1A	86	86	86	87	87														
PT57-1A	87	86	86	87	86	86	87	86	86	85	84	82	82	79	75	77			
PT58-2A	-12	-12	-12	-12	-12														
PT59-1A	-11	-11	-11	-11	-11	-11	-11	-11	-11	-11	-11	-11	-11	-11	-12	-11			
PT60-1A	-9	-8	-9	-8	-8	-8	-8	-8	-8	-9	-8	-8							
PT61-1B	85	86	86	86	86	85	86	85	85	84	83	82	81						
PT62-2A	27	27	27	27	27	27	27	27	27	26	26	25							
PT63-1A	-17	-16	-17	-17	-17	-16	-17	-17	-17	-16	-17	-17							
PT64-2A	-13	-14	-13	-13	-13														
PT65-2A	-13	-12	-13	-12	-12	-12	-12	-12	-12	-12	-12	-12							
PT66-1A	-2	-2	-2	-2	-3														
PT67-2A	-4	-4	-4	-4	-4	-4	-4	-4											
PT68-2A	110	111	110	111	110	110	110	110											
PT69-2A	73	73	73	73	72	72	72	72	72	71	70	69	68	68	64	64	66		
PT70-2A	-13	-13	-13	-12															
PT71-1A	50	50	50	50	50	50	50	50	49	48	49	48	47	45					
PT72-2A	85	85	85	86	85	84	84	85	84	83	83	82	81	79					
PT73-2A	87	88	87	88	88	88	88	87	86	83	81	82	81	81	100	115			
PT74-1A	99	98	97	98	97	97	97	97	95	93	93	93	91	89	86	85	81	85	85
PT75-2A	88	88	88	89	88	88	88	88	87	85	84	84	83	80	79	79	78	88	87
PT78-1A	88	88	88	89	88	89	89	89	89	87	86	86	85	84	83	85			
PT83-2B	128	128	128	130	129	129	130	130	130	127	126	125	123	122	121	121	120	138	138
PT84-2A	98	98	98	100	99	100	100	100	100	98	98	97	97	96	96	98	104	121	134
PT85-2A	120	120	120	121	121	121	121	121	120	119	117	117	117	120	140	160			
PT86-2A	152	151	152	154	153	153	153	154	153	152	150	150	148	147	148	151	171	186	188
PT87-2A	3	2	3	3	2	3	2	3	2	1	1	0	0						
PT88-1B	5	5	5	6	5	5	6	6	13	28	32	37	39						
PT89-1B	-2	-2	-2	-2	-2	-2	-2	-2	-2	-2	-2	-2	0						
PT90-1A	15	13	13	13	13	13	13	12	14	15	15	16	16	17	20	27	33	35	
PT91-1A	-5	-6	-6	-5	-5	-5	-5	-4	0	2	3	6	7						
PT92-1A	0	1	1	1	1	1	0	0	0	0	0	0	0						
PT93-1A	0	0	0	0	0	0	1	1	3	3	12	14	15	16					
PT94-1A	28	28	28	29	29	29	28	28	28	27	27	27	29	29	45	68			
PT95-1A	11	11	11	12	11	12	21	59	87	96	115	122	130	133	143	160	173		
PT96-1A	5	5	6	6	5	6	6	5	5	6	6	5	6						
PT97-2A	56	49	49	49	49	49	49	48	49	48	48	48	47	48	46	50	56	64	67
PT98-1A	13	13	13	13	13	13	13	13	13	13	13	13	16	19	20	34	42		
PT99-2A	39	39	39	40	39	40	40	39	40	39	39	39							
PT102-2A	84	82	83	84	83	83	83	83	82	82	81	81							
PT103-1A	-1	-1	-1	-1	-2	-1	-1	-2	-2	-2	-2	-2	-2						
PT104-1A	25	9	9	9	9	4													

TABLE III. Continued

Sample	ini	100	150	200	230	260	280	300	320	340	360	380	400	420	440	460	480	500	520
PT105-1A	34	34	34	33	33	32	32	31	31	32	33	33	34	35	35	46	48		
PT106-1A	7	7	7	7	7	7	7	7	7	7	6	6	9						
PT107-1B	21	21	21	21	20	20	20	20	19	18	18	18	20						
PT108-1A	22	22	22	22	22	23	23	22	24	38	42	45	50	59					
PT109-1B	5	5	5	5	4	5	5	5	5	11	23	26	27	29	30	44	51	66	
PT110-1A	13	13	13	13	13	13	13	13	20	50	54	56	59	61	62	74			
PT111-1A	6	6	7	7	6	7	6	6	6	11	19	22	23	26					
PT112-1A	35	35	35	36	35	35	35	35	34	34	35	35	35						
PT113-2A	10	10	10	11	10	10	10	10	10	10	10	10							
PT114-1A	18	19	18	18	19	18	18	19	18	18	18	18	19	20	22	42	45		
PT115-1A	32	32	32	33	32	32	32	32	32	31	31	31	32	32	34	49			
PT116-1B	17	17	17	17	17	18	17	18	19	19	23	25	35	36	61	85			
PT117-1A	4	4	5	4	4	4	5	4	4	4	4	4	7	6	14	27			
PT118-1A	6	6	6	6	5	6	5	6	6	5	5	5	4	6	8	11			
PT119-2A	6	6	6	6	6	7	6	6	6	7	7	7	7						
PT120-1A	6	6	6	6	6	6	6	6	6	6	6	7	7	7					
PT121-1A	17	17	17	17	17	17	17	16	16	16	16	15	16	19					
PT122-2A	65	65	65	66	65	65	65	65	62	62	61	61	61	64	73	85	93		
PT123-1A	48	48	48	49	48	48	48	47	46	46	46	46	47	48	55	64	71	70	
PT124-1A	42	42	42	42	42	42	42	42	43	44	44	44	46	47	56	68	74	73	
PT125-2A	17	17	17	17	17	17	17	18	18	18	18	18	21	28	52	66	78		
PT126-1A	0	1	0	1	0	1	1	1	1	0	0	-1	-1	0	3	7	22	37	
PT127-1A	-7	-7	-7	-7	-7	-7	-7	-7	-2	25	52	58							
PT200-1A	20	20	20	20	20	20	20	19	19	26	28	29	31	32	39	46			
PT201-1A	5	5	5	5	5	5	5	5	5	8	10	12	12	13	23	27			
PT202-2A	9	9	9	10	9	10	10	10	10	9	9	9	9	12	28	35			
PT203-2A	21	22	22	22	22	22	22	22	22	21	19	20	19						
PT205-2A	11	11	11	11	11	11	11	10	10	9	8	7	7	7	12	17			
PT209-2A	6	6	6	6	6	6	6	6	6	5	4	3	2	2	7	8	14	17	21
PT212-1A	5	6	6	6	5	6	6	5	6	5	3	3	3	3	10	13	16	19	
PT214-1A	-7	-7	-7	-7	-6	-7	-7	-7	-7	-7	-7	-7	-8	-9	-7	-6	-4		
PT225-1B	10	10	10	10	10	11	11	11	10	10	9	8	8	8	9	11	12	15	17
PT230-1A	0	0	-1	0	-1	0	0	-1	-1	-1	-4	-4	-4	-4	-4	-3	-3		

TABLE III. Continued

Sample	ini	100	150	200	250	300	350	390	420	450	480	510	540	570	600	630	650		
PT215-1A	44	43	44	44	43	41	40	38	38	42	47	51	56	55					
PT216-1A	51	50	51	51	51	50	49	49	52	58	64	72	83	76	66	76	81		
PT217-1A	12	13	13	13	13	11	11	9	10	15	20	23	27	30	33	51			
PT220-1A	31	30	31	31	30	30	28	27	26	31	35	37	39	39					
PT221-1B	11	12	12	12	12	11	9	9	9	15	22	25	27	29	150				
PT222-2A	37	36	37	38	36	35	33	33	33	37	43	46	47	45	242				
PT223-2A	7	7	7	7	7	7	5	4	5	8	11	14	15	19	26	38	56		
PT224-2A	31	31	31	31	31	29	27	28	27	31	37	36	35	34	35	42	57		
PT226-2A	30	29	30	30	29	29	27	28	28	31	35	36	36	35	38	47			
PT227-1A	43	43	44	44	44	43	40	40	39	45	51	52	53	52	54	65	85		
PT228-1A	12	12	12	12	12	11	9	9	9	12	18	20	22	24	30	47	69		
PT229-2A	24	24	24	25	24	23	21	21	21	24	29	31	31	32	35				
PT231-2A	-4	-4	-4	-4	-4	-4	-5	-5	-5	-4	-2	0	2	4	11				
PT232-2A	14	14	15	14	14	13	12	11	12	16	20	23	24	26					
PT233-1A	47	46	47	48	46	46	45	44	44	49	57	59	61	55	55	70			
PT234-1A	29	29	30	31	30	28	27	26	26	28	35	37	38	36					
PT239-1A	32	32	32	32	32	31	31	30	29	31	38	40	41	40	39	50	70		
PT240-1A	34	33	34	35	34	33	32	30	31	33	42	48							
PT241-1A	24	24	25	24	24	23	22	22	22	24	30	33	33	32	34	48			
PT242-2A	22	21	22	22	22	22	20	18	17	21	24	31	33	34	38	67			
PT243-1A	8	8	8	8	9	8	6	6	6										
PT244-1B	25	25	25	26	25	25	22	22	21	25	28	30	30	30	35	48			
PT245-2A	26	25	27	26	26	26	23	24	23	25	29	30	30	30	33	41			
PT246-1A	27	27	27	27	27	27	24	25	24	27	30	32	31	32	35	43	62		
PT248-2A	12	11	12	12	11	11	9	9	9	11	12	12	13	15	16	22	37		
PT249-2A	3	3	3	2	3	2	0	1	1	3	4	6	8	13	15	25	39		
PT250-1B	27	26	27	28	27	27	24	24	24	27	31	33	32	33	36	43			
PT253-2A	48	48	49	49	48	48	45	45	44	51	58	60	59	58	59	67			
PT255-1A	-2	-3	-3	-2	-2	-2	-4	-3	-3										
PT259-1A	44	43	44	44	44	44	40	45	50	57	65	70	56	52	53	59			
PT260-1A	41	40	41	41	41	41	39	40	41	48	59	65	63	60	61	71	87		
PT261-2A	26	26	26	27	26	26	24	25	25	28	33	35	34						
PT264-2A	25	24	25	25	25	25	23	23	23	25	27	27	25	25					
PT265-1A	21	21	22	21	20	21	18	18	18	21	24	25	25	26	27	47	60		
PT268-1A	5	4	4	5	5	4	6	7	7	9	12	15	15	17	18	27			
PT269-2A	-4	-4	-3	-4	-4	-3	-4	-4	-4	-3	1	3	4	7	10	21	40		
PT271-2A	22	22	22	23	22	23	20	22	25	28	38	39	34	32	30	35	48		
PT272-2A	21	21	21	20	21	21	19	20	21	25	34	38							
PT273-1A	31	31	31	32	32	31	29	28	29	32	38	44	46	45	49				
PT274-2A	10	10	11	10	10	10	9	10	9	11	12	15	16	16	16	37			
PT275-2A	43	42	42	42	42	42	39	40	41	45	54	54							
PT276-2A	50	50	50	49	48	49	45	46	46	51	60	64	61	57					
PT277-1A	20	20	20	21	20	21	18	18	20	23	28	32	29	29	31	43			
PT278-1A	53	54	54	54	54	54	50	52	54	61	72	78	70	65	63	68			
PT279-1A	43	42	44	43	43	43	40	41	42	46	55	59	52	50	51				
PT280-2A	31	30	30	30	30	30	26	27	28	30	23	25	25	28					
PT281-1A	41	41	42	41	42	42	38	40	42	48	56	58	48	46	46				

TABLE III. Continued

Sample	ini	100	150	200	250	300	350	390	420	450	480	510	540	570	600	630	650		
PT282-1A	16	16	16	16	16	15	13	13	14										
PT283-1A	27	27	28	27	27	28	25	26	25	28	35	38	36	37					
PT284-2A	18	18	18	18	18	17	16	15	17	19	24	25	2	26					
PT285-3A	33	33	34	34	33	33	31	31	31	34	41	44	41	40					
PT286-1A	33	32	33	33	33	32	30	30	32	35	46	48	45	45					
PT287-2A	22	23	23	22	23	23	20	20	20	24	33	35	36	38					
PT288-2A	40	40	40	41	40	41	38	38	37	41	51	53	54	53	52	99			
PT289-2A	17	18	17	17	17	18	16	16	16	20	30	31	28	27					
PT290-1A	29	29	29	30	29	29	27	27	26	26	32	33	32	32					
PT291-1A	80	78	79	79	79	80	77	75	77	81	108	115	108	101	94	97	124		
PT292-1A	59	58	60	58	58	48	47	47	49	54	72	78	77	73					
PT293-1A	40	39	40	41	39	41	37	36	37	48	51	49	49	48					
PT294-1A	25	25	26	25	25	25	23	24	24	28	35	42	41	42					
PT295-1A	97	96	97	97	96	96	93	91	92	100	123	126	130	124	113	114	137		
PT296-2A	11	11	11	11	11	11	10	10	15	31	33								
PT297-2A	13	12	12	12	12	12	10	10	10	12	17	19	20	23					
PT298-2A	10	10	11	10	10	10	8	8	8	9	12	14							
PT299-1A	37	37	37	37	37	37	34	34	34	37	44	47	48	45	47	58			
PT300-2A	18	18	18	18	18	18	17	18	17	19	24	25							
PT301-1A	21	21	22	21	22	22	20	20	20	22	25	27	27	27					
PT302-2A	16	16	16	16	16	16	14	15	14	18	27	29	31	33					
PT303-2A	5	5	5	5	5	5	4	4	3	6	12	14	16	19					
PT304-2A	20	21	20	21	20	21	18	19	18	19	24	25	26	27					
PT305-1A	10	10	10	10	10	10	9	10	10	11	18	22	26	30					
PT306-1A	15	16	15	16	16	16	14	14	15	16	23	25	25	26	28	50			
PT307-2A	1	2	2	2	2	2	1	1	1										
PT308-1A	-1	-1	-1	0	-1	0	-2	-2	-2	-1	3	5							
PT309-1B	7	7	7	7	6	6	5	5	4	5	9	12	13	14	16	42	76		
PT310-1A	21	20	21	20	21	21	18	19	18	18	24	29	30	30	30	67			

Bulk susceptibility measured after each demagnetization step. Thermal demagnetization steps expressed in celsius degrees, susceptibility values in 10^{-6}SI.